


5-1-2019

Active Polymeric Materials for 3D Shaping and Sensing

Adebola Oyefusi
University of Wisconsin-Milwaukee

Follow this and additional works at: <https://dc.uwm.edu/etd>

 Part of the [Materials Science and Engineering Commons](#), [Organic Chemistry Commons](#), and the [Polymer Chemistry Commons](#)

Recommended Citation

Oyefusi, Adebola, "Active Polymeric Materials for 3D Shaping and Sensing" (2019). *Theses and Dissertations*. 2108.
<https://dc.uwm.edu/etd/2108>

This Dissertation is brought to you for free and open access by UWM Digital Commons. It has been accepted for inclusion in Theses and Dissertations by an authorized administrator of UWM Digital Commons. For more information, please contact open-access@uwm.edu.

ACTIVE POLYMERIC MATERIALS FOR 3D SHAPING AND SENSING

by

Adebola Olatunji Oyefusi

A Dissertation Submitted in
Partial Fulfillment of the
Requirements for the Degree of

Doctor of Philosophy

in Chemistry

at

The University of Wisconsin-Milwaukee

May 2019

ABSTRACT

ACTIVE POLYMERIC MATERIALS FOR 3D SHAPING AND SENSING

by

Adebola Oyefusi

The University of Wisconsin-Milwaukee, 2019
Under the Supervision of Professor Jian Chen

Part I: Reprogrammable Chemical 3D Shaping for Origami, Kirigami, and Reconfigurable Molding

Origami- and kirigami-based design principles have recently received strong interest from the scientific and engineering communities because they offer fresh approaches to engineering of structural hierarchy and adaptive functions in materials, which could lead to many promising applications. Herein, we present a reprogrammable 3D chemical shaping strategy for creating a wide variety of stable complex origami and kirigami structures autonomously. This strategy relies on a reverse patterning method that encodes prescribed 3D geometric information as a spatial pattern of the unlocked phase (dispersed phase) in the locked phase (matrix phase) in a pre-stretched Nafion sheet. Building upon the unique chemical reprogramming capability of the Nafion shape memory polymer, we have developed a reconfigurable molding technology that can significantly reduce the time, cost, and waste in 3D shaping of various materials with high fidelity.

Part II: A Versatile, Multifunctional, Polymer-Based Dynamically Responsive Interference Coloration

The bioinspired stimuli-responsive structural coloration offers a wide variety of potential applications, ranging from sensing to camouflage to intelligent textiles. Owing to its design simplicity, which does not require multilayers of materials with alternative refractive indices or micro- and nanostructures, thin film interference represents a promising solution towards scalable and affordable manufacturing of high-quality responsive structural coloration systems. However, thin films of polymers with appropriate thickness generally do not exhibit visible structural colors if they are directly deposited on substrates with relatively low refractive indices such as glass and polydimethylsiloxane (PDMS). Here, a versatile technology that enables polymer-based, stimuli-responsive interference coloration (RIC) on various substrates is presented. Real-time, continuous, colorimetric RIC sensors for humidity, organic vapor, temperature, and mechanical force are demonstrated by using different stimuli-responsive polymers. The transparent RIC film on glass shows strong coupling of constructive interference reflected colors and complementary destructive interference transmitted colors on opposite sides of the film. The ability to use substrates such as glass and PDMS allows for the proof-of-concept demonstration of a humidity-sensing window, and a self-reporting, self-acting sensor that does not consume external power.

TABLE OF CONTENTS

PART I.....	1
Chapter 1: Reprogrammable Chemical 3D Shaping for Origami, Kirigami, and Reconfigurable Molding	1
1.1. Introduction	1
1.2. General Materials and Methods	4
1.2.1. Chemical Locking and Unlocking of Nafion.....	8
1.2.2. Reverse patterning of Nafion.	9
1.3. Results and Discussion.....	10
1.3.1. Nafion Origami Molding	21
1.3.2. Nafion Kirigami and Molding	25
1.3.3. Shape Reprogramming and Reconfigurable Molding	31
1.4. Conclusion	35
1.5. References.....	35
Chapter 2: Multi-Length Scale 3D Shaping of Nafion-Based Reconfigurable Polymer Composite.....	39
2.1. Introduction	39
2.2. Experimental	41
2.2.1. Materials	41

3.2.2. 2D Printing	41
2.3. Results and Discussion	42
2.4. Conclusion	49
2.5. References	49
PART II.....	52
Chapter 3: A Versatile Strategy for Transparent Stimuli Responsive Interference	
Coloration	52
3.1. Introduction	52
3.2. Experimental Section	57
3.2.1. Materials.	57
3.2.2. Preparation of Metal Layer.....	57
3.2.3. Preparation of Responsive Interference Coloration (RIC) Films on Glass	
Substrates.	58
3.2.4. Sample Characterizations.....	58
3.2.5. Stimuli Response Measurements.	59
3.2.6. Verification of Humidity Sensing Mechanism.....	59
3.2.7. Humidity Cycle Test.....	60
3.3. Results and Discussion.....	61
3.3.1. Metal Coating.....	61
3.3.2. Thin-Film Interference Coloration	61

3.3.3. Colorimetric Responsive Interference Coloration (RIC) Humidity Sensor	64
3.3.4. Estimating the Thickness of the PVP Layer Using the Coefficient of Hygroscopic Expansion of PVP.	71
3.3.5. Colorimetric Responsive Interference Coloration (RIC) Organic Vapor Sensor.	77
3.3.6. Viewing Angle Dependence of RIC Films	82
3.3.7. Humidity Sensing Window	84
3.4. Conclusions	86
3.5. References.....	87
Chapter 4: Self-Reporting and Self-Acting Chemical Sensing Without Power	91
4.1. Introduction	91
4.2. Materials and Methods.....	92
4.2.1. Materials.	92
4.2.2. Preparation of Metal Layer.....	93
4.2.3. Preparation of PVP-Ir-PDMS Films.....	93
4.2.4. Sample Characterizations.....	93
4.2.5. Stimuli Response Measurements.	94
4.3. Results and Discussion.....	94
4.4. Conclusion	102
4.4. References.....	103

Curriculum Vitae.....106

LIST OF FIGURES

Figure 1.1. Reverse patterning of *us*-Nafion film. a) Schematic representation of the reverse patterning of *us*- Nafion film with a patterned line perpendicular to the stretching direction (black arrows indicate the film stretching direction). The unlocked region of the film is shown in white, and gray arrows indicate the diffusion direction from top of the film to the bottom. b) Photograph of locked *us*-Nafion film obtained by stretching the Nafion_{H+} film at 125-130 °C to a strain, $\epsilon = 150\%$, followed by locking treatment with 1M KOH solution for 1 h. c) Photograph of typical line pattern width of ~ 1 mm obtained using the Micron pen filled with 1M HCl solution before wiping. The 1M HCl solution was left on the film for 40 s and then carefully wiped off using paper towel. d) Photograph of reverse patterned Nafion film after wiping off the unlocking agent. e) Photograph of folded Nafion film after heating at 170 °C for 5 min (patterned side up). Scale bar: 5 mm. 9

Figure 1.2. Characterization of the partial unlocking gradient through the thickness of the Nafion film in reverse patterning. a) SEM image of top side of reverse patterned *us*-Nafion film ($\epsilon = 150\%$) using the procedure described in Figure 1.1. Blue arrow indicates the same marker position on both top and bottom of the film. b) SEM image of bottom side of reverse patterned *us*-Nafion film in a). The film was flipped to image the bottom side. c,d) Potassium EDX mapping image of top and bottom of reverse patterned *us*-Nafion film, respectively. e) EDX line scan across the top surface of the reverse patterned film. SEM image at the bottom shows the corresponding region where the line scan was taken and the fine green line represents the path of the scan. Green arrow

indicates the same marker position on the top of the film as in a). f) EDX line scan across the bottom surface of the reverse patterned film. SEM image at the bottom shows the corresponding region where the line scan was taken. Purple arrow indicates the same marker position on the bottom of the film as in b). Scale bar: 500 μm 12

Figure 1.3. Effect of film thickness on folding angle. a) Folding angle as a function of heating time for different Nafion film thickness. b-e) Photographs of simple folds obtained by heating of reverse patterned *us*-Nafion (thickness, $t = 115 \mu\text{m}$; $\epsilon = 50\%$) at 170 °C for (b) 5, (c) 10, (d) 15, and (e) 20 min, respectively. f-i) Photographs of simple folds obtained by heating of reverse patterned *us*-Nafion ($t = 90 \mu\text{m}$; $\epsilon = 150\%$) at 170 °C for (f) 5, (g) 10, (h) 15, and (i) 20 min, respectively. The different film thicknesses were obtained by uniaxially stretching Nafion N115 films to different strains. 13

Figure 1.4. a) Schematic representation of the reverse patterning of *us*-Nafion film with a patterned line perpendicular to the stretching direction. The unlocked region of the film is shown in white, and gray arrows indicate the diffusion direction from top of the film to the bottom. b,c) Tuning folding angle (α) of a simple fold as a function of temperature and heating time, respectively. d-g) Photographs of simple folds obtained by heating of reverse patterned *us*-Nafion for 15 mins at (d) 150, (e) 160, (f) 170, and (g) 180 °C, respectively. h-k) Photographs of simple folds obtained by heating of reverse patterned *us*-Nafion at 170 °C for (h) 5, (i) 10, (j) 15, and (k) 20 min, respectively. l) 2D pattern of a bow-tie fold with solid black lines representing reverse pattern on the top of the film. m) Photograph of the bow-tie fold obtained by heating of reverse patterned *us*-Nafion at 170 °C for 15-20 mins. n) 2D pattern of a mountain-valley fold with solid and broken black lines representing reverse patterns on the top and bottom of the film, respectively.

o) Photograph of the mountain-valley fold obtained by heating of reverse patterned *us*-Nafion at 170 °C for 10 mins. Black arrows indicate the film stretching direction. T_{def} : 125-130 °C. Scale bar: 5 mm. 15

Figure 1.5. Stability of Nafion simple fold at room temperature. a) Plot of folding angle against storage time at room temperature. Two simple fold samples (initially decoded by heating for 15 min at 150 and 170 °C, respectively) were stored at room temperature and the folding angle was measured weekly over a period of 5 weeks. Week 0 refers to the folding angle measured right after the initial decoding. b,c) Photographs of simple fold (initially decoded by heating for 15 min at 150 °C) at week 0 and week 5, respectively. d,e) Photographs of simple fold (initially decoded by heating for 15 min at 170 °C) at week 0 and week 5, respectively. Scale bar: 5 mm..... 16

Figure 1.6. Stability of Nafion simple fold at 80 °C. a) Plot of folding angle against storage time at 80 °C. Two simple fold samples (initially decoded by heating at 170 °C for 5 and 15 min, respectively) were stored at 80 °C and the folding angle was measured daily over a period of 7 days. Day 0 refers to the folding angle measured right after initial decoding. b,c) Photographs of simple fold (initially decoded at 170 °C for 5 min) at day 0 and 7, respectively. d,e) Photographs of simple fold (initially decoded at 170 °C for 15 min) at day 0 and 7, respectively. Scale bar: 5 mm..... 17

Figure 1.7. a) 2D reverse pattern of Miura-ori origami. b,c) Photographs of b) reverse patterned *us*-Nafion film, c) Nafion Miura-ori obtained by heating at 170 °C for 10 mins. d) 2D reverse pattern of bow-tie origami. e,f) Photographs of e) reverse patterned *us*-Nafion film, f) Nafion bow-tie obtained by heating at 170 °C for 15 mins. g) 2D reverse

pattern of bird origami. h,i) Photographs of h) reverse patterned *us*-Nafion film, i) Nafion bird obtained by heating at 170 °C for 15 mins. Black arrows indicate the film stretching direction. T_{def} : 125-130 °C. Scale bar: 5 mm. 19

Figure 1.8. Fine-tuning of Nafion fundamental fold units. a) 2D reverse pattern of a line perpendicular to the stretching direction. b,c) Photographs of simple fold structure after reverse patterning using 1M HCl solution, followed by heating at 170 °C for 10 min (top and perspective views). d) 2D reverse pattern of a 45° line relative to the stretching direction. e,f) Photographs of simple fold structure after reverse patterning using 1M HCl solution, followed by heating at 170 °C for 10 min (top and perspective views). g) 2D reverse pattern of a line parallel to the stretching direction. h,i) Photographs of simple fold structure after reverse patterning using 1M HCl solution, followed by heating at 170 °C for 10 min (top and perspective views). j) 2D reverse pattern of mountain-valley fold showing lines at 45 and 90° relative to the stretching direction, respectively. k) Photograph of reverse patterned *us*-Nafion film. l) Photograph of mountain-valley fold after heating at 170 °C for 10 min. m) 2D reverse pattern of mountain-valley fold showing lines at 30, 75 and 130° relative to the stretching direction, respectively. n) Photograph of reverse patterned *us*-Nafion film. o) Photograph of mountain-valley fold after heating at 170 °C for 10 min. Solid and broken black lines represent pattern lines on the top and bottom of the film, respectively. Black arrows indicate the film stretching direction. Scale bar: 5 mm. 20

Figure 1.9. PDMS molding. a) Photograph of Nafion Miura-ori master mold. b) Photograph of PDMS Miura-ori secondary mold (negative mold) obtained from molding on the front side of a). c) Photograph of PDMS Miura-ori secondary mold (positive mold)

obtained from molding on the back side of a). d) Photograph of Nafion bow-tie master mold. e) Photograph of PDMS bow-tie secondary mold (negative mold) obtained from molding on the front side of d). f) Photograph of PDMS bow-tie secondary mold (positive mold) obtained from molding on the back side of d). g) Photograph of Nafion bird master mold. h) Photograph of PDMS bird secondary mold obtained from molding on the back side of g). Scale bar: 5 mm. 22

Figure 1.10. a-c) Free standing Nickel (a) Miura-ori, (b) bow-tie, and (c) bird molded from PDMS mold in Figure 1.9b,e,h, respectively, by electroless deposition. Scale bar: 5 mm. 23

Figure 1.11. Process for nickel molding by electroless deposition. a) PDMS Miura-ori secondary mold (negative mold). b,c) Photograph of front side and back side of PDMS Miura-ori negative mold plated with nickel by electroless deposition, respectively. Nickel electroless plating was carried out at 90-93 °C for 1 h. d) Photograph of PDMS/nickel origami placed in ethyl acetate solution to induce delamination. e) Photograph of swollen PDMS mold and delaminated nickel origami in ethyl acetate solution after 6 h. f,g) Photographs of front side and back side of freestanding nickel Miura-ori origami, respectively. h) Photograph of recovered PDMS Miura-ori secondary mold after cleaning and drying. i) Photograph of magnetic nickel Miura-ori structure picked up by a magnet. Scale bar: 5 mm. 23

Figure 1.12. Shape fidelity in molding. a) Photograph of Nafion Miura-ori master mold. b) Photograph of PDMS Miura-ori complementary secondary mold. c) Photograph of nickel Miura-ori origami from b) by electroless deposition. Scale bar: 5 mm. 24

Figure 1.13. a) 2D reverse pattern of staircase kirigami. Gray lines represent cuts while solid and broken black lines represent reverse patterns on the top and bottom of the film, respectively. b-e) Photographs of b) reverse patterned *us*-Nafion film, c) Nafion staircase kirigami master mold obtained by heating at 170 °C for 5-10 mins, d) Nafion staircase kirigami functionalized with polystyrene nanospheres via spray coating, and e) Polystyrene staircase kirigami molded from c) by spray coating. Black arrows indicate the film stretching direction. T_{def} : 125-130 °C. Scale bar: 5 mm. 26

Figure 1.14. Nafion staircase kirigami unit structure. a) 2D reverse pattern of staircase kirigami unit structure. Solid gray lines represent cuts; solid and broken black lines represent pattern lines on the top and bottom, respectively. b) Photograph of patterned *us*-Nafion film after cutting and reverse patterning. c) Photograph of staircase kirigami unit structure after heating at 170 °C for 5-10 min. Similar process was used to make the Nafion staircase kirigami structure shown in Figure 1.13 with slight modification of cuts. Black arrows indicate the film stretching direction. Scale bar: 5 mm. 26

Figure 1.15. Process for polystyrene kirigami molding. a) Nafion staircase kirigami unit master mold. b) Photograph of Nafion kirigami structure coated with a PVA sacrificial layer by dip coating in a PVA aqueous solution, followed by heating at 70 °C for 10 min. c) Photograph of Nafion/PVA/polystyrene trilayer kirigami structure made by spray coating of the polystyrene solution in toluene, followed by heating at 70 °C for 10 min. d) Photograph of Nafion/PVA/Polystyrene trilayer kirigami structure soaked in water to dissolve the PVA sacrificial layer. e) Photograph of Nafion/PVA/PS trilayer kirigami after 5 h of soaking in water. Blue arrow shows complete dissolution of the sacrificial layer and separation of the polystyrene kirigami structure from the Nafion kirigami structure. f)

Photograph of recovered freestanding Nafion kirigami structure after the whole polystyrene molding process (left) and freestanding polystyrene kirigami structure molded from Nafion (right). Similar procedure was used to make the polystyrene staircase kirigami structure shown in Figure 1.13. Scale bar: 5 mm. 27

Figure 1.16. Polystyrene nanosphere coating. a) 2D reverse pattern of Miura-ori origami. b) Photograph of Nafion Miura-ori master mold after heating at 170 °C for 10 min. c) Photograph of Nafion Miura-ori origami spray-coated with monodisperse polystyrene nanospheres (Diameter: ~ 164 nm). d) 2D reverse pattern of bow-tie origami. e) Photograph of Nafion bow-tie master mold after heating at 170 °C for 15 min. f) Photograph of Nafion bow-tie origami spray-coated with polystyrene nanospheres. g) 2D reverse pattern of bird origami. h) Photograph of Nafion bird master mold after heating at 170 °C for 15 min. i) Photograph of Nafion bird origami spray-coated with polystyrene nanospheres. Scale bar: 5 mm. 28

Figure 1.17. Reflectance spectra and SEM images of polystyrene nanosphere coating on Nafion film. a) Reflectance spectra of spray-coated polystyrene nanospheres on Nafion film measured at 45 and 90°, showing that the peak position at ~ 435 nm remains to be nearly same. b,c) SEM images of spray-coated polystyrene nanospheres on Nafion film at two different magnifications, showing a quasi-amorphous structure of assembled polystyrene nanospheres with short-range order d,e) SEM images of Nafion film at two different magnifications after removal of polystyrene nanospheres with wiping. No residual polystyrene nanospheres can be detected. SEM samples were sputter coated with iridium prior to imaging. 30

Figure 1.18. a) Encoding and decoding of Nafion Miura-ori master mold on Nafion film by uniaxial stretching, reverse patterning, and heating. b) Molding of PDMS Miura-ori secondary mold from a). c) Erasing of Nafion Miura-ori to recover Nafion film by 1M HCl treatment and heating. d) Encoding and decoding of Nafion bow-tie master mold on Nafion film by uniaxial stretching, reverse patterning, and heating. e) Molding of PDMS bow-tie secondary mold from d). f) Erasing of Nafion bow-tie to recover Nafion film by 1M HCl treatment and heating. g) Encoding and decoding of Nafion zigzag folds master mold on Nafion film by uniaxial stretching, reverse patterning, and heating. h) Molding of PDMS zigzag folds secondary mold from g). i) Erasing of Nafion zigzag folds to recover Nafion film by 1M HCl treatment and heating. Scale bar: 5 mm..... 34

Figure 2.1: Photograph of 2D printer showing the robot, computer, dispenser and nozzle. Both the print head and stage have with two degree of freedom (DOF) in the x and y-direction..... 42

Figure 2.2: Hierarchical 3D Shaping on Macro- and Microscale Inspired by *Romanesco Broccoli*. a) Image of *Romanesco* broccoli showing spiral shaped hierarchical structure. b) Spiral 2D pattern of microdots. c-d) Top and side view of Nafion hierarchical structure consisting of series of microscale domes on a millimeter scale larger dome, respectively. Scale bar: 2 mm. e-f) SEM image (e) top, (f) side view, of spiral shaped hierarchical structure. Scale bar: 500µm. Black arrows indicate the film stretching direction. T_{def} : 130-140 °C 45

Figure 2.3: Hierarchical 3D Shaping on Macro- and Microscale Inspired by *Dessert Beetle*. a) Image of dessert beetle showing macroscale bumps. b) Square 2D pattern of

microdots. c-d) Top and side view of Nafion hierarchical structure obtained after heating *bs*-Nafion patterned with square array of microscale domes. Scale bar: 2 mm. T_{def} : 130-140 °C 46

Figure 2.4: 3- Length scale hierarchical 3D Shaping on Macro- and Microscale Inspired by moth eye. a) Image of moth eye. b) Radial 2D pattern of microdots. c-d) Top and side view of hierarchical structure obtained after heating *bs*-Nafion patterned with radial array of microscale domes. Scale bar: 2 mm. e-f) SEM image (e) top, (f) side view, of hierarchical structure. Green asterisks represent defects. Scale bar: 1 cm. Black arrows indicate the film stretching direction. T_{def} : 130-140 °C 47

Figure 3.1. The interference coloration principle. (a) A polymer-metal-substrate trilayer RIC design. (b,c) The Ir-glass film. (d,e) The Nafion-glass film with the polymer layer thickness comparable to that in (g). (f-g) Photographs of the Nafion-Ir-glass film. d_3 : (b-g) 5 nm. Scale bars: 1 cm. 54

Figure 3.2. Chemical structures of PVP (polyvinylpyrrolidone), PDMS (polydimethylsiloxane), and PC (polycarbonate) and Nafion used in fabrication of the thin-film interference coloration. 56

Figure 3.3. Schematic illustration of the preparation of the thin films of polymer on metal-coated substrates. 58

Figure 3.4. a) Schematic representation of the thin-film layered structure consisting of Nafion/iridium/ glass. b) Photograph of full spectrum colors generated by thin film of

Nafion deposited on iridium-coated glass. Thickness (d_2) of iridium = 5 nm. Scale bar: 1 cm. 63

Figure 3.5. Experimental setup for the dynamic reflectance spectroscopy study. The fiber optic is oriented perpendicularly to the substrate and points to the color-changing region in the RIC film. Reflectance spectra for the response and recovery of the RIC films to the stimulus vapor is acquired continuously using a fiber optic spectrometer (USB2000+, Ocean Optics) with the interval time of 10 ms. 66

Figure 3.6. a,b) Photographs (top view) of the PVP-Ir-glass film in (a) response to and (b) recovery from the localized exposure to water vapor, respectively. d_3 : 5 nm. Scale bars: 1 cm. 66

Figure 3.7. Dynamic reflectance spectra ($\theta = 0^\circ$) of the PVP-Ir-glass film in response to water vapor. 67

Figure 3.8. Dynamic reflectance spectra ($\theta = 0^\circ$) of the PVP-Ir-glass film in recovery from water vapor. 67

Figure 3.9. Reflection spectra ($\theta = 0^\circ$) of the PVP-Ir-glass film before and after exposure to water vapor. 68

Figure 3.10. a-b) No response and color change when (a) PDMS-Ir-glass film, and (b) PC-Ir-glass are exposed to hexane vapor. d_3 : 5 nm. Scale bars: 1 cm. 68

Figure 3.11. a) Photograph (top view) of the green-colored PVP-Ir-glass film before thermal crosslinking. b) Photograph of the resulting blue-colored PVPP-Ir-glass film after heating at 200 °C for 1.5 h, which leads to thermal crosslinking of PVP to form

PVPP and decrease in film thickness. c) Photograph of the blue-colored PVPP-Ir-glass film after rinsing in DI water to remove any unreacted PVP residue. d) Corresponding reflection spectra ($\theta = 0^\circ$) of the films in (a-c), respectively. d_3 : 5 nm. Scale bars: 1 cm. 69

Figure 3.12. a) Photographs (top view) of the PVPP-Ir-glass film before (left) and after dipping of lower part in water for 10 s followed by blow drying with nitrogen (right). Red broken rectangle indicates the dipped region. Since PVPP is insoluble in water, the RIC film remains intact after dipping into the water. b) Photographs (top view) of the PVP-Ir-glass film before (left) and after dipping of lower part in water for 10 s followed by blow drying with nitrogen (right). Red broken rectangle indicates the dipped region. Since PVP is soluble in water, the PVP layer in the dipped region is removed after dipping into the water. c) Reflectance spectra ($\theta = 0^\circ$) of encircled region in (a) before and after dipping test. d) Reflectance spectra ($\theta = 0^\circ$) of encircled region in (b) before and after dipping test. d_3 : 5 nm. Scale bars: 1 cm. 70

Figure 3.13. Photographs (top view) of the PVPP-Ir-glass film in (a) response to and (b) recovery from the localized exposure to water vapor, respectively. d_3 : 5 nm. Scale bars: 1 cm. 71

Figure 3.14 (a) Scheme of sensing mechanisms for water vapor. b) Photographs (top view) of the PVP-Ir-glass film at different static humidity levels. c) Reflectance spectra of PVP-Ir-glass at different static humidity levels between 20 and 70%. d_3 : 5 nm. Scale bars: 1 cm. 73

Figure 3.15. Humidity sensing mechanism. Comparison of the experimental and theoretical reflection peak positions for the PVP-Ir-glass at different static RH levels between 20 and 70%..... 74

Figure 3.16. (a) Reflection spectra ($\theta = 0^\circ$) of the PVPP-Ir-glass film before cycle #1 and after cycle #50 of localized exposure to water vapor. (b,c) Corresponding photographs (top view) of the PVPP-Ir-glass film (b) before and (c) after 50 cycles of the localized exposure to water vapor at encircled region, respectively. d_3 : 5 nm. Scale bars: 1 cm. 75

Figure 3.17. Little effects of number of humidity sensing cycles on wavelength shift from blue to red color and corresponding response time of the PVPP-Ir-glass film upon localized exposure to water vapor during cycle #1, 25 and 50. 76

Figure 3.18. (a) Reflection spectra ($\theta = 0^\circ$) of the PVPP-nichrome-glass film before cycle #1 and after cycle #50 of localized exposure to water vapor. (b,c) Corresponding photographs (top view) of the PVPP-Ir-glass film (b) before and (c) after 50 cycles of the localized exposure to water vapor at encircled region, respectively. d_3 : 5 nm. Scale bars: 1 cm. 76

Figure 3.19. Little effects of number of humidity sensing cycles on wavelength shift from blue to red color and corresponding response time of the PVPP-nichrome-glass film upon localized exposure to water vapor during cycle #1, 25 and 50. 77

Figure 3.20. a,b) Photographs (top view) of the PDMS-Ir-glass film in (a) response to and (b) recovery from the localized exposure to hexane vapor, respectively. d_3 : 5 nm. Scale bars: 1 cm. 78

Figure 3.21. Dynamic reflectance spectra ($\theta = 0^\circ$) of the PDMS-Ir-glass film in response to hexane vapor.	79
Figure 3.22. Dynamic reflectance spectra ($\theta = 0^\circ$) of the PDMS-Ir-glass film in recovery from hexane vapor.	79
Figure 3.23. Reflection spectra ($\theta = 0^\circ$) of the PDMS-Ir-glass film before and after exposure to hexane vapor.	80
Figure 3.24. a,b) Photographs (top view) of the (a) PVP-Ir-glass, and (b) PC-Ir-glass film showing no response to hexane vapor, respectively. d_3 : 5 nm. Scale bars: 1 cm... 80	80
Figure 3.25. a) Photographs (top view) of the Nafion-Ir-glass (~2.5cm square) differentiating showing different response to ammonia and triethylamine vapor. (b) Corresponding reflectance spectra of ammonia and TEA vapor treated samples.	81
Figure 3.26. a) Viewing-angle dependent photography of the PC-Ir-glass film at different viewing angles relative to the normal. b) Reflection spectroscopy of the PC-Ir-glass film at different angles of incidence (θ). The reflection spectra were obtained using a fiber-guided light source (HL-2000, Ocean Optics) and a detector (USB2000+, Ocean Optics). Both light source and detector were varied at the same angle relative to the normal. c) Comparison of the observed reflection peak positions at various θ values with corresponding predicted reflection peak positions based on Equation 1 in the main text. d_2 : 295 nm. d_3 : 5 nm. Scale bar: 1 cm.	83
Figure 3.27. Demonstration of a humidity-sensing window made of PVP-Ir-glass. (a,d,f) Top view from the PVP side in (d) response to and (f) recovery from the localized	

exposure to water vapor, respectively. (b) A traditional color wheel. Each color serves as the complement of the opposite color across the wheel. (c,e,g) Top view from the glass side in (e) response to and (g) recovery from the localized exposure to water vapor, respectively. d_3 : 3 nm. Scale bars: 1 cm..... 85

Figure 4.1. Schematic illustration of self-reporting and self-acting chemical sensor..... 95

Figure 4.2. a,b) The colorless PDMS substrate. c,d) The colorless PVP-PDMS film with the PVP layer thickness comparable to that in (g,h). e,f) The Ir-PDMS film showing light grayish color. g,h) The PVP-Ir-PDMS film showing bright blue color. d_3 : (f,h) 5 nm. Scale bars: 1 cm 96

Figure 4.3. Self-reporting and self-acting sensor. a,b) Sensing mechanisms for (a) pentane vapor and (b) water vapor, respectively. c,d) Photographs of (c) top view and (d) side view of pentane vapor-induced bending deformation of the PVP-Ir-PDMS film. e) Photographs (top view) of the PVP-Ir-PDMS film in response to and recovery from the localized exposure to water vapor, respectively. f,g) Reflection spectra ($\theta = 0^\circ$) of the encircled area (f) A and (g) B of the PVP-Ir-PDMS film in Figure 4c before and upon exposure to pentane vapor, respectively. To acquire the reflection spectra ($\theta = 0^\circ$) of the encircled area B, the fiber optic probe is oriented perpendicular to the plane of the area B of the film for both unbent and bent shapes. h) Reflection spectra ($\theta = 0^\circ$) of the encircled area C of the PVP-Ir-PDMS film in Figure 4e before and upon exposure to water vapor. d_3 : 5 nm. Scale bars: 5 mm. 99

Figure 4.4. Strain induced transparency. a-b) Photograph of PVP-Ir-PDMS at different stretching ratio in a) 0, b) 30 and c) 60% elongation, respectively. d) Transmission

spectra of PVP-Ir-PDMS at different elongation. e) Reflection spectra ($\theta = 0^\circ$) of the PVP-Ir-PDMS film at elongation ratio. d_3 : 5 nm. Scale bars: 5 mm. 100

Figure 4.5. a) Scheme of process pristine unstretched and unstretched state after stretching. b) SEM image of unstretched Ir-PDMS, c) SEM image of unstretched Ir-PDMS after stretching. Red arrows show same position. Black arrows represent the stretching direction. Green and blue arrows indicate cracks present before stretching and newly formed cracks after stretching, respectively. Scale bar: 25 μm 102

LIST OF TABLES

Table 2. 1. Properties of chemically locked and unlocked Nafion films.....	9
Table 2.2. Shape fidelity of the feature size (s) in PDMS and nickel molded structures relative to Nafion master mold.*	24

LIST OF SCHEMES

Scheme 2.1. Chemical locking and unlocking of Nafion. 8

ACKNOWLEDGEMENTS

First, I will like to thank God for the successful journey towards my graduate studies. My advisor, Dr. Jian Chen, for the opportunity he gave me in his research group. His outstanding ideas, guidance, and advice throughout my PhD studies have been the major contributor to my success and professional development. I would like to thank members of my committee — Dr. James Cook, Dr. Mark Dietz, Dr. Guilherme Indig, and Dr. Alan Schwabacher for their time and valuable contributions.

I am grateful to Dr. Ryan R. Kohlmeyer his help and suggestions on the chemical 3D shaping aspect of this work. I would like to acknowledge Dr. Heather Owen, for her help and instruction on SEM; Dr. Woo Jin Chang and members of his lab, particularly, Tae Joon Kwak, for allowing me to use his lab's oxygen plasma equipment. Thanks to Elise Nicks, Wendy Grober, Kevin Blackburn and Shelly Hagen for their help during my graduate studies at UWM. I would like to appreciate my current and immediate past members of Chen group, Dr. Banisadr, Ali Altan and Milad Momtaz for their encouragement and support.

My sincere appreciation goes to my parents and siblings for their support, prayers and encouragements. Without them, none of my success would have been possible. Many thanks to Mr. Osunnuyi and Dr. S. Osho who helped kick-start my graduate studies. To my wonderful wife and son, I say a big thank you for your understanding and support. Thanks for staying by me when the going was tough and for encouraging me to keep going. Finally, I would like to acknowledge the Olukotuns for their support. And to all my friends who have supported me through this endeavor, I say thank you!

PART I

Chapter 1: Reprogrammable Chemical 3D Shaping for Origami, Kirigami, and Reconfigurable Molding

1.1. Introduction

3D shaping allows rational tailoring of the properties and functions of materials to target applications. Conventional plastic shaping techniques like molding relies on complementary replication of the geometry from a physical template or mold. The strong coupling between the complexity of the shape and the production cost and time associated with tools and machining used in this linear shape-translation processes has limited its potential applications. Recently, a chemical 3D shaping technology has emerged that offers the possibility towards decoupling the degree of shape complexity from the production cost and time. This new technology prescribes 3D geometric information directly into a single material system such as hydrogels,¹⁻⁵ hydrogel nanocomposites,⁶ and liquid crystalline polymers⁷ via irreversible chemical patterning. Upon exposure to environmental stimuli such as heat or light, the chemical pattern can guide the material undergoing autonomous shape transformation from a simple geometry such as a flat sheet into a more complex 3D shape.

For example, patterning of a crosslinked region in a planar N-isopropylacrylamide hydrogel with a combination of UV irradiation and photomask result in a gradient sheet, which undergoes differential swelling or shrinking when exposed to different stimuli.^{2,3} In addition, a functional gradient can also be generated by remotely controlling the orientation of reinforced inorganic particles/platelets (Al_2O_3) within the hydrogel

composite using a weak magnetic field or by photo 2,3 patterning of the mesogenic unit alignment in a liquid-crystal line polymer network.^{6,7} Since the geometric information is embedded permanently, shape-reprogramming of such material systems to achieve unlimited diverse 3D structures from the same piece of polymer is impossible.

Shape memory polymers are materials that can memorize one or multiple temporary shapes and are able to return from this temporary shape to their permanent shape upon exposure to an external stimulus such as heat. Xie and coworkers discovered that the perfluorosulfonic acid ionomer, a commercial thermoplastic polymer called Nafion,⁸⁻¹⁰ exhibits novel multi-shape-memory effects without any change to the material composition. Nafion possesses a low degree of crystallinity and these crystals serve as physical cross-links that prevent flow above the thermal relaxation temperatures, as well as hold a temporary shape during the shape memory process.¹¹

Previous study found that any shape of Nafion or its composite can be reversibly locked and unlocked with high fidelity by deprotonation and reprotonation, respectively.¹³ Protonated Nafion (unlocked phase) and deprotonated Nafion (locked phase) exhibit significantly different thermal, mechanical, and electrical properties (Scheme 2.1, Table 2.1). Hence, chemical locking is particularly useful for stabilizing temporary shapes against heating to temperatures at or higher than the initial deformation temperature (T_{def}), the temperature at which a film was stretched before shape fixing upon cooling.^{13,14}

More recently, it was reported that 3D geometric information can be encoded as a spatial pattern of discrete unlocked and locked phases in a pre-stretched Nafion sheet to form a Nafion composite (encoding of 3D shape), where the location, size, shape, and

orientation of the patterned dispersed phase can be controlled and reconfigured arbitrarily by on-demand reversible acid-base chemistry.¹³ Since unlocked Nafion phase has much lower thermal relaxation temperature (T_{unlocked} : ~ 100 °C) than locked Nafion phase (T_{locked} : ~ 260 °C), shape recovery from temporary shape to permanent shape is allowed in unlocked phase but inhibited in locked phase upon heating ($T_{\text{def}} < T < 260$ °C). The heterogeneous shape recovery enables the chemical pattern to manifest into predictive 3D shapes through heat-induced differential shrinkage autonomously without using external mechanical force and physical mold (decoding of 3D shape). The resulting 3D shape can be erased via acid-base chemical treatment and heating, and then re-patterned (re-encoding of another 3D shape). Such reprogrammable chemical 3D shaping technology allows Nafion films to be repurposed directly without going through material disposal and recycling.¹³

Origami refers to an ancient folding technique that transforms a flat sheet into a complex 3D shape. Kirigami is a variation of origami that involves both cutting and folding. Origami- and kirigami-based design principles have recently received growing interest^{5,14-25} from the scientific and engineering communities and enabled a wide variety of promising applications such as self-assembling robots,¹⁸ reconfigurable mechanical metamaterials,^{19,20} self-deployable heart stents,²¹ dynamic solar tracking,²² flexible lithium-ion batteries,²³ and soft actuators.^{24,25} Therefore, it is of great interest to explore the use of reprogrammable chemical 3D shaping to create stable complex origami and kirigami structures, which can serve as adaptive master molds for 3D shaping of other materials.

Previous research has focused on a normal patterning strategy: spatial patterning of the locked phase (dispersed phase) in the unlocked phase (matrix phase).¹³ Upon heating, such patterned Nafion films undergo significant shrinkage, because the unlocked matrix phase returns to permanent shape via shrinking. Therefore, the normal patterning is not suitable for typical origami and kirigami, which requires sharp folding and rigid facets.

Herein, we report a reverse patterning strategy that involves spatial patterning of the unlocked phase (dispersed phase) in the locked phase (matrix phase), which allows for creation of numerous origami and kirigami structures autonomously (i.e. the 3D shape is mainly determined by the prescribed chemical pattern). Owing to the good mechanical and thermal stability, the resulting 3D Nafion structure can serve as a master mold to make a secondary mold (e.g. polydimethylsiloxane (PDMS)) in complementary shape with high fidelity, which can then be used for 3D shaping of various polymers, composites, ceramics, and metals. Thanks to its unique chemical reprogramming capability, a single sheet of Nafion is sufficient to produce a variety of complex 3D shapes, which enables the reconfigurable master molds.²⁶ Our reconfigurable molding technology offers engineering versatility and mobility, and can significantly reduce the time, cost, and waste in 3D shaping of various materials.

1.2. General Materials and Methods

Nafion N115 films (DuPont, $t = 127 \mu\text{m}$) were purchased through Ion Power, Inc. Sylgard 184 silicone (PDMS) was purchased from Dow Corning Corporation. Nickel electroless plating solutions (Parts A, B, and C) were purchased from Caswell Inc. Polystyrene (Average M_w : 350,000) for kirigami molding and polyvinyl alcohol (PVA;

Average M_w : 100,000) were purchased from Sigma Aldrich. Styrene monomer was purchased from Alfa Aesar. Potassium persulfate (KPS) and tin(II) chloride (SnCl_2) were purchased from Mallinckrodt Chemicals. Sodium dodecylbenzene sulfonates (SDBS) was purchased from Tokyo Chemical Industry (TCI). Palladium(II) chloride (PdCl_2) was purchased from Strem Chemicals, Inc. Airbrush (Model G44) was purchased from TCP Global Inc.

Mechanical testing was performed using a Shimadzu Autograph AGS-J universal tester with a 500 N cell load and pneumatic side-action grips. Tensile tests were carried out at 0.5 mm/min. The four-point probe electrical conductivity measurement was carried out using Lucas Laboratories Pro4 system. Film thickness was measured using a Mitutoyo Digital Micrometer. Energy-dispersive X-ray spectrometer (EDX) and line scans were performed using a Hitachi S-4800 field emission scanning electron microscope (FE-SEM) equipped with an EDX. Reflectance measurement was performed using USB 2000+ fiber optic spectrometer (Ocean Optics). Plasma treatment was carried out using Zepto (Diener Electronic).

Unless otherwise stated, all as-received Nafion films were annealed at 140 °C in nitrogen for 2h to reach their equilibrium states. Uniaxially stretched (*us*-) Nafion films were stretched using an in-house mechanical stretcher either at elevated temperature or at room temperature to a targeted strain.^{10,13} The strain, ϵ , used throughout this work is defined according to Equation 1.1

$$\epsilon = 100\% \times (L - L_0)/L_0 \quad (1.1)$$

Where L_0 is the initial length of the film and L is the final length of the film after stretching. Unless otherwise stated (e.g. shape reprogramming experiment), all Nafion films used for origami and kirigami structures were stretched to a strain of 150% at deformation temperature (T_{def}) of 125-130 °C.

The *us*-Nafion film obtained at T_{def} was fully locked by immersion in 1 M KOH followed by rinsing with deionized water and drying. All origami and kirigami structures presented in this work were realized by making prescribed 2D reverse patterns in locked *us*-Nafion films using a 0.45 mm Pigma Micron pen filled with 1M HCl solution as unlocking reagent (Cuts were created before the reverse patterning for kirigami structures), followed by heating above T_{def} to decode the 3D shapes. The Micron pen allows for the deposition of a line pattern with ~ 1 mm width of 1M HCl solution, which was left on the film for 40 s and then removed by careful wiping with paper towel. Prior to use, the as-received Micron pen was thoroughly cleaned by sonicating for 10 min each in methanol, isopropyl alcohol, and distilled water to remove ink/pigments.

PDMS molding of Nafion origami structures were performed following the manufacturer's procedure. Briefly, a 10:1 ratio of PDMS base and curing agent were thoroughly mixed and degassed in vacuum. The mixture was carefully poured onto the Nafion origami master mold and further degassed to remove any trapped bubbles within the origami structure, followed by curing at 80 °C for at least 4 h. The resulting elastomeric mold was carefully released from the Nafion master mold to give PDMS origami secondary mold.

Nickel origami structures were molded from corresponding PDMS secondary molds by electroless deposition. Prior to electroless deposition, the surface of the

PDMS secondary mold was made hydrophilic by oxygen plasma treatment for 30 s. The oxygen plasma- treated PDMS secondary mold was sensitized in SnCl_2/HCl for 30 min, followed by activation in PdCl_2/HCl solutions for another 30 min. Sensitization and activation solutions were prepared according to literature procedure.²⁷ The Pd-activated PDMS mold was then immersed in nickel electroless plating solution and the temperature of the solution was maintained at 90-93 °C. The freestanding nickel origami structure was acquired by solvent-induced delamination using ethyl acetate.

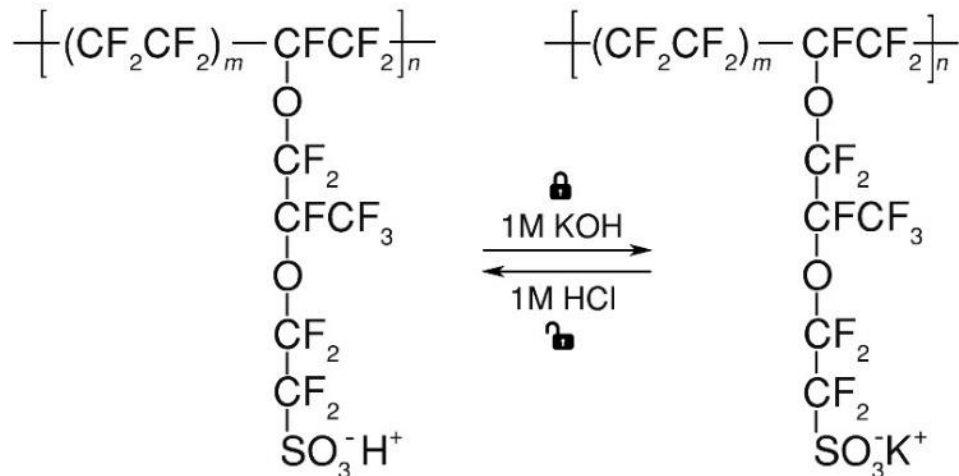
Polystyrene molding of a Nafion kirigami structure was achieved with the use of PVA as a sacrificial layer. The Nafion kirigami structure was first coated with PVA by dip coating in a 6% (w/v) PVA aqueous solution, and then coated with polystyrene by spray coating of a 5% (w/v) polystyrene solution in toluene. After molding and drying, freestanding polystyrene kirigami structure can be released by removing the PVA sacrificial layer via soaking the Nafion/PVA/polystyrene trilayer kirigami structure in water.

Monodisperse polystyrene nanospheres were synthesized by emulsion polymerization using modified literature procedure.²⁸ Briefly, styrene monomer (10.0 g) was magnetically stirred with a mixture of divinylbenzene (0.50 g), sodium dodecylbenzene sulfonate (0.084 g) in 120 mL of deionized water at 300 rpm for 15 min in a 250 mL three-necked flask equipped with a reflux condenser. Subsequently, the reaction flask was purged by nitrogen bubbling at room temperature for 15 min, followed by increasing the reaction temperature to 80 °C using a heated oil bath. After keeping the reaction temperature stable for 45 min, potassium persulfate (0.10 g) was introduced into the reaction mixture. The polymerization was terminated after 5 h, followed by cooling

down to room temperature. Finally, polystyrene nanoparticles were purified by repeated cycles of washing, centrifugation, and redispersing in deionized water to remove residual styrene and sodium dodecylbenzenesulfonate. The average diameter of polystyrene nanoparticles was obtained by scanning electron microscope (SEM) by measuring 50 particles.

1.2.1. Chemical Locking and Unlocking of Nafion

In this work, chemical *locking* refers to the deprotonation of Nafion_{H+} using 1 M KOH or NaOH solution. Although both KOH and NaOH have been demonstrated to lock Nafion films effectively,^{10,13} KOH is preferred for EDX mapping because potassium has higher atomic number than sodium. For comparison, chemical *unlocking* refers to the protonation of Nafion_{K+} or Nafion_{Na+} to Nafion_{H+} using 1M HCl solution. Protonated Nafion (unlocked phase) and deprotonated Nafion (locked phase) exhibit significantly different thermal, mechanical, and electrical properties (Scheme 2.1, Table 2.1).



Scheme 1.1. Chemical locking and unlocking of Nafion.

Table 1.1. Properties of chemically locked and unlocked Nafion films.

Properties	Unlocked Nafion	Locked Nafion
Thermal relaxation temperature (°C)	~ 100 [1]	~ 260 ¹³
Tensile strength (MPa)	31	43
Tensile modulus (MPa)	229	515
Electrical conductivity (S/cm)	3.65 X 10 ⁻⁶	Beyond instrument's lower limit

1.2.2. Reverse patterning of Nafion.

Reverse patterning refers to spatial patterning of the unlocked phase (dispersed phase) in the locked phase (matrix phase) in a pre-stretched, locked Nafion film. For all origami and kirigami structures presented in this work, reverse patterning was achieved using the Micron pen filled with 1M HCl solution (Figure .1).

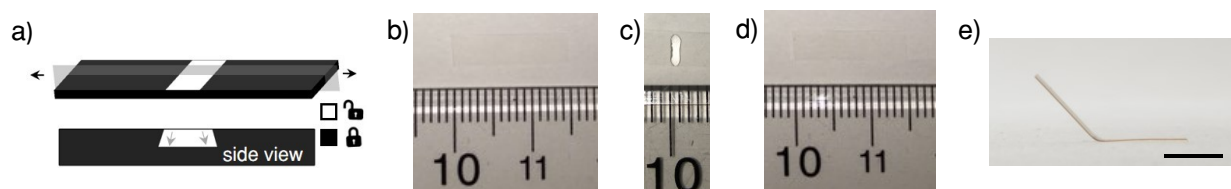


Figure 1.1. Reverse patterning of *us*-Nafion film. a) Schematic representation of the reverse patterning of *us*- Nafion film with a patterned line perpendicular to the stretching direction (black arrows indicate the film stretching direction). The unlocked region of the film is shown in white, and gray arrows indicate the diffusion direction from top of the film to the bottom. b) Photograph of locked *us*-Nafion film obtained by stretching the Nafion_{H+} film at 125-130 °C to a strain, $\epsilon = 150\%$, followed by locking treatment with 1M KOH solution for 1 h. c) Photograph of typical line pattern width of ~ 1 mm obtained using the Micron pen filled with 1M HCl solution before wiping. The 1M HCl solution was left on the film for 40 s and then carefully wiped off using paper towel. d) Photograph of reverse patterned Nafion film after wiping off the unlocking agent. e) Photograph of folded Nafion film after heating at 170 °C for 5 min (patterned side up). Scale bar: 5 mm.

1.3. Results and Discussion

For chemical 3D shaping experiments described in this study, the uniaxially stretched (*us*-) Nafion film (unlocked phase) obtained at T_{def} was fully locked by immersion in 1M KOH solution to generate a locked Nafion matrix phase. The Nafion composites were created by spatial reverse-patterning of the unlocked phase (dispersed phase) in the locked phase (matrix phase) with localized deposition of 1M HCl solution. The fold sharpness in 3D shapes, which is mainly determined by the width of fold creases, was achieved by controlling the unlocking pattern width as narrow as ~ 1 mm using a Pigma Micron pen with a 0.45 mm tip (Figure 1.1).

The simple fold can be obtained by a reverse line pattern on a locked, *us*-Nafion film (Figure 1.1a) followed by heating. The folding direction of the patterned Nafion depends on the diffusion behavior of unlocking reagent and is dependent on diffusion related variables, such as applied HCl concentration and volume, treatment time, and film thickness (Figure 1.2, 1.3). By adjusting these parameters, a partial or complete unlocking gradient can be generated, where the unlocked phase either doesn't reach the bottom side of the film or reaches the bottom of the film, respectively. In this work, using the Micron pen and controlled parameters, we observed that the folding direction of reversed patterned *us*-Nafion films is towards the patterned surface, which indicates a partial unlocking gradient through the thickness. Since only the top side of the patterned area is unlocked and can shrink upon heating above T_{def} , the Nafion film bends towards the patterned surface. This partial unlocking gradient is further supported by the EDX mapping and line scans (Figure 1.2).

The EDX mapping, line scans, which show a clear decrease in the concentration of potassium ion in the unlocked region compared with the locked region on the top side of the film (Figure 1.2c,e). In contrast, no significant change in the concentration of potassium ion is observed in the same area on the bottom side of the film according to both EDX mapping and line scan (Figure 1.2d,f). In addition, the SEM image contrast observed between unlocked and locked regions in Figure 1.2a may arise from the significant difference between electrical conductivities of unlocked and locked phases as shown in Table 1.1. No SEM image contrast is observed in the same area on the bottom side of the film (Figure 1.2b), which is consistent with the partial unlocking gradient through the thickness in Figure 1.1a.

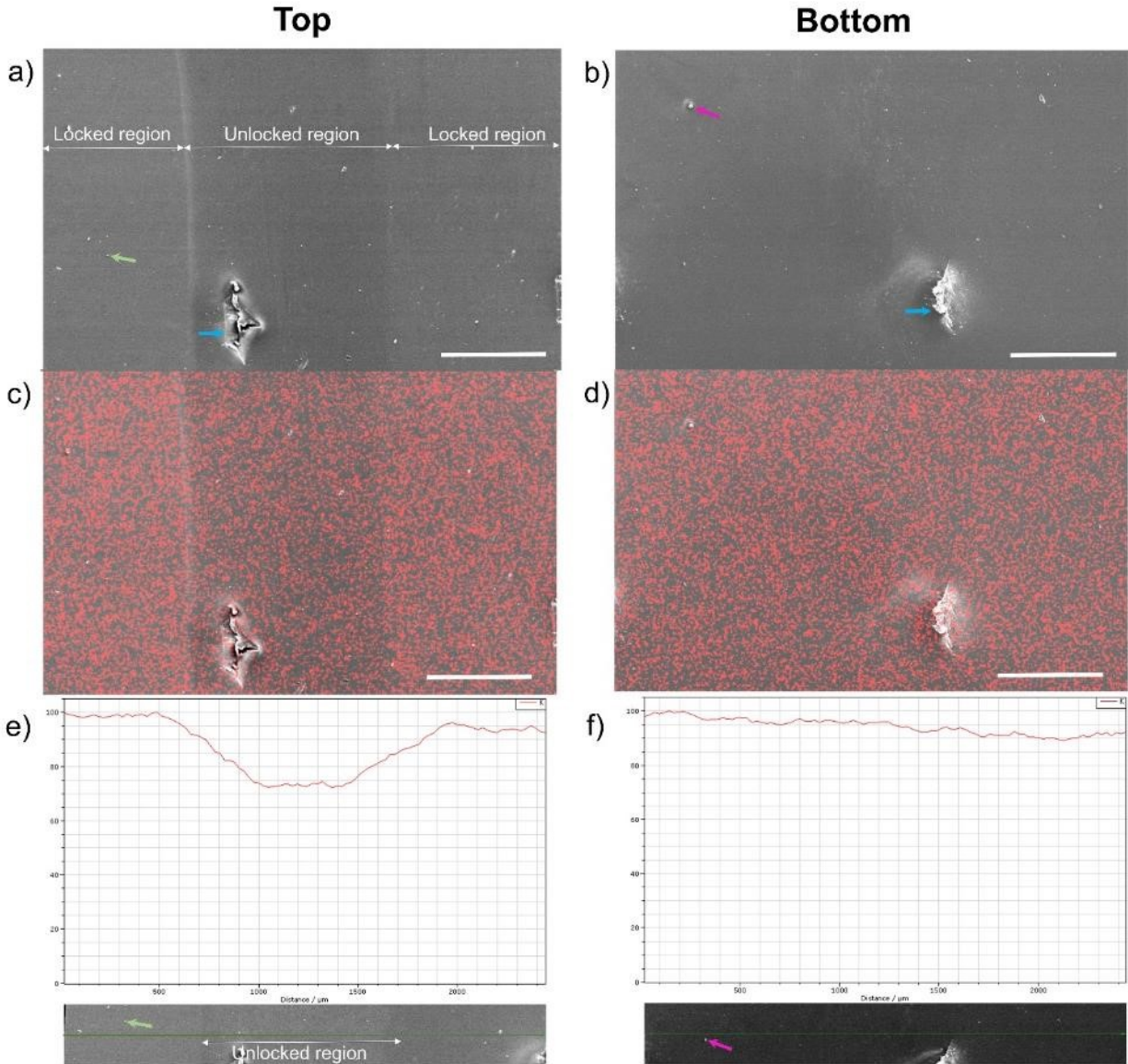


Figure 1.2. Characterization of the partial unlocking gradient through the thickness of the Nafion film in reverse patterning. a) SEM image of top side of reverse patterned *us*-Nafion film ($\epsilon = 150\%$) using the procedure described in Figure 1.1. Blue arrow indicates the same marker position on both top and bottom of the film. b) SEM image of bottom side of reverse patterned *us*-Nafion film in a). The film was flipped to image the bottom side. c,d) Potassium EDX mapping image of top and bottom of reverse patterned *us*-Nafion film, respectively. e) EDX line scan across the top surface of the reverse patterned film. SEM image at the bottom shows the corresponding region where the line scan was taken and the fine green line represents the path of the scan. Green arrow indicates the same marker position on the top of the film as in a). f) EDX line scan across the bottom surface of the reverse patterned film. SEM image at the bottom

shows the corresponding region where the line scan was taken. Purple arrow indicates the same marker position on the bottom of the film as in b). Scale bar: 500 μm .

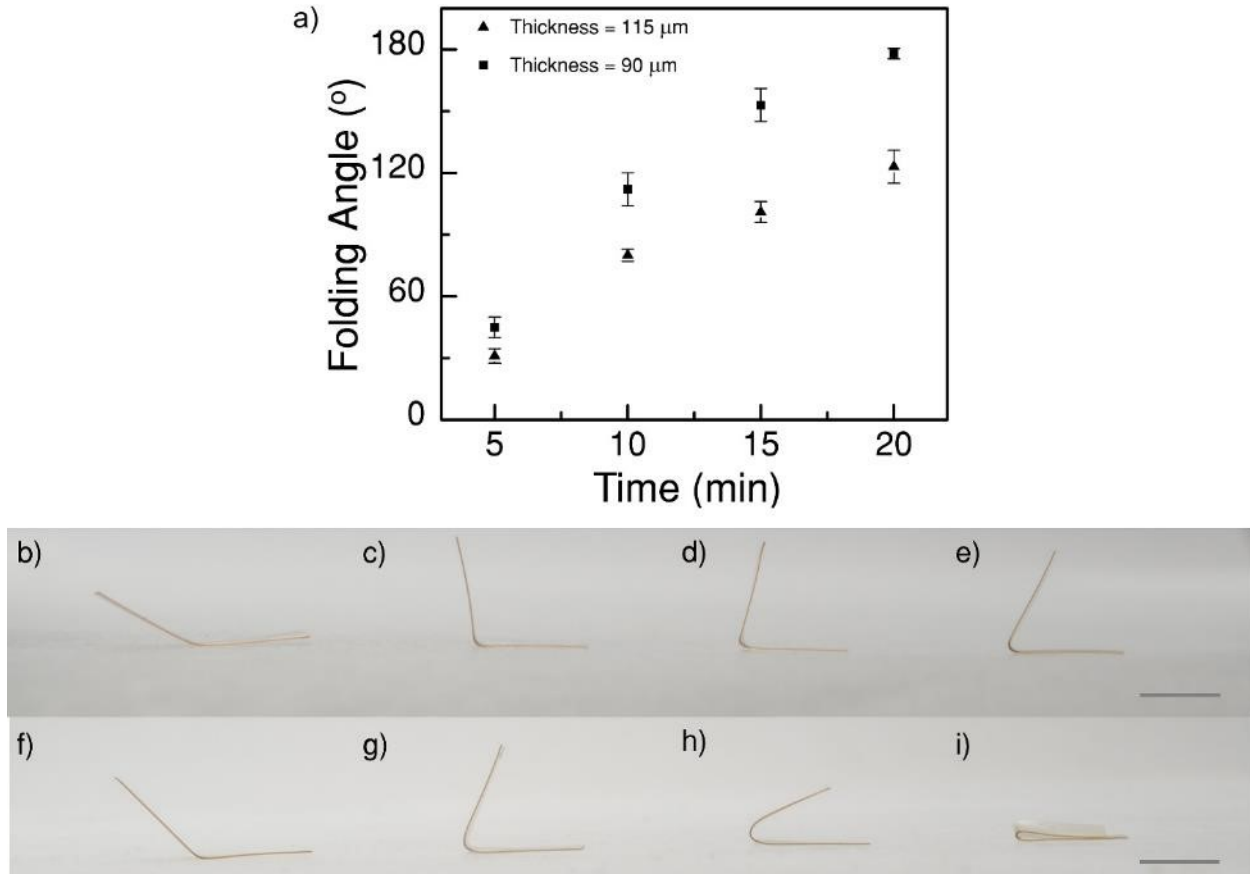


Figure 1.3. Effect of film thickness on folding angle. a) Folding angle as a function of heating time for different Nafion film thickness. b-e) Photographs of simple folds obtained by heating of reverse patterned *us*-Nafion (thickness, $t = 115 \mu\text{m}$; $\epsilon = 50\%$) at $170 \text{ }^\circ\text{C}$ for (b) 5, (c) 10, (d) 15, and (e) 20 min, respectively. f-i) Photographs of simple folds obtained by heating of reverse patterned *us*-Nafion ($t = 90 \mu\text{m}$; $\epsilon = 150\%$) at $170 \text{ }^\circ\text{C}$ for (f) 5, (g) 10, (h) 15, and (i) 20 min, respectively. The different film thicknesses were obtained by uniaxially stretching Nafion N115 films to different strains.

Three types of fundamental fold units were used for creation of various origami structures in this study: simple fold (Figure 1.4a-k), bow-tie fold (Figure 1.4l,m), and mountain-valley fold (Figure 1.4n,o).

We found that the folding angle α (Figure 1.4d) can be controlled by tuning the heating temperature and time, and film thickness, respectively. More specifically, the folding angle α increases with increase in heating temperature with constant heating time (Figure 1.4b,d-g), and it also increases with increase in heating time at the same temperature (Figure 1.4c,h-k). Although the exact underlying mechanisms remain unclear at present and require an in-depth investigation in the future, they may involve the gradient interface between fully locked and unlocked phases with variable thermal transition temperatures, and the time-dependent polymer relaxation process. Furthermore, the folding angle α decreases with increase in film thickness, owing to decrease in strain and increase in thickness of locked Nafion layer (Figure 1.3). The tunability of the folding angle offers great versatility in producing diverse origami and kirigami structures. In addition, the resulting fold angles are very stable at room temperature (Figure 1.5) and 80 °C (Figure 1.6), which is essential for various applications. The stability of 3D Nafion structures can be further enhanced to ~ 260 °C by fully relocking of the unlocked regions.

One main advantage of chemical 3D shaping is that only relatively simple chemical patterns are needed to encode more complex 3D shapes. For instance, the prescribed 5-line and 4-line reverse patterns result in the bow-tie fold (Figure 1.4l,m) and mountain-valley fold (Figure 1.4n,o), respectively, which are necessary for generating more advanced origami structures.

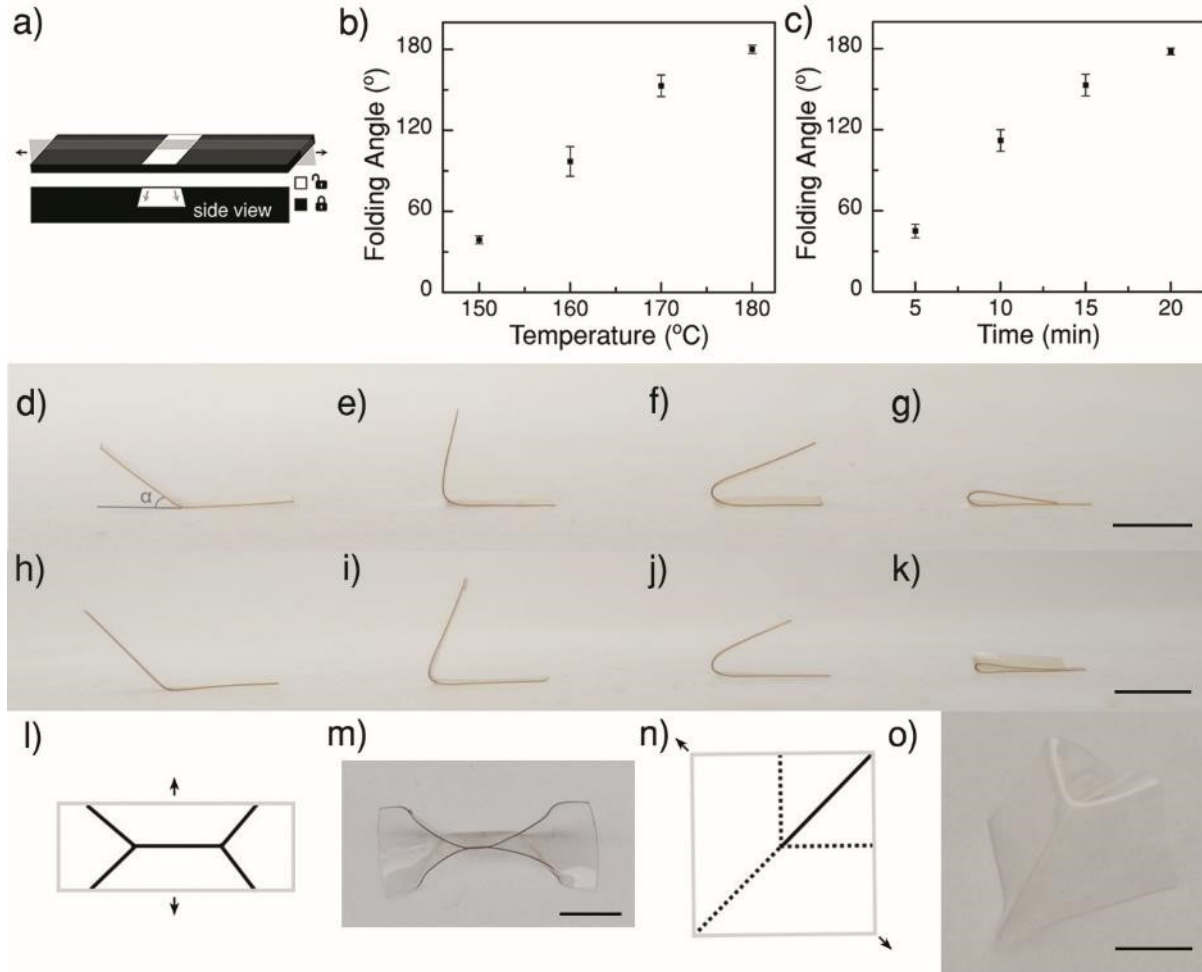


Figure 1.4. a) Schematic representation of the reverse patterning of *us*-Nafion film with a patterned line perpendicular to the stretching direction. The unlocked region of the film is shown in white, and gray arrows indicate the diffusion direction from top of the film to the bottom. b,c) Tuning folding angle (α) of a simple fold as a function of temperature and heating time, respectively. d-g) Photographs of simple folds obtained by heating of reverse patterned *us*-Nafion for 15 mins at (d) 150, (e) 160, (f) 170, and (g) 180 °C, respectively. h-k) Photographs of simple folds obtained by heating of reverse patterned *us*-Nafion at 170 °C for (h) 5, (i) 10, (j) 15, and (k) 20 min, respectively. l) 2D pattern of a bow-tie fold with solid black lines representing reverse pattern on the top of the film. m) Photograph of the bow-tie fold obtained by heating of reverse patterned *us*-Nafion at 170 °C for 15-20 mins. n) 2D pattern of a mountain-valley fold with solid and broken black lines representing reverse patterns on the top and bottom of the film, respectively. o) Photograph of the mountain-valley fold obtained by heating of reverse patterned *us*-Nafion at 170 °C for 10 mins. Black arrows indicate the film stretching direction. T_{def} : 125-130 °C. Scale bar: 5 mm.

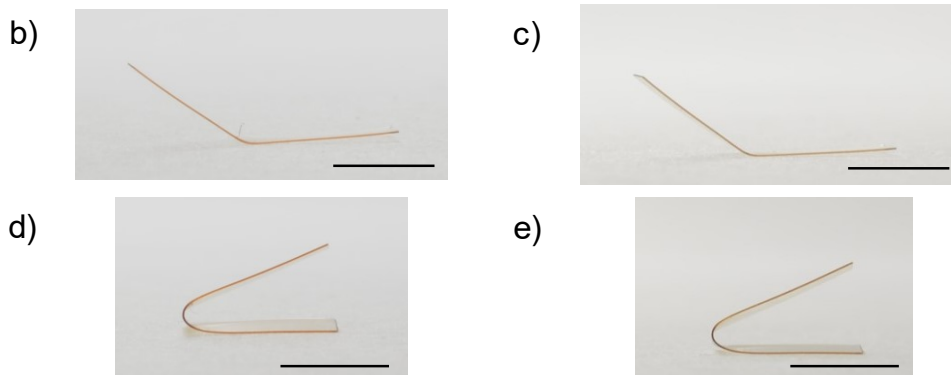
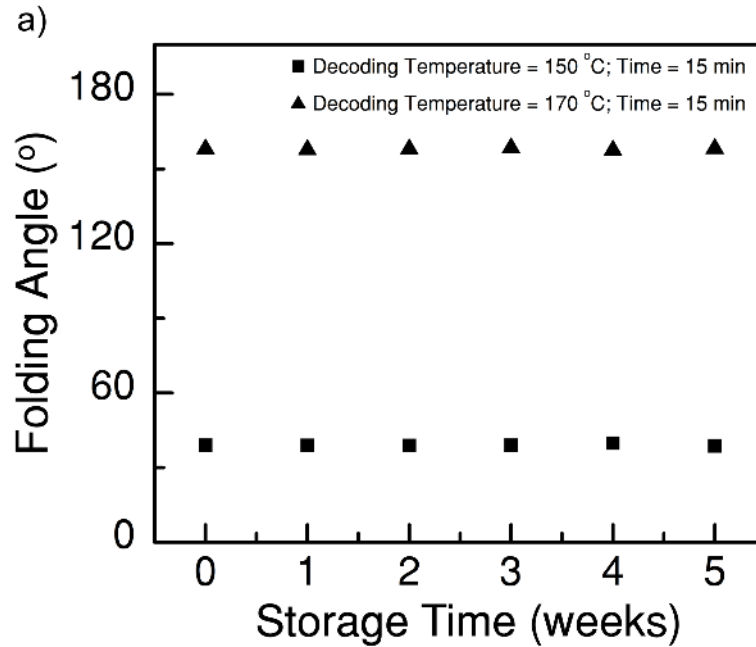


Figure 1.5. Stability of Nafion simple fold at room temperature. a) Plot of folding angle against storage time at room temperature. Two simple fold samples (initially decoded by heating for 15 min at 150 and 170 °C, respectively) were stored at room temperature and the folding angle was measured weekly over a period of 5 weeks. Week 0 refers to the folding angle measured right after the initial decoding. b,c) Photographs of simple fold (initially decoded by heating for 15 min at 150 °C) at week 0 and week 5, respectively. d,e) Photographs of simple fold (initially decoded by heating for 15 min at 170 °C) at week 0 and week 5, respectively. Scale bar: 5 mm.

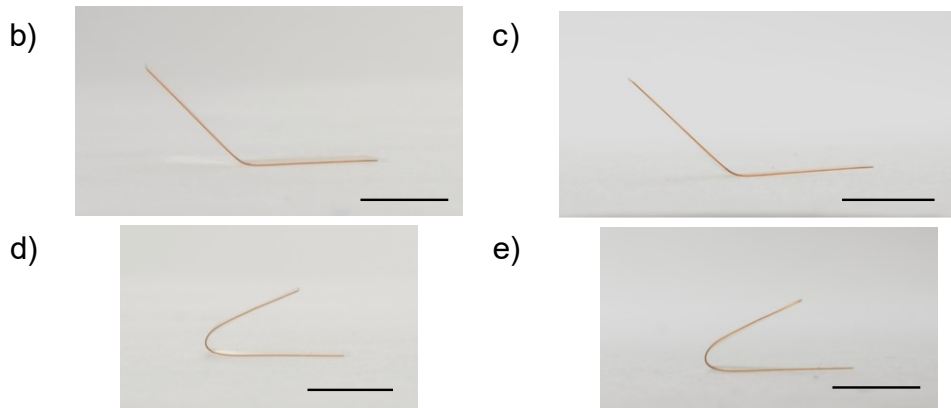
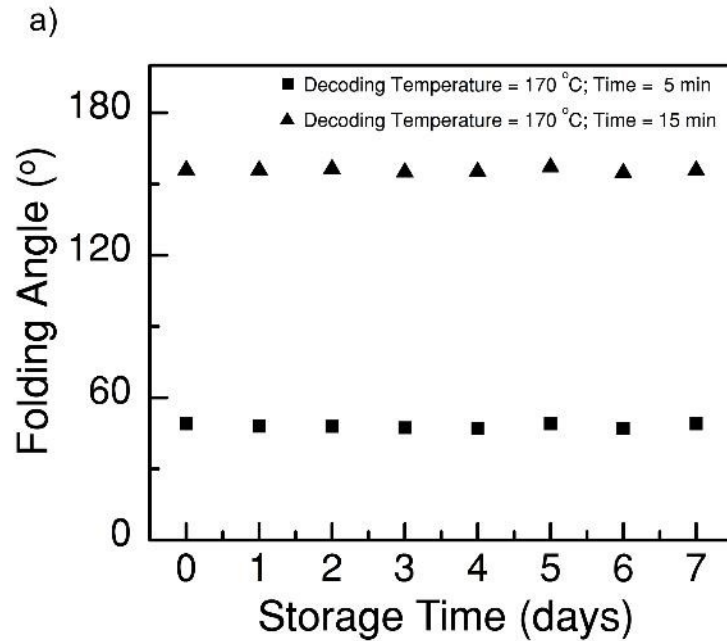


Figure 1.6. Stability of Nafion simple fold at 80 °C. a) Plot of folding angle against storage time at 80 °C. Two simple fold samples (initially decoded by heating at 170 °C for 5 and 15 min, respectively) were stored at 80 °C and the folding angle was measured daily over a period of 7 days. Day 0 refers to the folding angle measured right after initial decoding. b,c) Photographs of simple fold (initially decoded at 170 °C for 5 min) at day 0 and 7, respectively. d,e) Photographs of simple fold (initially decoded at 170 °C for 15 min) at day 0 and 7, respectively. Scale bar: 5 mm.

A variety of complex origami structures were made based on reverse patterning and subsequent heating of the *us*-Nafion films (Figure 1.7). The Miura-ori origami involves repeating units of mountain-valley folds (Figure 1.7a-c). The bow-tie origami comprises

repeating units of bow-tie folds and simple folds (Figure 1.7 d-f). The bird origami includes various mountain-valley folds and simple folds (Figure 1.7g-i). We observed that alteration of simple fold and mountain-valley fold line pattern angles versus the film stretching direction does not change the corresponding fold type, and it mainly affects the dimensions and orientation angles of facets in the fold structures (Figure 1.8). This fine-tuning capability enables high adaptability in origami design.

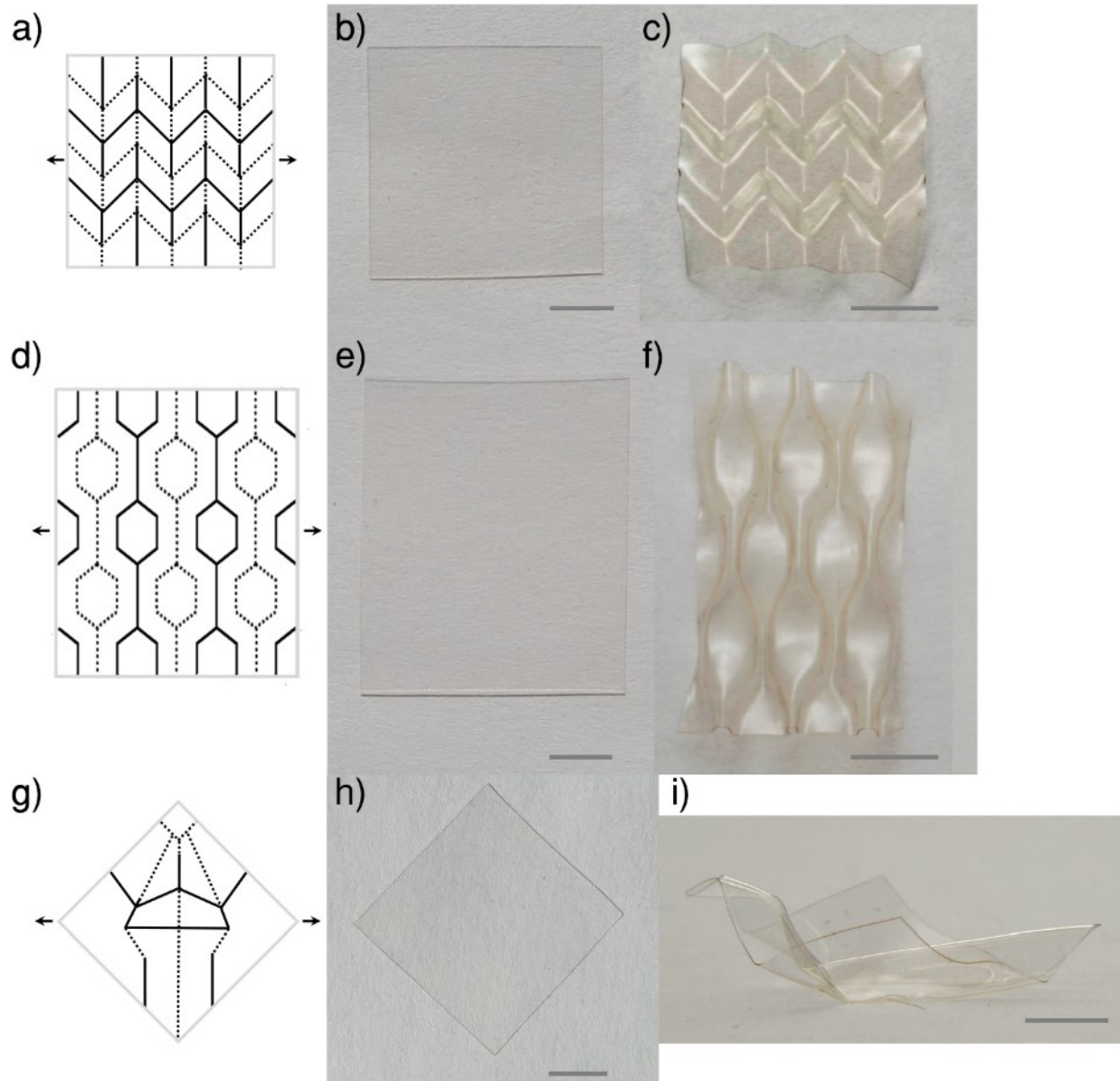


Figure 1.7. a) 2D reverse pattern of Miura-ori origami. b,c) Photographs of b) reverse patterned *us*-Nafion film, c) Nafion Miura-ori obtained by heating at 170 °C for 10 mins. d) 2D reverse pattern of bow-tie origami. e,f) Photographs of e) reverse patterned *us*-Nafion film, f) Nafion bow-tie obtained by heating at 170 °C for 15 mins. g) 2D reverse pattern of bird origami. h,i) Photographs of h) reverse patterned *us*-Nafion film, i) Nafion bird obtained by heating at 170 °C for 15 mins. Black arrows indicate the film stretching direction. T_{def} : 125-130 °C. Scale bar: 5 mm.

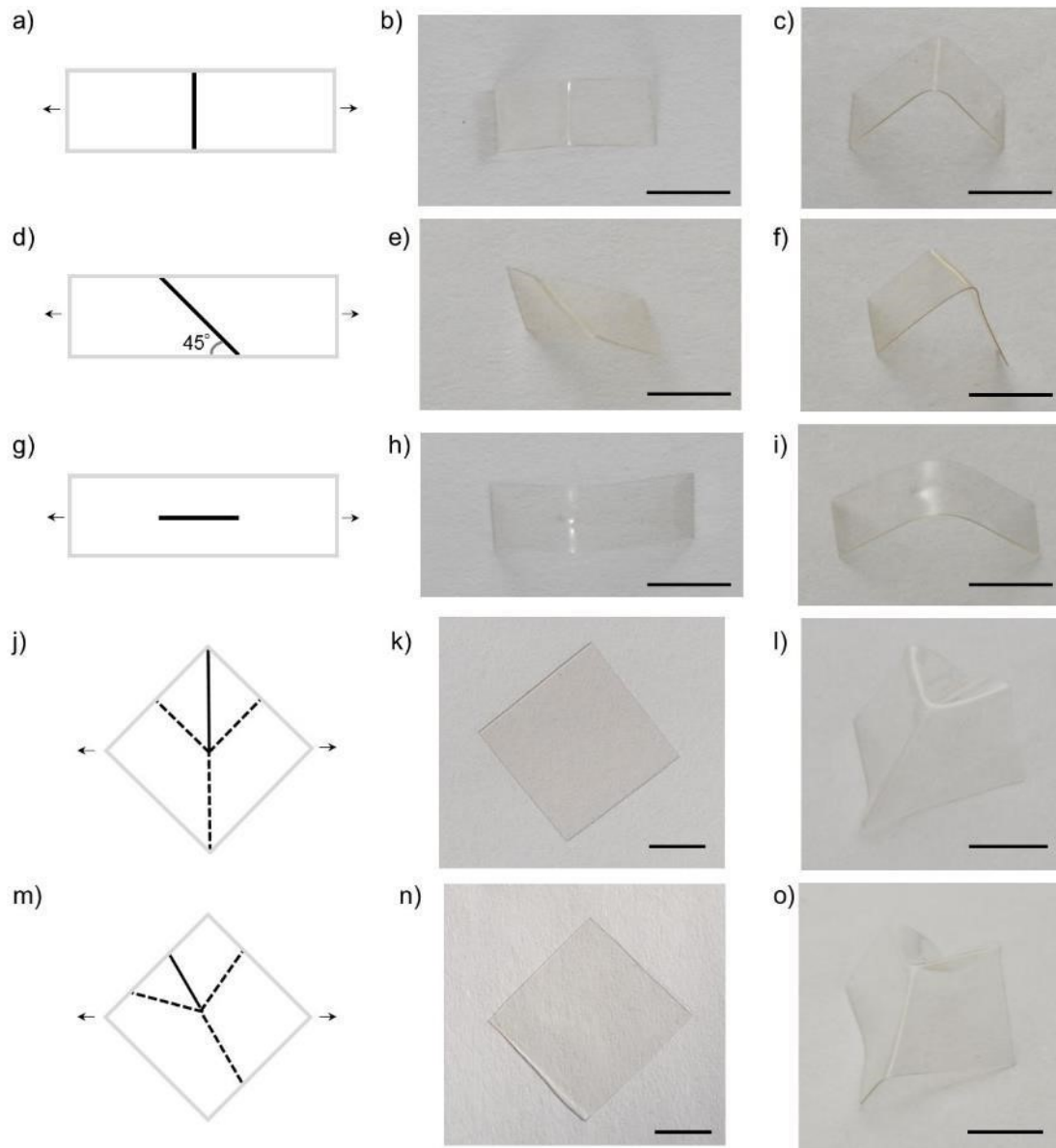


Figure 1.8. Fine-tuning of Nafion fundamental fold units. a) 2D reverse pattern of a line perpendicular to the stretching direction. b,c) Photographs of simple fold structure after reverse patterning using 1M HCl solution, followed by heating at 170 °C for 10 min (top and perspective views). d) 2D reverse pattern of a 45° line relative to the stretching direction. e,f) Photographs of simple fold structure after reverse patterning using 1M HCl solution, followed by heating at 170 °C for 10 min (top and perspective views). g) 2D reverse pattern of a line parallel to the stretching direction. h,i) Photographs of simple fold structure after reverse patterning using 1M HCl solution, followed by heating at 170 °C for 10 min (top and perspective views). j) 2D reverse pattern of mountain-valley fold showing lines at 45 and 90° relative to the stretching direction, respectively. k) Photograph of reverse patterned *us*-Nafion film. l) Photograph of mountain-valley fold

after heating at 170 °C for 10 min. m) 2D reverse pattern of mountain-valley fold showing lines at 30, 75 and 130° relative to the stretching direction, respectively. n) Photograph of reverse patterned *μ*s-Nafion film. o) Photograph of mountain-valley fold after heating at 170 °C for 10 min. Solid and broken black lines represent pattern lines on the top and bottom of the film, respectively. Black arrows indicate the film stretching direction. Scale bar: 5 mm.

1.3.1. Nafion Origami Molding

Stable Nafion 3D origami structures can serve as master molds to fabricate PDMS secondary molds in complementary 3D shapes with high fidelity (Figure 1.9a-h), Table 2.2). PDMS has a number of properties that are instrumental in molding high-quality structures.²⁹ Therefore the resulting PDMS molds can be used for 3D shaping of various polymers, composites, ceramics, and metals with exact copy of original Nafion master mold structure. For instance, the freestanding magnetic 3D nickel structures such as Miura-ori, bow-tie, and bird origamis can be made from corresponding PDMS molds using electroless deposition followed by release (Figure 1.10a-c, Figure 1.11).

Although PDMS negative mold was used in the electroless deposition process in Figure 1.11, either negative or positive PDMS secondary mold can be used for electroless deposition to make freestanding magnetic nickel origami structure. In either case, the obtained nickel origami structure shows two faces – one complementary to and another same as the PDMS secondary mold used in the nickel molding process. Swelling of PDMS with ethyl acetate caused the PDMS to increase in size significantly without affecting the size of the nickel structure, leading to delamination of the nickel origami from PDMS mold (Figure 1.11e). The swollen PDMS secondary mold returned to its original shape after cleaning and drying at room temperature and can be re-used for next molding process.

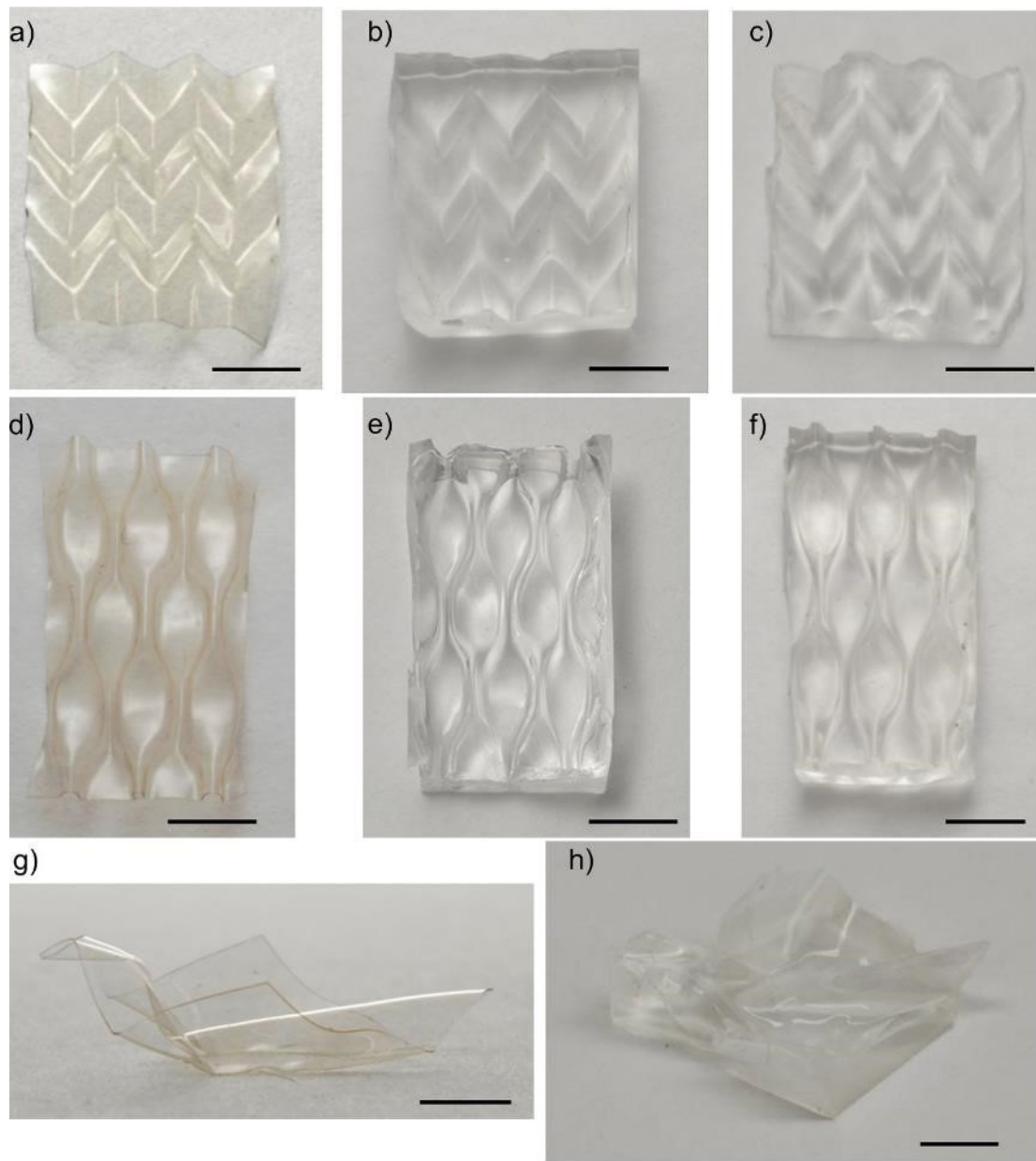


Figure 1.9. PDMS molding. a) Photograph of Nafion Miura-ori master mold. b) Photograph of PDMS Miura-ori secondary mold (negative mold) obtained from molding on the front side of a). c) Photograph of PDMS Miura-ori secondary mold (positive mold) obtained from molding on the back side of a). d) Photograph of Nafion bow-tie master mold. e) Photograph of PDMS bow-tie secondary mold (negative mold) obtained from molding on the front side of d). f) Photograph of PDMS bow-tie secondary mold (positive mold) obtained from molding on the back side of d). g) Photograph of Nafion bird master mold. h) Photograph of PDMS bird secondary mold obtained from molding on the back side of g). Scale bar: 5 mm.

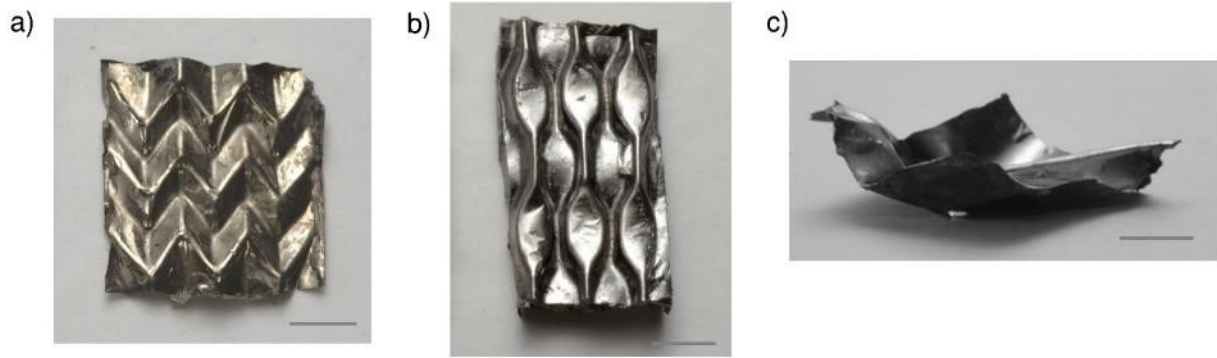


Figure 1.10. a-c) Free standing Nickel (a) Miura-ori, (b) bow-tie, and (c) bird molded from PDMS mold in Figure 1.9b,e,h, respectively, by electroless deposition. Scale bar: 5 mm.

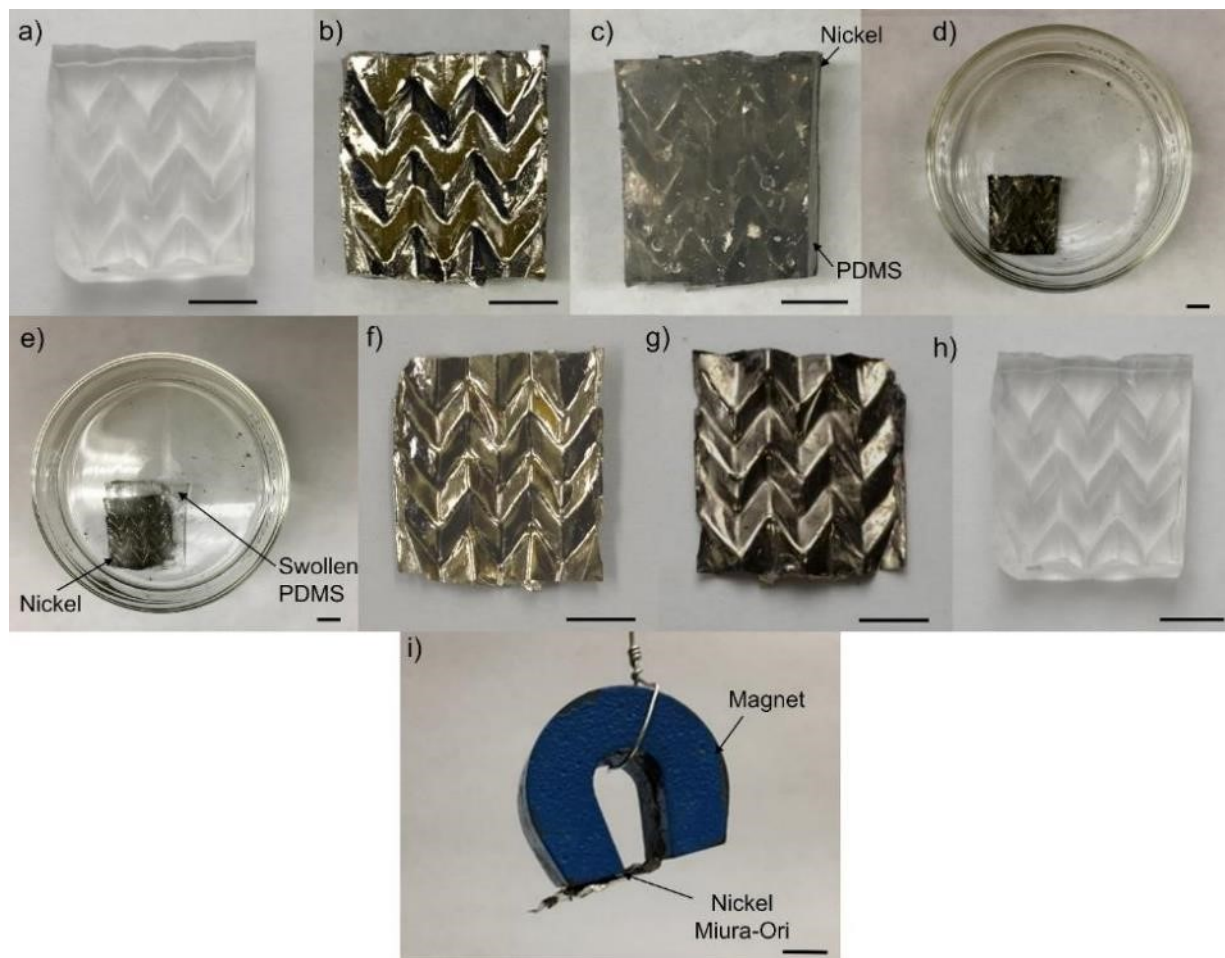


Figure 1.11. Process for nickel molding by electroless deposition. a) PDMS Miura-ori secondary mold (negative mold). b,c) Photograph of front side and back side of PDMS

Miura-ori negative mold plated with nickel by electroless deposition, respectively. Nickel electroless plating was carried out at 90-93 °C for 1 h. d) Photograph of PDMS/nickel origami placed in ethyl acetate solution to induce delamination. e) Photograph of swollen PDMS mold and delaminated nickel origami in ethyl acetate solution after 6 h. f,g) Photographs of front side and back side of freestanding nickel Miura-ori origami, respectively. h) Photograph of recovered PDMS Miura-ori secondary mold after cleaning and drying. i) Photograph of magnetic nickel Miura-ori structure picked up by a magnet. Scale bar: 5 mm.

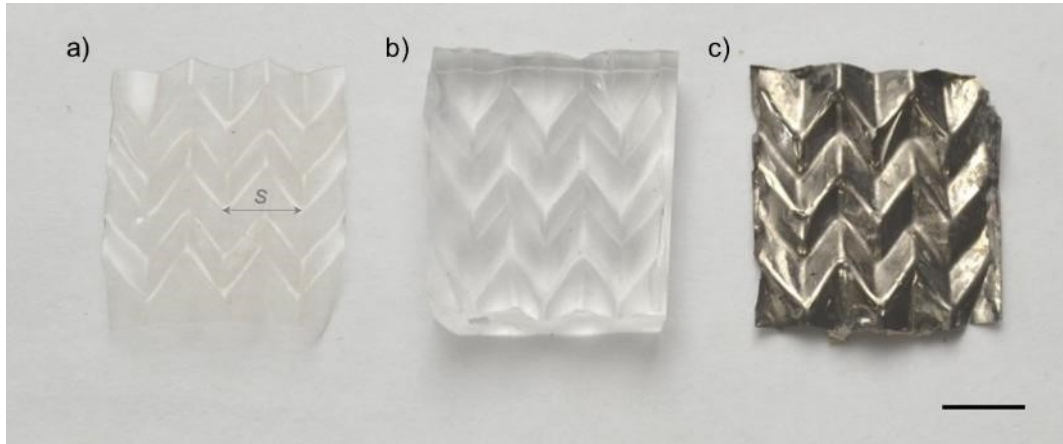


Figure 1.12. Shape fidelity in molding. a) Photograph of Nafion Miura-ori master mold. b) Photograph of PDMS Miura-ori complementary secondary mold. c) Photograph of nickel Miura-ori origami from b) by electroless deposition. Scale bar: 5 mm.

Table 1.2. Shape fidelity of the feature size (s) in PDMS and nickel molded structures relative to Nafion master mold.*

	$s_{average}$ (mm)	Shape Fidelity (%)
Nafion	4.6	Master mold
PDMS	4.5	98
Nickel	4.4	96

* s is defined as the distance between the vertices of two successive mountain-valley folds (one such feature is shown in Figure 1.12). Reported $s_{average}$ value is the average of six measured s values from different regions.

1.3.2. Nafion Kirigami and Molding

Combination of reverse patterning and cutting followed by heating leads to the formation of kirigami structures. A staircase kirigami can be created by incorporating repeating units of simple folds and cuts (Figure 1.13a-c, Figure 1.14). Using the Nafion kirigami as a master mold, the kirigami structure of the exact copy based on other polymers such as polystyrene can be produced via spray coating technique followed by release (Figure 1.13e, Figure 1.15). Rational functionalization of origami and kirigami surfaces is highly desirable for many potential applications. We showed that a structural color coating can be formed on Nafion origami and kirigami surfaces by spray coating of polystyrene nanospheres (Diameter: ~ 164 nm, Figure 1.13e, Figure 1.16). The viewing angle-independent bluish color originates from the reflection band at ~ 435 nm of the quasi-amorphous structure (Figure 1.17a).^{30,31} Pristine Nafion surfaces can be fully recovered by complete removal of polystyrene nanospheres with wiping (Figure 1.17b-e).

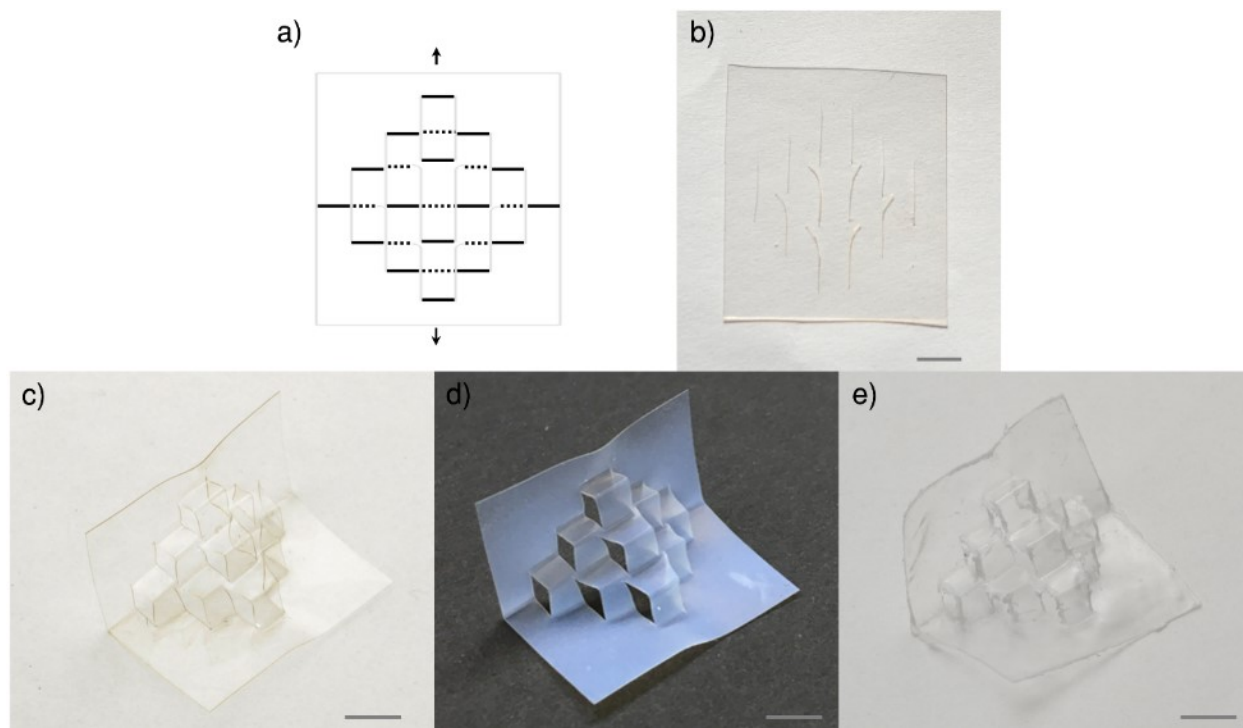


Figure 1.13. a) 2D reverse pattern of staircase kirigami. Gray lines represent cuts while solid and broken black lines represent reverse patterns on the top and bottom of the film, respectively. b-e) Photographs of b) reverse patterned *us*-Nafion film, c) Nafion staircase kirigami master mold obtained by heating at 170 °C for 5-10 mins, d) Nafion staircase kirigami functionalized with polystyrene nanospheres via spray coating, and e) Polystyrene staircase kirigami molded from c) by spray coating. Black arrows indicate the film stretching direction. T_{def} : 125-130 °C. Scale bar: 5 mm.

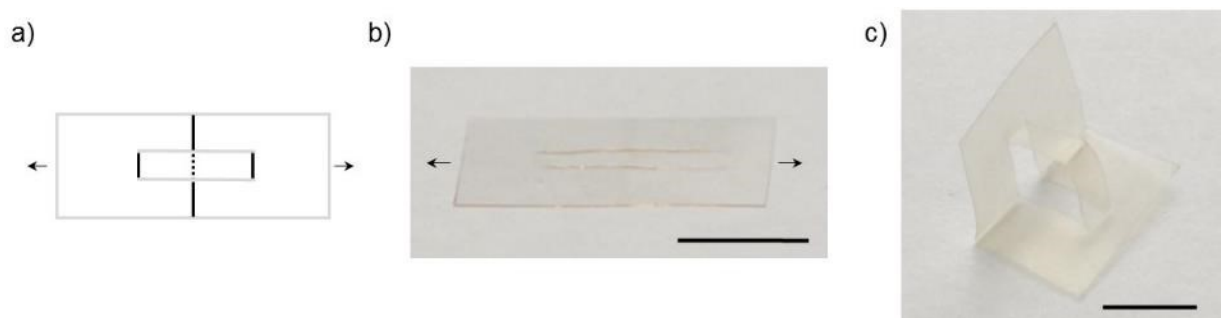


Figure 1.14. Nafion staircase kirigami unit structure. a) 2D reverse pattern of staircase kirigami unit structure. Solid gray lines represent cuts; solid and broken black lines represent pattern lines on the top and bottom, respectively. b) Photograph of patterned *us*-Nafion film after cutting and reverse patterning. c) Photograph of staircase kirigami unit structure after heating at 170 °C for 5-10 min. Similar process was used to make the Nafion staircase kirigami structure shown in Figure 1.13 with slight modification of cuts. Black arrows indicate the film stretching direction. Scale bar: 5 mm.

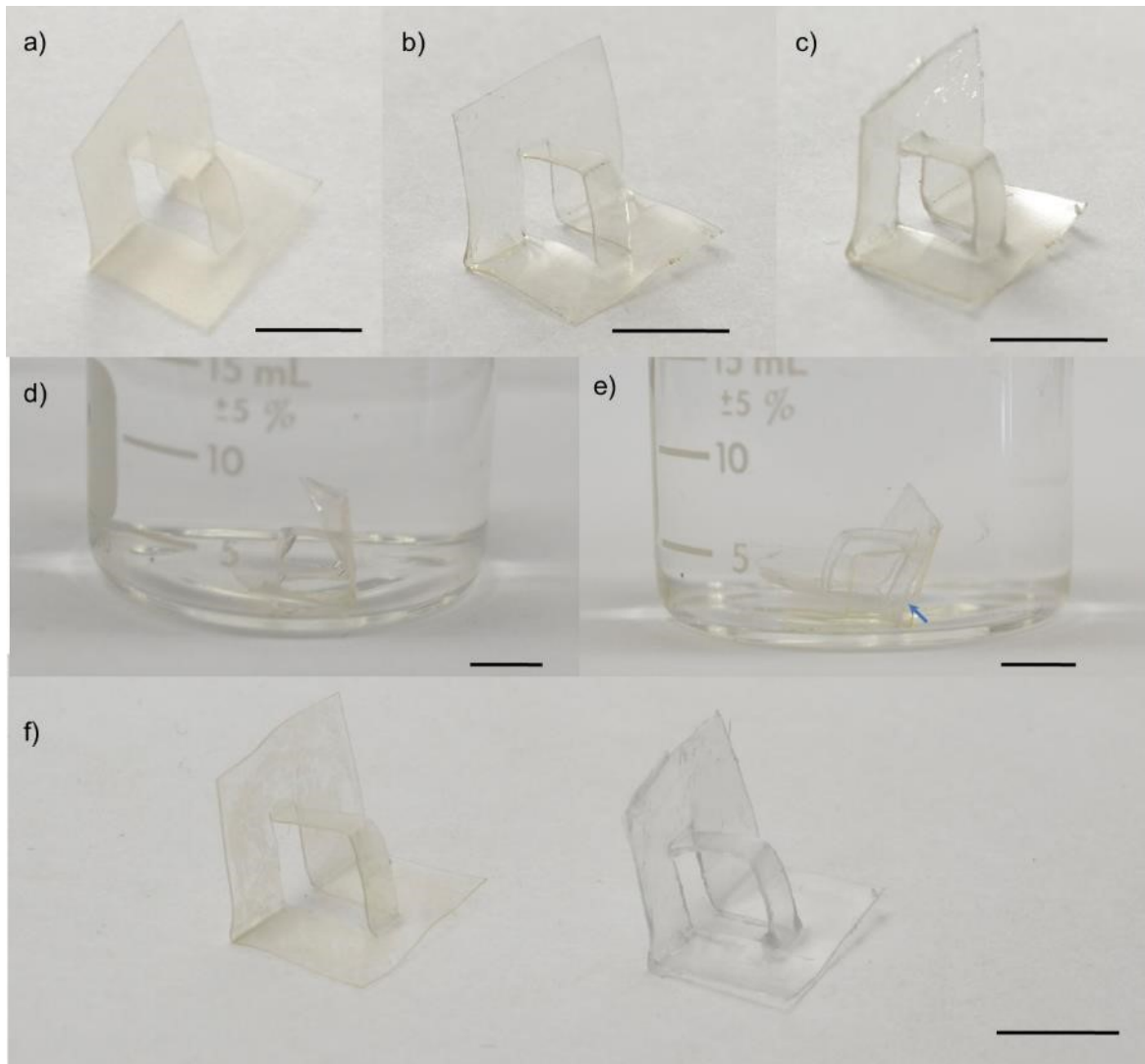


Figure 1.15. Process for polystyrene kirigami molding. a) Nafion staircase kirigami unit master mold. b) Photograph of Nafion kirigami structure coated with a PVA sacrificial layer by dip coating in a PVA aqueous solution, followed by heating at 70 °C for 10 min. c) Photograph of Nafion/PVA/polystyrene trilayer kirigami structure made by spray coating of the polystyrene solution in toluene, followed by heating at 70 °C for 10 min. d) Photograph of Nafion/PVA/Polystyrene trilayer kirigami structure soaked in water to dissolve the PVA sacrificial layer. e) Photograph of Nafion/PVA/PS trilayer kirigami after 5 h of soaking in water. Blue arrow shows complete dissolution of the sacrificial layer and separation of the polystyrene kirigami structure from the Nafion kirigami structure. f) Photograph of recovered freestanding Nafion kirigami structure after the whole polystyrene molding process (left) and freestanding polystyrene kirigami structure

molded from Nafion (right). Similar procedure was used to make the polystyrene staircase kirigami structure shown in Figure 1.13. Scale bar: 5 mm.

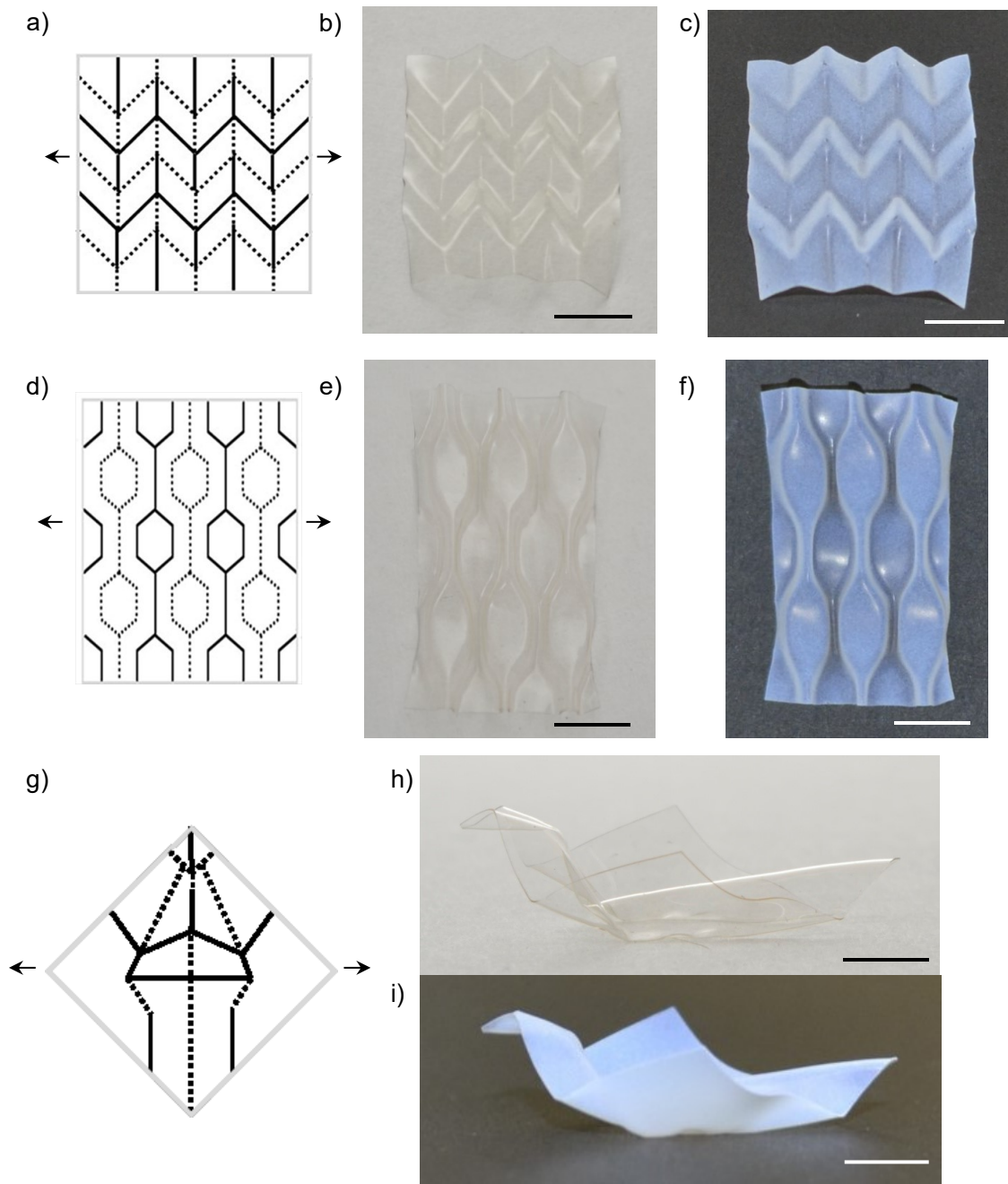


Figure 1.16. Polystyrene nanosphere coating. a) 2D reverse pattern of Miura-ori origami. b) Photograph of Nafion Miura-ori master mold after heating at 170 °C for 10 min. c) Photograph of Nafion Miura-ori origami spray-coated with monodisperse

polystyrene nanospheres (Diameter: ~ 164 nm). d) 2D reverse pattern of bow-tie origami. e) Photograph of Nafion bow-tie master mold after heating at 170 °C for 15 min. f) Photograph of Nafion bow-tie origami spray-coated with polystyrene nanospheres. g) 2D reverse pattern of bird origami. h) Photograph of Nafion bird master mold after heating at 170 °C for 15 min. i) Photograph of Nafion bird origami spray-coated with polystyrene nanospheres. Scale bar: 5 mm.

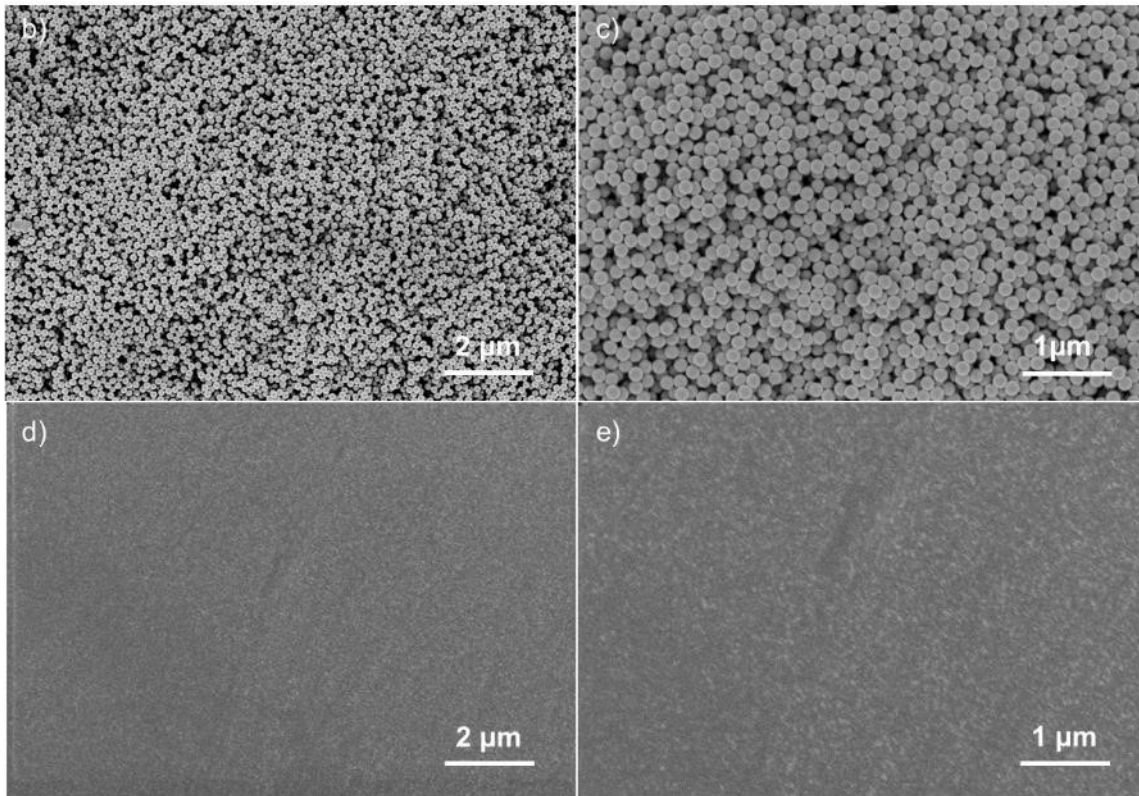
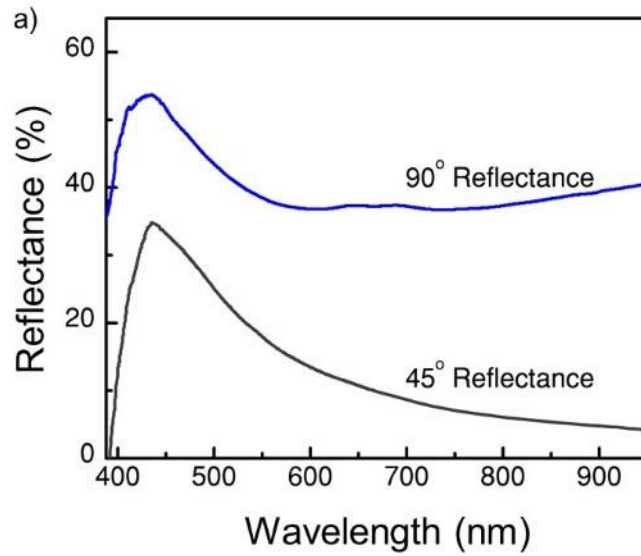


Figure 1.17. Reflectance spectra and SEM images of polystyrene nanosphere coating on Nafion film. a) Reflectance spectra of spray-coated polystyrene nanospheres on Nafion film measured at 45 and 90°, showing that the peak position at ~ 435 nm remains to be nearly same. b,c) SEM images of spray-coated polystyrene nanospheres on Nafion film at two different magnifications, showing a quasi-amorphous structure of

assembled polystyrene nanospheres with short-range order d,e) SEM images of Nafion film at two different magnifications after removal of polystyrene nanospheres with wiping. No residual polystyrene nanospheres can be detected. SEM samples were sputter coated with iridium prior to imaging.

1.3.3. Shape Reprogramming and Reconfigurable Molding

Conventional manufacturing systems for 3D shaping of materials rely on passive tooling systems such as fixed molds and dies, which are unable to rapidly respond to changing needs with new and modified platforms due to extended development timelines and high costs associated with tool development. Here we have demonstrated the feasibility of reconfigurable molding based on shape reprogramming. A single Nafion sheet is sufficient to produce three different Nafion master molds and complementary PDMS secondary molds: Miura-ori, bow-tie, and zigzag folds. (Figure 1.18). The whole experiment involves the following steps:

1) Encoding and decoding of Nafion Miura-ori master mold on Nafion film (Figure 1.18a).

The Nafion film in its permanent shape was uniaxially stretched to a strain of $\epsilon = 81\%$ at room temperature, followed by fixing under load for 10 min. The stretching was performed sequentially by dividing the Nafion film into three segments and each segment was stretched evenly. This sequential stretching allows for areas close to the clamps to be equally stretched with reduced “dead ends”, hence, maximizing the film areas to be reverse patterned. The stretched film was fully locked by soaking in 1M KOH solution, followed by reverse patterning of Miura-ori 2D pattern using 1M HCl solution, which was then wiped off after 40 s. Heating of the patterned film at 160 °C for 10 min gives the Nafion Miura-ori master mold.

2) Molding of PDMS Miura-ori secondary mold (Figure 1.18b)

The resulting Nafion Miura-ori master mold was used to make PDMS Miura-ori secondary mold following the procedure described in Section 1.2.

3) Erasing of Nafion Miura-ori to recover Nafion film (Figure 1.184c)

The permanent shape of Nafion was recovered by soaking the Nafion Miura-ori in 1M HCl solution for 1 h, followed by heating at 130-140 °C for 1 min.

4) Encoding and decoding of Nafion bow-tie master mold on Nafion film (Figure 1.18d)

The recovered permanent shape of Nafion was uniaxially stretched at room temperature to a strain of $\epsilon = 60\%$, followed by fixing under load for 10 min. The stretched film was fully locked by soaking in 1M KOH solution, followed by reverse patterning of bow-tie 2D pattern using 1M HCl solution, which was then wiped off after 40 s. Heating of the patterned film at 160 °C for 15 min produces the Nafion bow-tie master mold.

5) Molding of PDMS bow-tie secondary mold (Figure 1.18e)

The resulting Nafion bow-tie master mold was used to make PDMS bow-tie secondary mold following the procedure described in Section 1.2.

6) Erasing of Nafion bow-tie to recover Nafion film (Figure 1.18f)

The permanent shape of Nafion was recovered by soaking the Nafion bow-tie in 1M HCl solution for 1 h, followed by heating at 130-140 °C for 1 min.

7) Encoding and decoding of Nafion zigzag folds master mold on Nafion film (Figure 1.18g)

The recovered permanent shape of Nafion was uniaxially stretched at 125-130 °C to a strain of $\epsilon = 100\%$, followed by fixing under load while cooling to room temperature. The stretched film was fully locked by soaking in 1M KOH solution, followed by reverse

patterning three lines perpendicular to the stretching direction using 1M HCl solution. Two of these lines were patterned on the top of the film while the third line was patterned at the bottom of the film equidistant between the two lines patterned on the top of the film. Heating of the patterned film at 170 °C for 15 min yields the Nafion zigzag folds master mold.

8) Molding of PDMS zigzag folds secondary mold (Figure 1.18h)

The resulting Nafion zigzag folds master mold was used to make PDMS zigzag folds secondary mold following the procedure described in Section 1.2.

9) Erasing of Nafion zigzag folds to recover Nafion film (Figure 1.18i)

The permanent shape of Nafion was recovered by soaking the Nafion zigzag folds in 1M HCl solution for 1 h, followed by heating at 130-140 °C for 1 min.

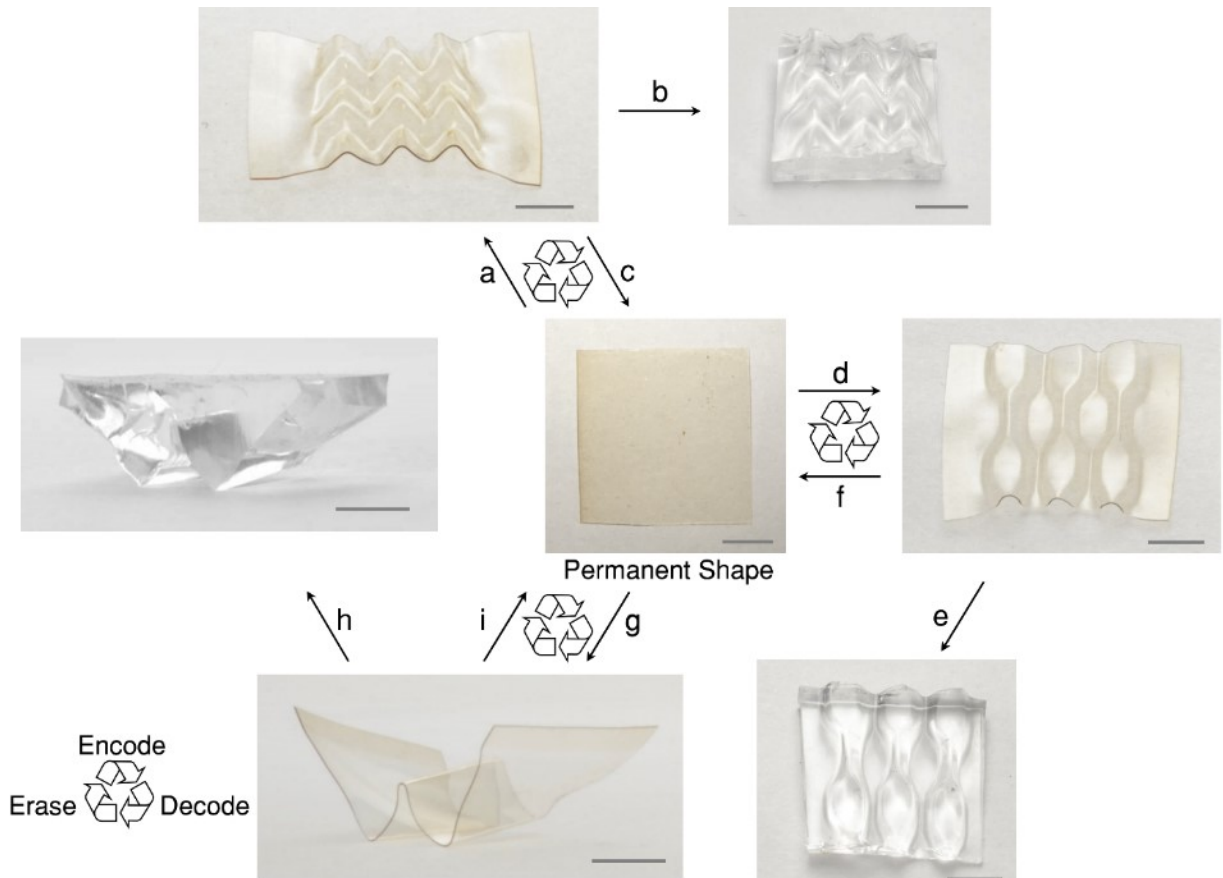


Figure 1.18. a) Encoding and decoding of Nafion Miura-ori master mold on Nafion film by uniaxial stretching, reverse patterning, and heating. b) Molding of PDMS Miura-ori secondary mold from a). c) Erasing of Nafion Miura-ori to recover Nafion film by 1M HCl treatment and heating. d) Encoding and decoding of Nafion bow-tie master mold on Nafion film by uniaxial stretching, reverse patterning, and heating. e) Molding of PDMS bow-tie secondary mold from d). f) Erasing of Nafion bow-tie to recover Nafion film by 1M HCl treatment and heating. g) Encoding and decoding of Nafion zigzag folds master mold on Nafion film by uniaxial stretching, reverse patterning, and heating. h) Molding of PDMS zigzag folds secondary mold from g). i) Erasing of Nafion zigzag folds to recover Nafion film by 1M HCl treatment and heating. Scale bar: 5 mm.

1.4. Conclusion

In summary, we successfully developed a reprogrammable 3D chemical shaping strategy for origami, kirigami, and reconfigurable molding based on reverse patterning of pre-stretched Nafion sheets. This shape-reprogramming of shape-memory polymers represents a thrilling new strategy to develop re-useable, sustainable materials for morphing technologies ranging from soft robotics, reconfigurable metamaterial, satellite deployment, medical implants and lab-on-a-chip. The key to this methodology is accessible and reversible acid–base chemistry that shifts the softening temperature of a shape-memory polymer. Such design concept is potentially amenable to other ionomers with sulfonic acid or carboxylic acid groups, as well as other polymers that can undergo reversible side-chain cross-linking such as cycloaddition or supramolecular reactions.³²⁻

35

This new strategy not only decouples the degree of shape complexity from the production cost and time, but also enables a versatile, low-cost, scalable process for 3D shaping of diverse materials, which could lead to new material functions and applications. Future studies include the development of new shape reprogrammable polymer materials and developing a computational topology optimizer that can directly predict an input pattern for a desired 3D output shape.

1.5. References

- (1) Y. Klein, E. Efrati, E. Sharon, *Science* **2007**, *315*, 1116-1120.
- (2) J. Kim, J. A. Hanna, M. Byun, C. D. Santangelo, R. C. Hayward, *Science* **2012**, *335*, 1201-1205.

- (3) H. Thérien-Aubin, Z. L. Wu, Z. Nie, E. Kumacheva, *J. Am. Chem. Soc.* **2013**, *135*, 4834-4839.
- (4) A. W. Hauser, A. A. Evans, J. -H. Na, R. C. Hayward, *Angew. Chem.* **2015**, *127*, 5524-5527; *Angew. Chem. Int. Ed.* **2015**, *54*, 5434-5437.
- (5) J. -H. Na, A. A. Evans, J. Bae, M. C. Chiappelli, C. D. Santangelo, R. J. Lang, T. C. Hull, R. C. Hayward, *Adv. Mater.* **2015**, *27*, 79-85.
- (6) R. M. Erb, J. S. Sander, R. Grisch, A. R. Studart, *Nat. Commun.* **2013**, *4*, 1712.
- (7) T. H. Ware, M. E. McConney, J. J. Wie, V. P. Tondiglia, T. J. White, *Science* **2015**, *347*, 982-984.
- (8) T. Xie, *Nature* **2010**, *464*, 267-270.
- (9) T. Xie, *Polymer* **2011**, *52*, 4985-5000.
- (10) R. R. Kohlmeier, M. Lor, J. Chen, *Nano Lett.* **2012**, *12*, 2757-2762.
- (11) G. J. Berg, M. K. McBride, C. Wang, C. N. Bowman, *Polym.*, *55*, **2014**, 5849-5872.
- (12) K. A. Page, K. M. Cable, R. B. Moore, *Macromolecules* **2005**, *38*, 6472-6484.
- (13) R. R. Kohlmeier, P. R. Buskohl, J. R. Deneault, M. F. Durstock, R. A. Vaia, J. Chen, *Adv. Mater.* **2014**, *26*, 8114-8119.
- (14) J. Rogers, Y. Huang, O. G. Schmidt, D. H. Gracias, *MRS Bull.* **2016**, *41*, 123-129.
- (15) S. Yang, I. -S. Choi, R. D. Kamien, *MRS Bull.* **2016**, *41*, 130-137.
- (16) Q. Zhao, W. K. Zou, Y. W. Luo, T. Xie, *Sci. Adv.* **2016**, *2*, e1501297.
- (17) N. Zheng, Z. Fang, W. Zou, Q. Zhao, T. Xie, *Angew. Chem.* **2016**, *128*, 11593-11597; *Angew. Chem. Int. Ed.* **2016**, *55*, 11421-11425.
- (18) S. Felton, M. Tolley, E. Demaine, D. Rus, R. Wood, *Science* **2014**, *345*, 644-646.

- (19) J. L. Silverberg, A. A. Evans, L. McLeod, R. C. Hayward, T. Hull, C. D. Santangelo, I. Cohen, *Science* **2014**, *345*, 647-650.
- (20) J. T.B. Overvelde, T. A. de Jong, Y. Shevchenko, S. A. Becerra, G. M. Whitesides, J. C. Weaver, C. Hoberman, K. Bertoldi, *Nat. Commun.* **2016**, *7*, 10929.
- (21) K. Kuribayashi, K. Tsuchiya, Z. You, D. Tomus, M. Umemoto, T. Ito, M. Sasaki, *Mater. Sci. Eng. A* **2006**, *419*, 131-137.
- (22) A. Lamoureux, K. Lee, M. Shlian, S. R. Forrest, M. Shtein, *Nat. Commun.* **2015**, *6*, 8092.
- (23) Z. Song, T. Ma, R. Tang, Q. Cheng, X. Wang, D. Krishnaraju, R. Panat, C. K. Chan, H. Yu, H. Jiang, *Nat. Commun.* **2014**, *5*, 3140.
- (24) R. V. Martinez, C. R. Fish, X. Chen, G. M. Whitesides, *Adv. Funct. Mater.* **2012**, *22*, 1376-1384.
- (25) R. R. Kohlmeier, J. Chen, *Angew. Chem.* **2013**, *125*, 9404-9407; *Angew. Chem. Int. Ed.* **2013**, *52*, 9234-9237.
- (26) Y. Koren, M. Shpitalni, *J. Manuf. Syst.* **2010**, *29*, 130-141.
- (27) M. Schlesinger, *Modern Electroplating*, 5th Edition, John Wiley & Sons, Inc., **2010**, 447- 458.
- (28) Tang, B.; Zheng, X.; Lin, T.; Zhang, S. *Dyes and Pigments* **2014**, *104*, 146-150
- (29) Y. Xia, G. M. Whitesides, *Angew. Chem.* **1998**, *110*, 568-594; *Angew. Chem. Int. Ed.* **1998**, *37*, 550-575.
- (30) Y. Takeoka, *J. Mater. Chem.* **2012**, *22*, 23299-23309.
- (31) D. Ge, L. Yang, G. Wu, S. Yang, *Chem. Commun.* **2014**, *50*, 2469-2472.
- (32) A. Lendlein , H. Jiang , O. Jünger , R. Langer , *Nature* **2005** , *434* , 879-882 .

- (33) J. Li , J. A. Viveros , M. H. Wrue , M. Anthamatten , *Adv. Mater.* **2007** ,19 , 2851-2855 .
- (34) C. J. Kloxin , C. N. Bowman , *Chem. Soc. Rev.* **2013** , 42 , 7161-7173 .
- (35) K. Liu , Y. Kang , Z. Wang , X. Zhang , *Adv. Mater.* **2013** , 25 , 5530-5548 .

Chapter 2: Multi-Length-Scale 3D Shaping of Nafion-Based Reconfigurable Polymer Composite

2.1. Introduction

Nature has provided scientists and engineers with exceptional examples of strong building materials. These materials usually show complex hierarchical organization from the nanometer to the macroscopic scale.¹⁻³ Multi-length scale hierarchical structures are responsible for many functions and properties such as for mechanical, optical, and wettability behavior found in biological materials, with every structural level contributing to the mechanical stability and toughness of the resulting design.^{3,4}

In the past few decades, there have been efforts in the development of advanced materials using bioinspired hierarchical approaches, such as the development of self-cleaning surface inspired by the self-cleaning ability of lotus leaf,⁵ high adhesive superhydrophobic materials inspired by the feet of gecko and barnacles;⁶⁻⁹ advanced anti-fogging material inspired by anti-fogging compound eyes of moth and fly;^{7,10-11} advanced mechanical materials inspired by sea shells,^{7, 12-16} advanced sensory materials inspired by structural hierarchy of various biological materials;¹⁷⁻²¹ advanced optical materials and structural colors inspired by vibrant butterflies and bird feathers.²²⁻²⁴ These structural hierarchy found in nature have motivated scientist and engineers to develop materials with useful functions.

However, most methods reported in the literature to mimic biological materials are experimentally complex and not flexible. For example, to make a hierarchical or multi-length scale pattern, a microstructured surface is fabricated in the first step and then further processing is carried out to add nano-features over it at the second step²⁵⁻²⁷ by combining different fabrication techniques with different resolutions making a whole process long, complicated and limited to a certain geometrical shape.^{4, 28-31} These complicated fabrication approaches have resulted in the scarcity of hierarchical engineered materials.

We have recently demonstrated the use of Nafion based reconfigurable polymer composite in creating various complex macroscale 3D structures by chemical means and using origami and kirigami principles. This macroscale approach relies on reverse patterning of the protonated or “unlocked” phase (dispersed phase) in a deprotonated or “locked” phase (matrix). Such approach so far has resulted in sharp folds with rigid facets accompanied by little or no material shrinkage, making it suitable for creating complex 3D origami and kirigami structures. On the otherhand, normal patterning (spatial patterning of the locked phase (dispersed phase) in an unlocked Nafion (matrix)) results in material shrinkage during shape decoding. Hence, using normal patterning or combination with reverse patterning may provide promising approach in achieving multi-length scale structures

Herein, we demonstrated the feasibility of obtaining multi-length scale 3D structure via a combination of 2D printing and normal chemical patterning (spatial patterning of the locked phase into a matrix of the unlocked) of a biaxially (*bs*-) stretched Nafion film. This multi-length scale 3D shaping strategy may provide scalable

approach to engineering of structural hierarchy and adaptive functions in polymers, which could lead to novel material properties and exciting new applications.

2.2. Experimental

2.2.1. Materials

Nafion N115 films (DuPont, $t = 127 \mu\text{m}$) were purchased through Ion Power, Inc. All as-received Nafion films were annealed at $140 \text{ }^\circ\text{C}$ in nitrogen for 2h to reach their equilibrium states followed by soaking in 1M HCl for at least 1 h. Biaxially stretched (*bs*-) Nafion films were stretched using an in-house mechanical stretcher at elevated temperature to a targeted strain. ^[1,2] Unless otherwise stated, the locking agent (printing ink) used was 1M KOH solution.

3.2.2. 2D Printing

Prepared printing ink (1M KOH) was loaded to a 3 ml syringe attached by a luer-lock to a smooth-flow nozzle (blunt tip dispensing needle, gauge 32). An air-powered fluid dispenser (Ultimus V, EFD) helps provides the required pressure to deposit the ink unto the *bs*-Nafion_{H+}. The patterns were printed using a robot (Nordson Pro 4) through the combination of movement of the stage and printing head in the x-y- direction. The printed patterns were generated either using the robot's inbuilt program (DispenseMotion software) or DraftSight and exported as Drawing eXchange Format (.DXF) to be read by the robot. The *bs*-Nafion was placed on a stage with a nozzle height of $\sim 60 \mu\text{m}$ (0.75 times the nozzle diameter). Through the control of the gauge height, dispensing pressure and time, microdots of an average diameter of $350 \mu\text{m}$

were deposited on *bs*-Nafion_{H+}. Microdots spacing are between 500-700 μm depending on the nature of the targeted structure. After, printing, the printing ink was allowed to sit on the *bs*-Nafion_{H+} for ~ 4 min followed by heating at 150 $^{\circ}\text{C}$ for 3-5 min .

2.3. Results and Discussion

2D printing provides an attractive, non-lithographic approach to obtaining ordered pattern for meeting the demand for large scale designs and production. In 2D printing method, a concentrated ink is extruded through a nozzle (e.g. syringe), onto a substrate which is translated using a two-axis (x-y), motion-controlled stage and/or printing head. Typically, the size of the 2D pattern or ink deposited depends on a number of factors including the diameter of nozzle, rheology of the ink, extrusion pressure and time.

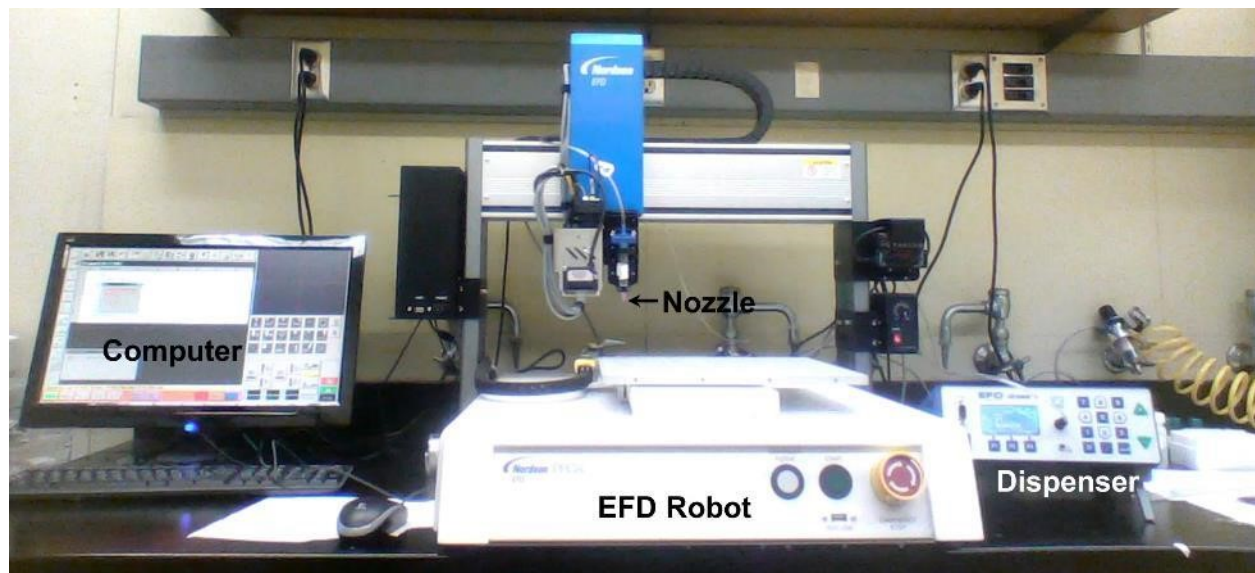


Figure 2.1: Photograph of 2D printer showing the robot, computer, dispenser and nozzle. Both the print head and stage have with two degree of freedom (DOF) in the x and y-direction.

Printing was done using a robot (Nordson EFD Pro4) which includes a specialized DispenseMotion™ software with a fully integrated CCD smart vision camera and three types of feedback – contact, optical, and non-contact laser height sensing which ensures absolute accurate fluid placement (Figure 2.1). An air-powered fluid dispenser (Ultimus V, EFD) helps provides the required pressure to deposit the ink unto the *bs*-Nafion_{H+} (Figure 2.1). Through careful selection of nozzle diameter, dispensing pressure and time, series of patterns consisting of microdots were deposited onto *bs*-Nafion. Heating of such patterned *bs*-Nafion results in various hierarchical bumpy 3D shapes at macro- and microscale (Figures 2.2-2.4).

Bumpy surfaces are found in nature and are utilized by various organisms for different functions. For example, the Namibia desert beetle surface is made up of macroscopic bumpy surface, with hydrophilic and hydrophobic patterns, which are utilized for water condensation and harvesting. Previous studies have shown that a biaxially stretched Nafion film with circular dot patterning experiences buckling in the locked area, as well as shrinking in the unlocked area in response to heating, which leads to the formation of dome structures that resemble the profile of a 3D Gaussian shape.³² Such combination of buckling and shrinkage in Nafion film is promising for creation of multi-length scale structures similar to those found in nature.

In this work, we focused on demonstration of feasibility of obtaining microscale and multi-length scale structure using *bs*- Nafion film in combination with 2D printing. Specifically, we focused on obtaining 2- and 3-length scale hierarchical structures based on microdomes arrays. Structures with 2 - length scale hierarchy are defined by the characteristic of having primary domes (microscale domes) and secondary domes

(milli- or centimeter scale domes), with the secondary domes being a result of the synergistic effect of the primary domes while 3 - length scale hierarchy are defined by the characteristic of having primary domes, secondary domes, and tertiary domes with the secondary domes being a result of the synergistic effect of the primary domes and the tertiary domes being a result of the synergistic effect of the secondary domes.

We demonstrate 2 - length scale hierarchical bumpy structures mimicking some organisms found in nature using microdot patterns in a spiral and square arrangement (Figures 2.2, 2.3). For example, Romanesco broccoli is a plant resembling a cauliflower with self-similar buds and meristems arranged in a logarithm spiral which continues at several smaller levels (Figure 2.2a).³³ Inspired by the self-cleaning ability of the surface of these class of plants, we patterned series of microdots in a spiral arrangement to obtain a 2-length scale hierarchical structure consisting of micro-and millimeter scale structure mimicking the *Romanesco* broccoli was obtained (Figure 2.2b-d). Individual microdomes making up the 2-length scale structure were found to be $\sim 350 \mu\text{m}$ in diameter as shown in the SEM images (Figures 2.2e,f).

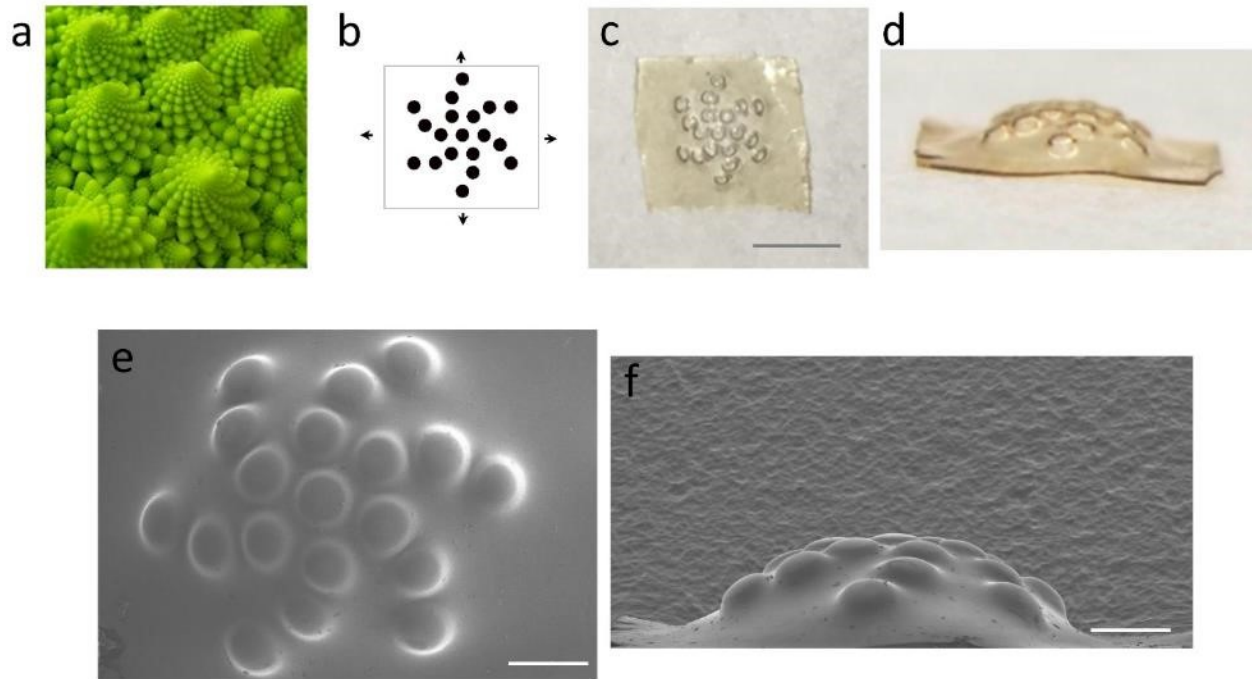


Figure 2.2: Hierarchical 3D shaping on macro- and microscale inspired by *Romanesco* Broccoli. a) Image of *Romanesco* broccoli showing spiral shaped hierarchical structure. b) Spiral 2D pattern of microdots. c-d) Top and side view of Nafion hierarchical structure consisting of series of microscale domes on a millimeter scale larger dome, respectively. Scale bar: 2 mm. e-f) SEM image (e) top, (f) side view, of spiral shaped hierarchical structure. Scale bar: 500 μ m. Black arrows indicate the film stretching direction. T_{def} : 130-140 $^{\circ}$ C

Arrangement of patterns or microstructures plays significant role in the efficiency of some processes and functions needed for survival. For example, based on the structure of cactus stem, which is densely covered with cones, Ju *et. al.* fabricated cone arrays with different arrangements/orientations using a combination of mechanical perforation and template replica molding. They found that a hexagonal arrangement of cone array proves to be more efficient in water collection or harvesting.³⁴ Inspired by the desert beetle which is able to collect water on its bumpy back surface from early morning fog, we showed the feasibility of obtaining multi-length scale structure with square array

of microdot patterns (Figure 2.3) to mimic the bumpy back of the desert beetle. Such macro- and microscale structure inspired by the desert beetle may find application in water harvesting. Future studies may investigate the water harvesting capability of such macro- and microscale structure. In addition, investigation of different arrangement of microdots such as triangular, helical e.t.c on *bs*-Nafion may confer additional functionality and efficiency for some application.

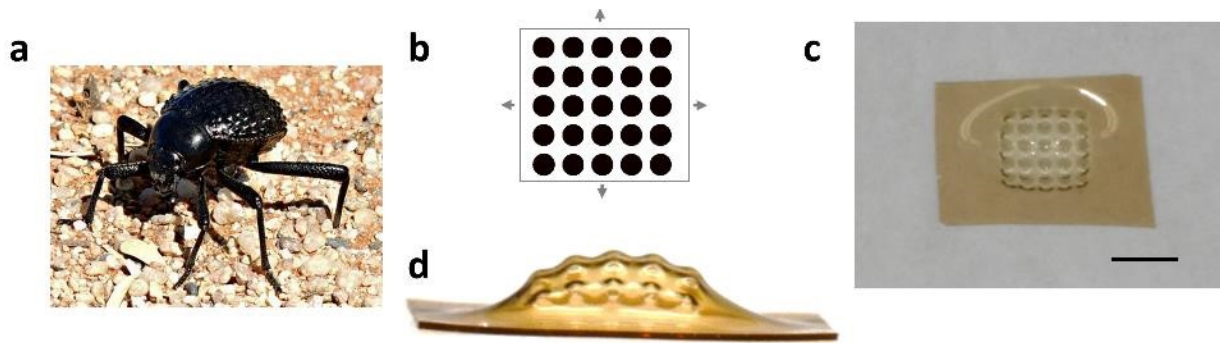


Figure 2.3: Hierarchical 3D Shaping on macro- and microscale inspired by *Desert Beetle*. a) Image of desert beetle showing macroscale bumps. b) Square 2D pattern of microdots. c-d) Top and side view of Nafion hierarchical structure obtained after heating *bs*-Nafion patterned with square array of microscale domes. Scale bar: 2 mm. T_{def} : 130-140 °C

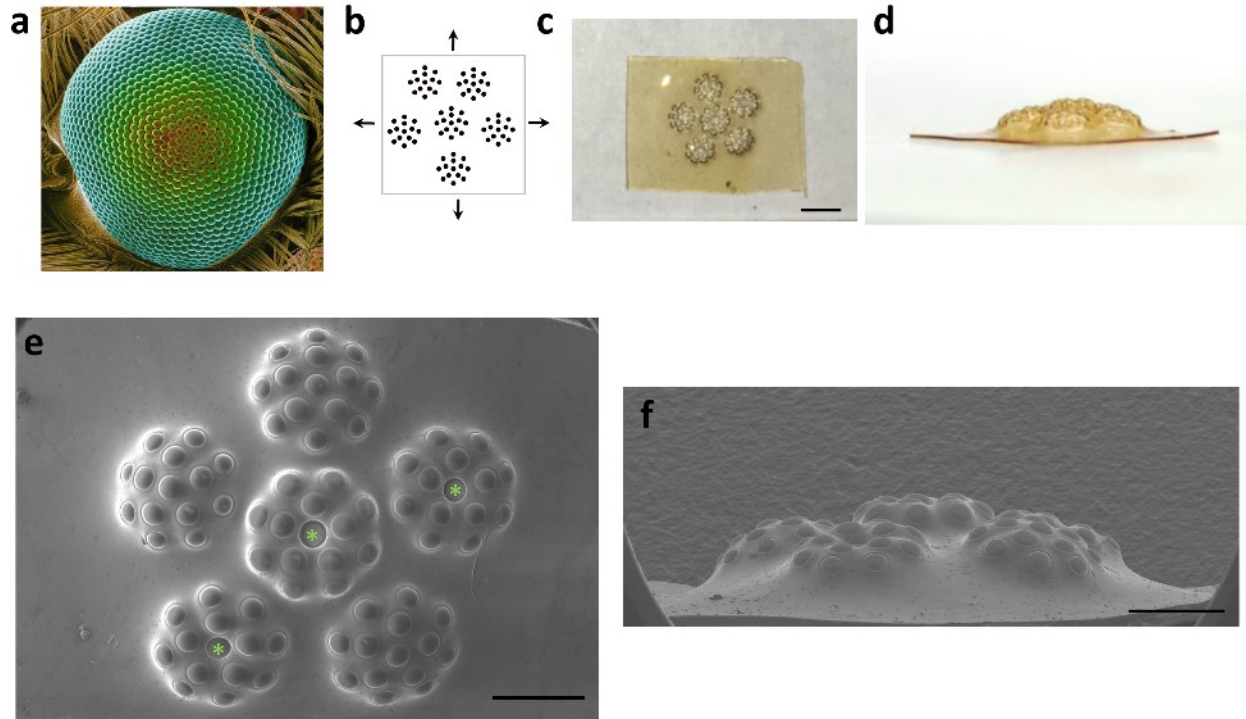


Figure 2.4: 3- Length scale hierarchical 3D shaping on macro- and microscale inspired by moth eye. a) Image of moth eye. b) Radial 2D pattern of microdots. c-d) Top and side view of hierarchical structure obtained after heating *bs*-Nafion patterned with radial array of microscale domes. Scale bar: 2 mm. e-f) SEM image (e) top, (f) side view, of hierarchical structure. Green asterisks represent defects. Scale bar: 1 cm. Black arrows indicate the film stretching direction. T_{def} : 130-140 °C

Hierarchical structures found in nature are usually based on multiple length scales (usually more than two length scales). Building on our success demonstration of 2-length scale hierarchical structure by combining 2D printing and normal patterning, we demonstrate the possibility of obtaining a 3- length scale hierarchical structure consisting of microdome arranged in a radial pattern (mimicking moth eye) in *bs*-Nafion (Figure 2.4). Structures with 3 - length scale hierarchy are defined by the characteristic of having primary domes, secondary domes, and tertiary domes with the secondary domes being a result of the synergistic effect of the primary domes and the tertiary domes being a result of the synergistic effect of the secondary domes. In other to

achieve synergistic effect of the secondary domes to give a 3-length scale structure, careful control of inter-distance between micro patterns for both secondary and primary structures are important. Such control allows for individual microdomes to be formed independently while still giving synergistic effect to form the multi-length scale structure.

So far, large scale printing of hierarchical structures on *bs*-Nafion have resulted in some defects. SEM images reveal these defects arise from microdomes folding in opposite direction relative to the patterned side (Figure 2.4e). One possible cause of the defects is the occurrence of a different diffusion gradient of the locking agent through the *bs*-Nafion film after deposition. Previous studies have reported through a combination of FE modeling and EDX mapping that the direction of bend or gaussian shaped domes depends on the diffusion behavior of the locking reagent through the film.³³ The three possible scenarios include uniform through thickness, diffusive concentration (or partial locking) and completely locked diffusive gradient are possible upon deposition of locking reagent on Nafion. In the case of structures in Figures 2.2-2.3, direction of dome formation indicates a partial locking gradients while in Figure 2.4, majority of the microdomes form through partial locking except for the defects which fold in the opposite direction relative to the patterned side suggesting completely locked gradient in the defective sites.

The elimination of defects in multi-length scale 3D structures relies mainly on the ability to better control the diffusion of the locking reagent through the thickness of the film such that either partial or complete locking gradient of the locking reagent is achieved for all patterned microdots. Both complete and partial gradient locking have been reported to result in similar gaussian dome on *bs*-Nafion and bend in *us*-Nafion.

Since diffusion depends on concentration, size of molecule, viscosity of media and thickness, systematic study of how these factors affects the locking gradient of *bs*-Nafion may be worth exploring in other to eliminate the defects and allow for several centimeter large scale hierarchical structures. For example, addition of a second solvent which is compatible with Nafion may be used to simultaneously tune the viscosity of the locking reagent and diffusion time through the thickness of the film. Alternatively, using bulky organic amines or reducing the concentration of the KOH in the locking reagent may result in all microdomes forming in same direction thereby eliminating defects.

2.4. Conclusion

In conclusion, we successfully demonstrated multi-length scale (2- and 3-length scale hierarchical structures) by prescribing 3D hierarchical structure in form of a 2D patterns in a *bs*-Nafion sheet using 2D printing technology. 2D printing will allow for rapid, large-area printing of arbitrary patterns with a hierarchy of length scales tunable for different application. Such large-scale hierarchical structure consisting of series of domes are useful for water harvesting and condensation, optical property tuning, antifouling and reconfigurable molding.

2.5. References

- (1) G. Mayer, M. Sarikaya, *Exp. Mech.* 2002, 42, 395-403
- (2) S. Kamat, X. Su, R. Ballarini, A. H. Heuer, *Nature*. 2000, 405,1036-1040
- (3) Aizenberg, J, Weaver, J.C, Thanawala, M.S., Sundar, V.C. , Morse, D.E., r Fratzl, *P. Science*, **2005**, 275-277
- (4) Abid, M. I., Wang, L., Chen, Q. D., Wang, X. W., Juodkazis, S., Sun, H. B. *Laser Photonics Rev.*, **2017**, 11, 1600187.
- (5) W. Barthlott, W., Neinhuis, C., *Planta* **1997**, 202, 1–8 .

- (6) Xia , F., Jiang , L., *Adv. Mater.* **2008** , 20 , 2842-2858 .
- (7) Tao, P., Shang, W., Song, C., Shen, Q., Zhang, F., Luo, Z., Deng, T., *Adv. Mater.* **2015**, 27, 428-463.
- (8) K. Liu , K., Yao , X., Jiang , L., *Chem. Soc. Rev.* **2010** , 39 , 3240-3255 .
- (9) Liu , K., Du , J., Wu , J., Jiang, L., *Nanoscale* **2012** , 4 , 768 -772 .
- (10) Gao, X., Yan, X., Yao, X., Xu, L., Zhang, K., Zhang, J., Yang, B., Jiang, L., *Adv. Mater.* **2007**, 19, 2213–2217.
- (11) Z. Sun, Z., Liao, T., Liu, K., Jiang, L., Kim, J.H., Dou, S.X., *Small* **10**, 2014, 3001–3006.
- (12) Li , Y., Yu , T., Yang , T., Zheng , L., Liao, K., *Adv. Mater.* **2012** . 24 , 3426-3431 .
- (13) E. Munch , E., Launey , M.E., Alsem , D. H., Saiz , E., Tomsia , A. P., Ritchie, R. O., *Science* **2008** , 322 , 1516-1520.
- (14) G. M. Luz , G. M., Mano, J. F, *Philos. Trans. R. Soc. A* **2009** , 367 , 1587-1605 .
- (15) Fratzl P., *J. R. Soc., Interface* **2007** , 4 , 637-642 .
- (16) Yao , H. Fang , H., Wang , X., Yu, S., *Chem. Soc. Rev.* **2011**, 40 , 3764-3785 .
- (17) Grande , J.C. , Zorn , G., Goddard , G., Zalubovsky, S. *Proc. Natl. Acad. Sci. USA* **2013** , 110 , 15567.
- (18) Potyrailo , R. A. , Ding , Z., Butts , M. D., Genovese , S. E., Deng , T., *IEEE Sens. J.* **2008** , 8 , 815-822 .
- (19) Potyrailo , R. A., Ghiradella , H., Vertiatchikh , A. , Dovidenko , K., Cournoyer , J. R., Olson , E., *Nat. Photonics* **2007** , 1 , 123-128.
- (20) Yang , Q., Zhu , S., Peng , W., Yin , C., Wang , W., Gu , J., Zhang , W., Ma , J. , Deng , T., Feng , C., Zhang , D., *ACS Nano* **2013** , 7 , 4911-4918.
- (21) Zarzar , L. D. , Kim , P., Aizenberg, J., *Adv. Mater.* **2011** , 23 , 1442-1446.
- (22) Kong, Y. L. , Gupta, M. K. , Johnson, B. N., McAlpine, M. C., *Nano Today*, **2016**, **11**, 330–350.
- (23) Jie, Y., Jiang, Q., Zhang, Y., Wang, N., Cao, X., *Nano Energy.* **2016**, 27, 554–560.

- (24) Yang, J., Luo, F., Kao, T. S., Li, X., Ho, G.W., Teng, J., Luo, X., Hong, M., *Light Sci. Appl.* **2014**, 3, e185.
- (25) Wu, D., Chen, Q. D., Xia, H., Jiao, J., Xu, B. B., Lin, X. F., Xu, Y., Sun, H. B., *Soft Matter*, **2010**, 6, 263–267.
- (26) Choi, S. J., Choi, M. K., Tahk, D., Yoon, H., *J. Mater. Chem.* **2011**, 21, 14936–14940.
- (27) Zhang, F., Chan, J., Low, H. Y., *Appl. Surf. Sci.* **2008**, 254, 2975–2979.
- (28) Golovin, K., Lee, D. H., Mabry, J. M., Tuteja, A., *Angew Chem. Int. Edit.* **2013**, 52, 13007–13011.
- (29) Wang, J. N., Zhang, Y. L., Liu, Y., Zheng, W., Lee, L. P., Sun, H. B., *Nanoscale*, **2015**, 7, 7101–7114.
- (30) Nguyen, T. P. N., Boukherroub, R., Thomy, V., Coffinier, Y., *J. Colloid Interf. Sci.* **2014**, 416, 280–288.
- (31) Malinauskas, M., Zukauskas, A., Hasegawa, S., Hayasaki, Y., Mizeikis, V., Buividas, R., Juodkazis, S., *Light Sci Appl.* **2016**, 5, e16133.
- (32) R. R. Kohlmeyer, P. R. Buskohl, J. R. Deneault, M. F. Durstock, R. A. Vaia, J. Chen, *Adv. Mater.* **2014**, 26, 8114-8119.
- (33) Kieffer, M., Fuller, M..P., Jellings, A.J. *Planta.* **1998**, 206, 34–43.
- (34) Ju, J., Yao, X., Yang, S., Wang, L., Sun, R., He, Y., Jiang, L. *Adv. Funct. Mater.*, **2014**, 24, 6933-6938.

PART II

Chapter 3: A versatile strategy for transparent stimuli responsive interference coloration

3.1. Introduction

Structural coloration arises from the physical interaction of light with micro- or nanostructures via a variety of optical mechanisms, including thin-film interference, multilayer interference, diffraction gratings, photonic crystals, and scattering.^{1,2} Compared with pigmentary coloration, structural coloration is not only more resistant towards the color degradation caused by environmental conditions, but also easily tunable via changes in structural parameters or refractive index.

In nature, responsive structural coloration towards various environmental stimuli has been used by some organisms for camouflage, predation, communication, etc. The bioinspired stimuli-responsive structural coloration has received great interest from the scientific and engineering communities in the past two decades, and it offers a wide range of promising applications in medical diagnostics, advanced packaging, environmental and building monitoring, adaptive camouflage, intelligent coatings and textiles, and anti-counterfeiting.²⁻¹²

While remarkable progress has been made in the field of responsive structural coloration based on photonic crystals and multilayer interference, how to make high-quality responsive structural coloration systems on large scale at low cost still remains a challenge.⁹ Thin-film interference is the simplest structural coloration mechanism, which

is responsible for the colorful, iridescent reflections that can be seen in oil films on water, and soap bubbles.^{1,2} Owing to its design simplicity, which does not require multilayers of materials with alternative refractive indices or micro- and nanostructures, thin film interference represents a promising solution towards scalable and affordable manufacturing of high-quality responsive structural coloration systems.

Although structural coloration based on thin film interference is well known,^{1,2,13} research on stimuli-responsive thin film interference has been mainly limited to materials such as reflectin proteins,^{14,15} multilayers of polyelectrolytes,¹⁶ and hydrogels,¹⁷ which are typically deposited on nontransparent substrates such as silicon wafer. Compared with other substrates such as glass, single crystalline silicon wafer is relatively expensive to produce and has limited area size. For many potential applications, low-cost substrates other than monocrystalline silicon wafer are highly desirable. For example, the glass substrate can be used for applications where large-area structural coloration is required. In addition, transparent glass substrate is required for smart window-related applications. However, thin films of polymers with appropriate thickness that are directly deposited on glass generally do not exhibit visible structural colors (Figure 3.1d and e).

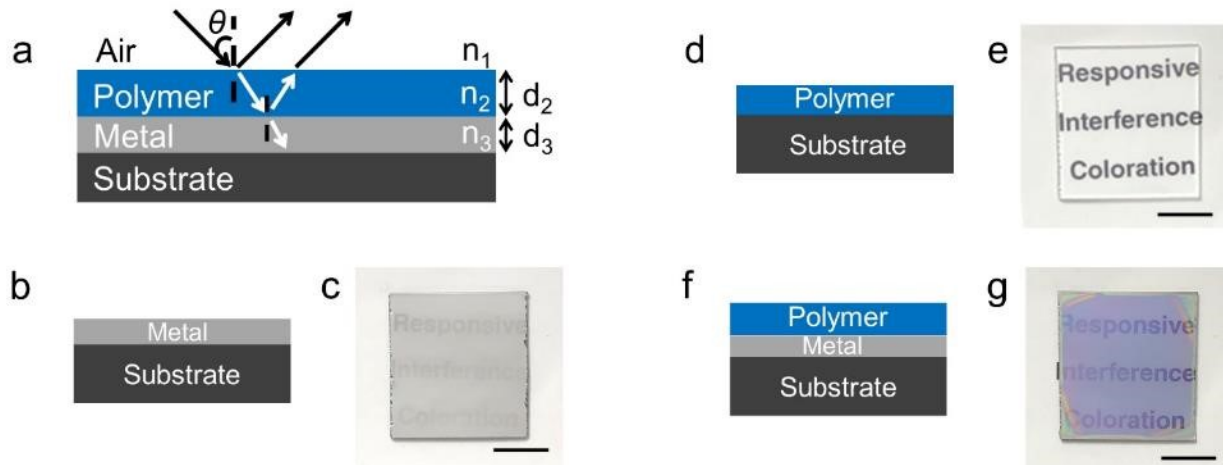


Figure 3.1. The interference coloration principle. (a) A polymer-metal-substrate trilayer RIC design. (b,c) The Ir-glass film. (d,e) The Nafion-glass film with the polymer layer thickness comparable to that in (g). (f-g) Photographs of the Nafion-Ir-glass film. d_3 : (b-g) 5 nm. Scale bars: 1 cm.

Herein, we report a versatile new strategy that enables scalable and affordable manufacturing of transparent stimuli-responsive interference coloration (RIC) systems. Our RIC system is composed of three layers (Figure 1a): 1) The thin polymer layer that exhibits stimuli-responsive thin film interference coloration; 2) The ultrathin metal layer that acts as an optical filter; 3) The substrate layer. The key concept in our work is to use an ultrathin metal layer as an optical filter instead of high refractive index substrate or highly reflective substrate. Such an optical filter layer allows tuning of the degree of transparency, the constructive interference reflection light, and complementary destructive interference transmission light via changing the metal layer thickness.

Our simple RIC system has the following distinctive advantages: 1) Versatile polymer layer choice: A wide range of thermoplastics, thermosets, and polymer composites can be used for rational engineering of stimuli-responsivity, stability, etc. 2) Versatile metal layer choice: A variety of metals and metal alloys such as iridium, silver,

nichrome, etc. can be selected for target applications and manufacturing processes. 3) Versatile substrate choice: Our RIC design is applicable to many substrates, including glass.

The glass has been selected as a transparent substrate, and different polymers have been chosen as the polymer layer candidates in this study (Figure 4.2), including polyvinylpyrrolidone (PVP), polyvinylpolypyrrolidone (PVPP), which is a crosslinked PVP, polydimethylsiloxane (PDMS), polycarbonate (PC), and Nafion.

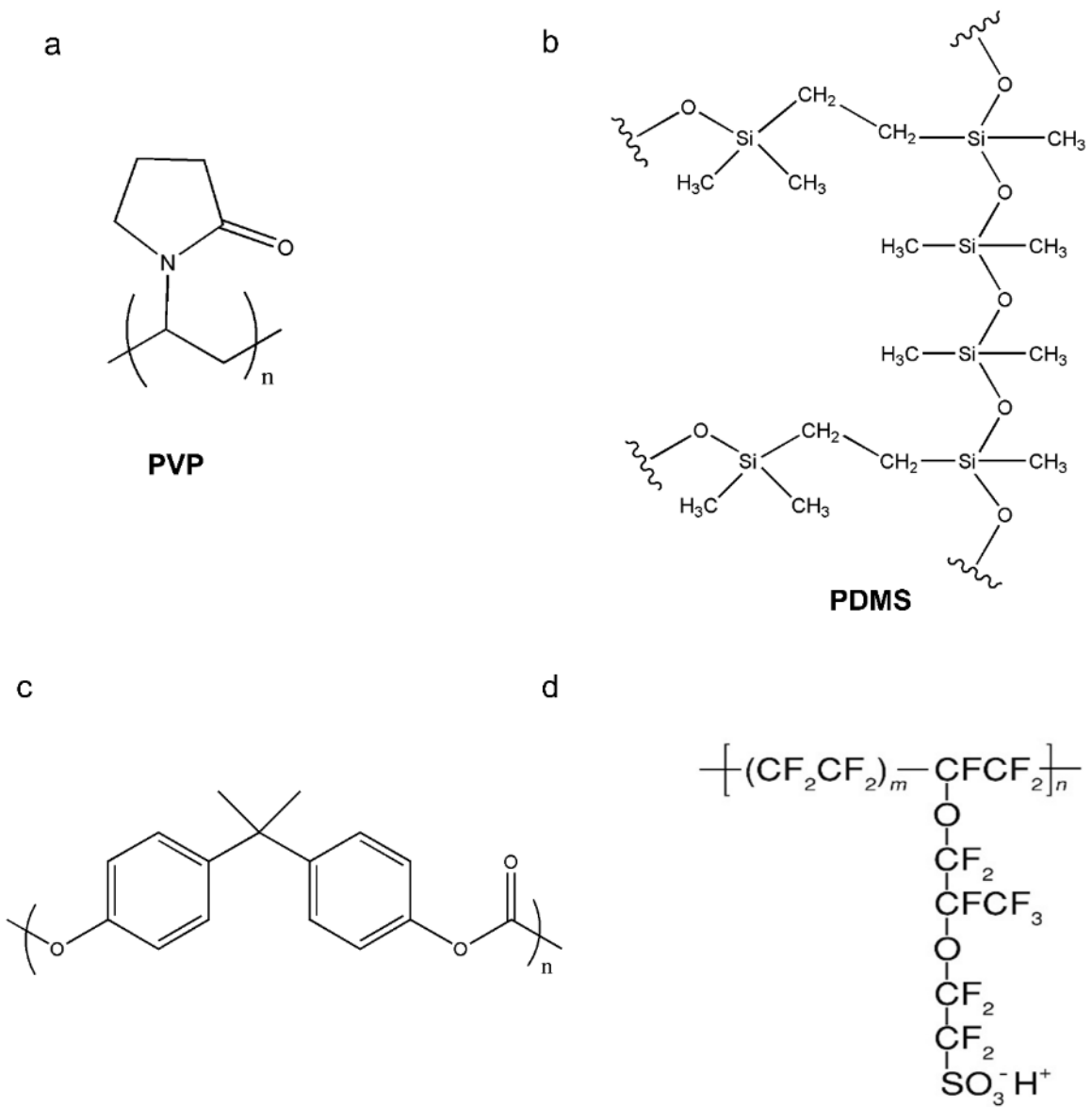


Figure 3.2. Chemical structures of PVP (polyvinylpyrrolidone), PDMS (polydimethylsiloxane), and PC (polycarbonate) and Nafion used in fabrication of the thin-film interference coloration.

3.2. Experimental Section

3.2.1. Materials.

PVP powder was purchased from Alfa Aesar. PC pellets was purchased from Sigma-Aldrich. PDMS precursors (Sylgard 184) were purchased from Dow Corning, and mixed based on the manufacturer's recommended base to crosslinker ratio of 10:1. PVP solutions in ethanol with PVP loadings from 6 to 9 wt%, PC solutions in chloroform with PC loading of 2 wt%, and PDMS solutions in hexane with PDMS precursors loading of 8 wt% were prepared and stored at room temperature. 5% w/w stock Nafion alcohol solution was purchased from Alfa Aesar and was concentrated to 7-8 wt% by gentle evaporation. Ethanol (200 proof) was purchased from Koptec. Chloroform and hexane were acquired from Sigma-Aldrich. Nichrome wire and high purity aluminum wire (diameter: 0.015 inches) were purchased from Ted Pella Inc. High purity silver wire was purchased from Integrity Beads, Inc. Glass substrates (Micro Slides), were purchased from Corning. Glass microscopic slides were rinsed with acetone and isopropanol and then dried with nitrogen prior to use.

3.2.2. Preparation of Metal Layer.

Ultrathin film of iridium is deposited on a desired substrate in a sputter coating system (model K150X, Quorum Emitech) using a high purity iridium target (Ted Pella, Inc.) under a vacuum pressure of 2×10^{-3} mbar. Ultrathin films of nichrome and aluminum were deposited using a thermal vacuum evaporation system (Edwards Coating System Inc., model E-306A) under a vacuum pressure of 2×10^{-4} mbar.

3.2.3. Preparation of Responsive Interference Coloration (RIC) Films on Glass Substrates.

After ultrathin film of metal was deposited on a glass substrate (2.5 cm × 2.5 cm), ~ 0.5 mL of the solution of desired polymer (PVP, PC, Nafion, or PDMS) was placed on top of the metal-coated glass substrate. The spin coating was carried out at specific spinning rates for 30 seconds using a spin coater (model P6700, Specialty Coating Systems, Inc.). Since the reflected color is controlled by the polymer layer thickness, appropriate spinning rate and concentration of the polymer solution were used to obtain the desired color. Unless otherwise stated, the entire process was performed at ambient humidity (45 ± 5 RH%) and room temperature (22 ± 2 °C).



Figure 3.3. Schematic illustration of the preparation of the thin films of polymer on metal-coated substrates.

3.2.4. Sample Characterizations.

The reflection spectra were acquired using a fiber optic spectrometer (USB2000+, Ocean Optics). The incident light was perpendicular to the plane of the film. The transmission and absorption spectra of the samples were recorded with a Cary 5000 UV-Vis-NIR spectrophotometer. Scanning electron microscopy (SEM) was performed using a Hitachi S-4800 field emission scanning electron microscope. The average polymer layer thickness was determined from SEM measurements of 50 location points of the cross

section of the polymer layer. Thickness of the substrates were measured with a Mitutoyo Digital Micrometer. Unless otherwise stated, all sample characterization was carried out at ambient humidity (45 ± 5 RH%) and room temperature (22 ± 2 °C).

3.2.5. Stimuli Response Measurements.

The static response measurement of the RIC films to different humidity levels was carried out in a home-built humidity-control chamber based on literature.^{18,19} The RH level of the chamber was varied between 20% and 70% by controlling the relative flow rates of dry and wet N₂ gas. Under each humidity condition, the film was kept for 2 hours to ensure fully equilibrated state. The chamber's RH level was monitored with a commercial humidity meter (AcuRite 01083), calibrated with standard salt solutions (Appendix 1).²⁰ The chemical vapors (i.e. water and hexane vapors) for localized, dynamic response experiments were generated by a commercial ultrasonic humidifier (Essential Oil Diffuser, Radha Beauty Co.), and then applied to the samples through a rubber tubing with a small plastic tip (e.g. pipette tip) at the end. The dynamic reflection spectra were acquired continuously using a fiber optic spectrometer (USB2000+, Ocean Optics) with the interval time of 10 ms. Thermal response experiment was performed on a hot plate, and temperature of the RIC film during the experiment was measured with a non-contact infrared thermometer (MICRO-EPSILON thermoMETER LS), which was found to be in good agreement (within ± 2 °C) with a traditional thermometer.

3.2.6. Verification of Humidity Sensing Mechanism.

To determine the reflection peak wavelength of the RIC film at different static RH levels, the sample was placed inside a homemade, transparent humidity chamber. The

RH level of the chamber was varied between 20% and 70% by controlling the relative flow rates of dry and wet N₂ gas, and it was monitored with the calibrated commercial humidity meter. Under each humidity condition, the static reflection spectrum was recorded using a fiber optic spectrometer (USB2000+, Ocean Optics) after the film reached equilibrium state.

To verify whether the humidity sensing mechanism of the PVP-Ir-glass film is due to the change in thickness of the PVP layer, we calculated the reflection peak position at each increased static RH level using the expected thickness of the PVP layer at corresponding static RH level. The expected thickness of the PVP layer was estimated using the coefficient of hygroscopic expansion of PVP, with respect to the original thickness of the PVP layer measured by SEM. Comparison of the observed and calculated reflection peak positions at each static RH level was then used to determine whether the observed reflection wavelength change is caused by change in thickness of the PVP layer.

3.2.7. Humidity Cycle Test.

To investigate the long-term stability of the RIC films, both PVPP-Ir-glass and PVPP-nichrome-glass films were subjected to 50 cycles of localized exposure to water vapor in the same region. The dynamic reflection spectra ($\theta = 0^\circ$) were acquired continuously using a fiber optic spectrometer (USB2000+, Ocean Optics) with the interval time of 10 ms during the cycle #1, cycle #25, and cycle #50 of the humidity sensing experiments.

3.3. Results and Discussion

3.3.1. Metal Coating

In this study, iridium was mainly used as the metal to be coated on the desired substrates, mainly due to its availability. Thin films of iridium were coated on the substrates using a sputter coating system equipped with a film thickness monitor (FTM) quartz crystals which monitors the thickness of the metal deposited and terminates the coating once the pre-set thickness is reached. The FTM controller operates by monitoring the frequency shift of an oscillating quartz crystal as iridium is deposited on the crystal. The frequency shift is related to the mass of the deposited iridium.

3.3.2. Thin-Film Interference Coloration

In this work, the thin polymer layer serves as an interference coloration layer, where the reflected color represents the constructive interference, whereas the transmitted color represents the destructive interference. Without the thin polymer layer, the metal-glass film exhibits only light grayish color (Figure 3.1b and c). The condition for constructive thin-film interference is determined by Equation 3.1:

$$m\lambda = 2n_2d_2\cos\theta \quad (3.1)$$

where λ is the wavelength giving the maximum reflectivity, m is the order of diffraction (a positive integer), d_2 and n_2 are the thickness and refractive index of the polymer layer, respectively, and θ is the angle of incidence (Figure 3.1a).^{1,2} The condition for the destructive thin-film interference follows Equation 3.2:

$$(m-1/2)\lambda = 2n_2d_2\cos\theta \quad (3.2)$$

where λ represents the wavelength giving the minimum reflectivity (maximum transmissivity).^{1,2}

We have found that the thickness of the ultrathin metal layer is crucial to tune the intensity of the reflected light color.²¹ Without the metal layer, there is no detectable interference color for the polymer layer on glass (Figure 3.1b and c). If the metal layer is too thick, then all wavelengths of light could be reflected, which significantly diminishes the intensity of the reflected interference color.²¹ In this work, the ultrathin metal layer serves as an optical filter instead of highly reflective substrate, which can filter out unwanted wavelengths of light by transmission. The metal layer with appropriate thickness can simultaneously tune both the constructive interference reflection light and complementary destructive interference transmission light for various applications.²¹ To verify this concept, the peak wavelength was calculated for the constructive interference reflection spectra and destructive interference transmission spectra in a PVP-Ir-glass system based on Equation 3.1 and 3.2, respectively, using $n_2=1.53$ for the refractive index of PVP, $\theta=0^\circ$ for the angle of incidence, and the experimentally-measured thickness (d_2) of the PVP film. The result shows that the calculated peak wavelengths are in reasonably good agreement with corresponding experimental reflection and transmission spectra, respectively.²¹

According to Equation 3.1, the thickness of the polymer layer determines the reflected color wavelength when the viewing angle is fixed (e.g. $\theta=0^\circ$). By tuning the polymer layer thickness via spin coating using appropriate spin speeds and

concentrations of polymer solutions, various interference colors including purple, blue, green, yellow, and red can be generated by thin films of various polymers such as PVP, PDMS, Nafion, and PC on metal-coated glass substrates (Figure 3.4). Owing to the transparency of glass, both constructive interference reflected colors and complementary destructive interference transmitted colors across the spectrum can be created simultaneously on opposite sides of the substrate, respectively.²¹ In addition, the degree of transparency in the interference system can be tuned via changing the thickness of the ultrathin metal film.²¹ Such transparent films with coupled complementary colors on opposite sides are desirable for applications such as wearable sensors, where the color change at the on-body side can be transduced into the color change on the opposite side of the film.

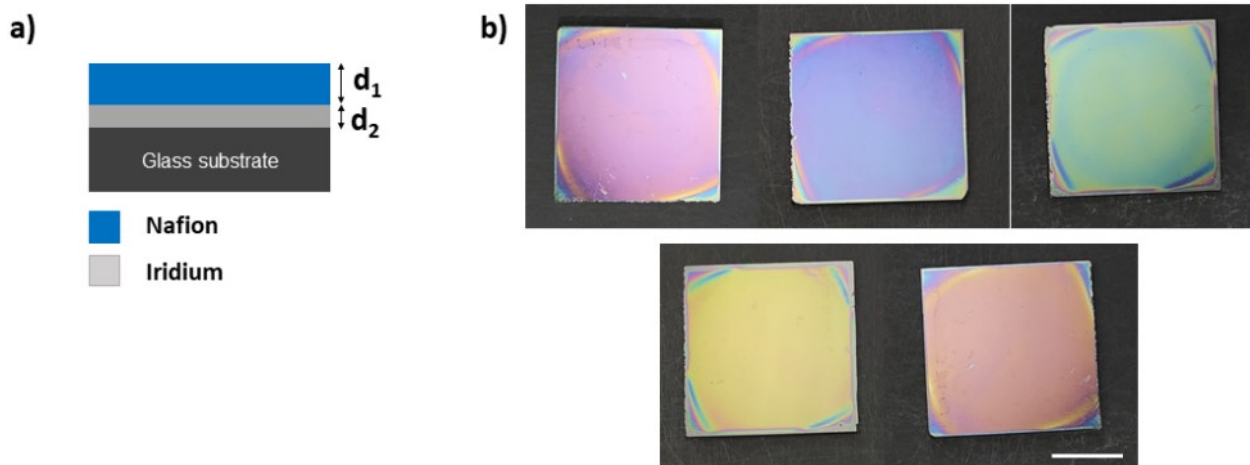


Figure 3.4. a) Schematic representation of the thin-film layered structure consisting of Nafion/iridium/ glass. b) Photograph of full spectrum colors generated by thin film of Nafion deposited on iridium-coated glass. Thickness (d_2) of iridium = 5 nm. Scale bar: 1 cm.

Our RIC design is applicable to a variety of metals and metal alloys, including iridium, nichrome, silver²¹ and aluminum. Since the silver has very low refractive index ($n=0.05$ at 589 nm), this supports that the ultrathin metal layer serves as an optical filter instead of high refractive index substrate. In addition, interference color patterns can be produced by patterning of the ultrathin metal film with a plastic stencil mask on top of a glass substrate during the metal deposition. Although the thicker metal layer leads to diminished interference color intensity, the RIC trilayer system can be put on additional metal substrates without negatively affecting its reflected color intensity.²¹

3.3.3. Colorimetric Responsive Interference Coloration (RIC) Humidity Sensor

Compared with most inorganic materials, polymer-based materials have many advantages such as low cost, flexibility, good processability, excellent corrosion resistance, and light-weight. Moreover, stimuli-responsive polymers can sense their environment and change the shape and/or material properties accordingly.²² In our current colorimetric RIC sensor design, the primary sensing mechanism is based on the stimulus-induced thickness change in the polymer layer, which leads to corresponding color change. In this study, we focus on the proof-of-concept demonstration of real-time, continuous, colorimetric RIC sensors for humidity (Figure 3.9-3.19), organic vapor (Figure 3.20-3.24), and temperature.²¹ The main advantages of such RIC sensors include low cost, zero power consumption, spatial and temporal resolution, fast, dynamic, and reversible response.

There has been a growing interest in low-cost, real-time humidity sensors for applications in agriculture, manufacturing, food industry, healthcare, and environmental

monitoring.²³ The PVP-Ir-glass colorimetric sensor exhibits excellent sensitivity to relative humidity (RH) change, ranging from purple at 20% RH to blue at 40% RH, green at 50% RH, yellow at 70% RH (Figure 3.14), and red²¹ at 80% RH. This is because the hygroscopic PVP layer swells in a high humidity environment and shrinks in a low humidity environment. Furthermore, the PVP-Ir-glass sensor shows fast, dynamic, and reversible response both spatially and temporally towards the water vapor. To further investigate the humidity sensing properties, we have conducted the dynamic reflectance spectroscopy study (Figure 3.5-3.9), which is more reliable and accurate than the video imaging in measuring the stimulus response and recovery time. It takes only ~ 1.1 s for the peak wavelength for the second-order of reflection to undergo ~ 200 nm of shift from the blue-colored to red-colored PVP film in response to the water vapor (Figure 3.6a, Figure 3.7). After the removal of the water vapor, it takes ~ 2.9 s for the red-colored PVP film to be fully recovered to the original blue-colored film (Figure 3.6b, Figure 3.8-3.9). For comparison, both PDMS-Ir-glass and PC-Ir-glass systems do not respond to the water vapor (Figure 3.10). Heating of a PVP thin film at 200 °C leads to thermal crosslinking of PVP to form more stable PVPP, which is insoluble in common solvents.²⁴ We have found that thermal crosslinking of PVP can significantly enhance the stability of PVP-based humidity sensors towards liquid water (Figures 3.11, 3.12). Compared with the PVP-based humidity sensor, the PVPP-Ir-glass sensor exhibits similar sensitivity towards the humidity change while remains intact after dipped into liquid water (Figure 3.13).

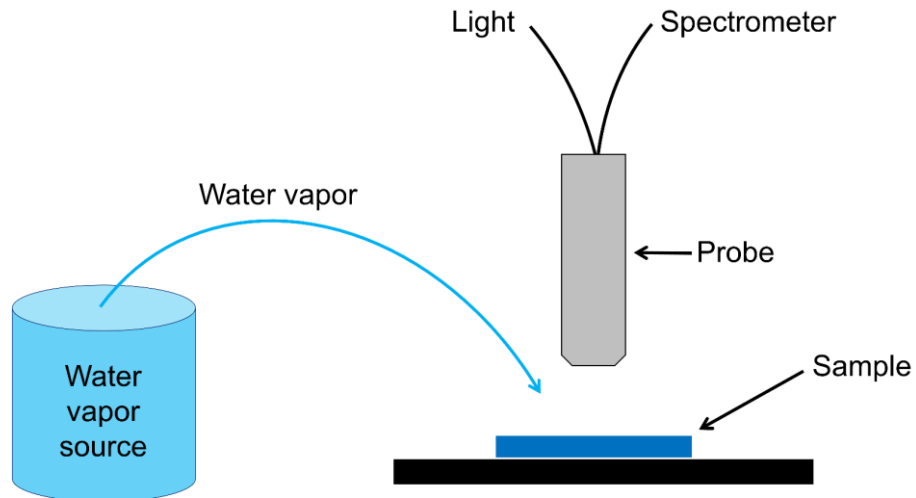


Figure 3.5. Experimental setup for the dynamic reflectance spectroscopy study. The fiber optic is oriented perpendicularly to the substrate and points to the color-changing region in the RIC film. Reflectance spectra for the response and recovery of the RIC films to the stimulus vapor is acquired continuously using a fiber optic spectrometer (USB2000+, Ocean Optics) with the interval time of 10 ms.

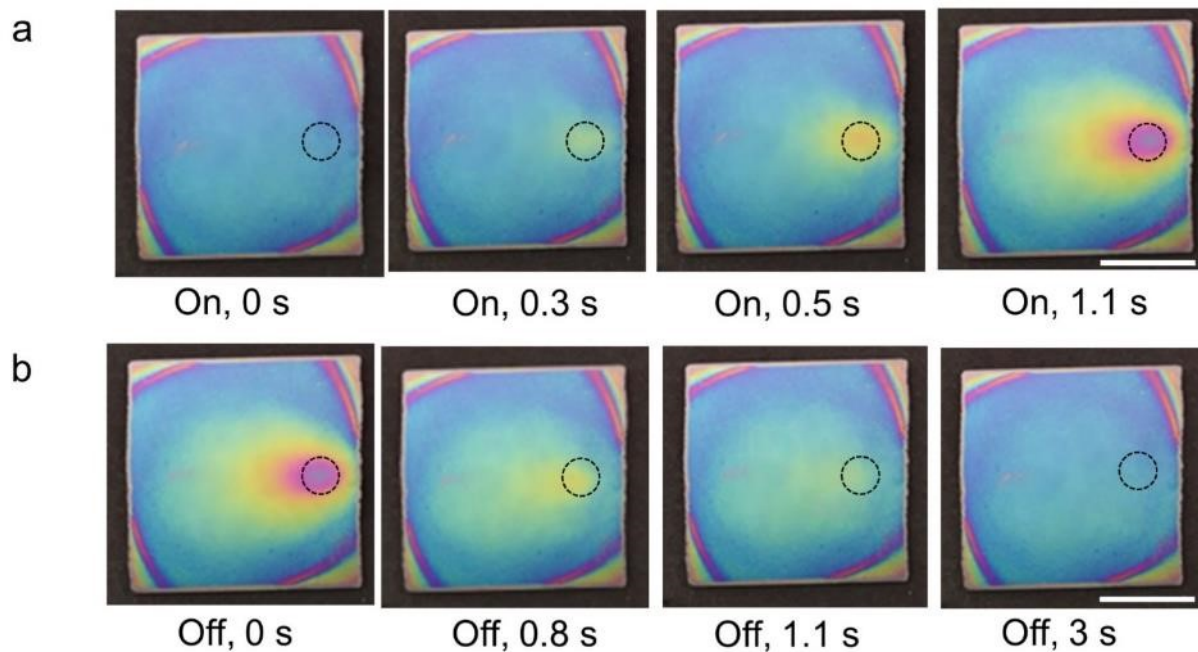


Figure 3.6. a,b) Photographs (top view) of the PVP-Ir-glass film in (a) response to and (b) recovery from the localized exposure to water vapor, respectively. d_3 : 5 nm. Scale bars: 1 cm.

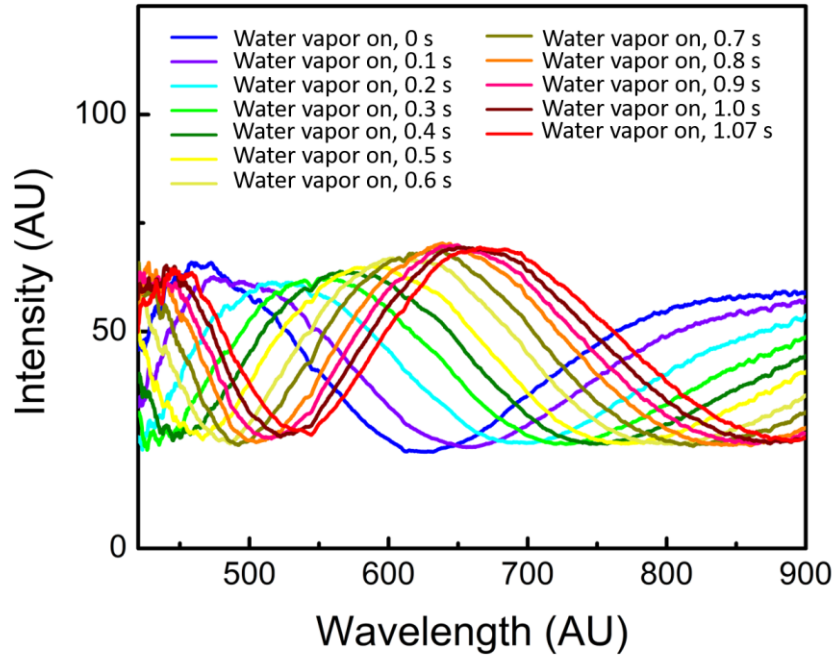


Figure 3.7. Dynamic reflectance spectra ($\theta = 0^\circ$) of the PVP-Ir-glass film in response to water vapor.

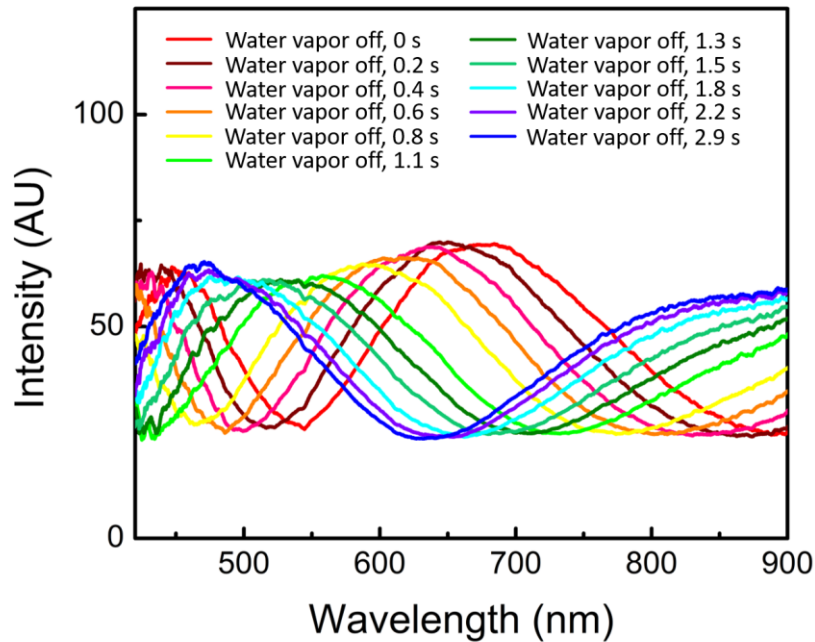


Figure 3.8. Dynamic reflectance spectra ($\theta = 0^\circ$) of the PVP-Ir-glass film in recovery from water vapor.

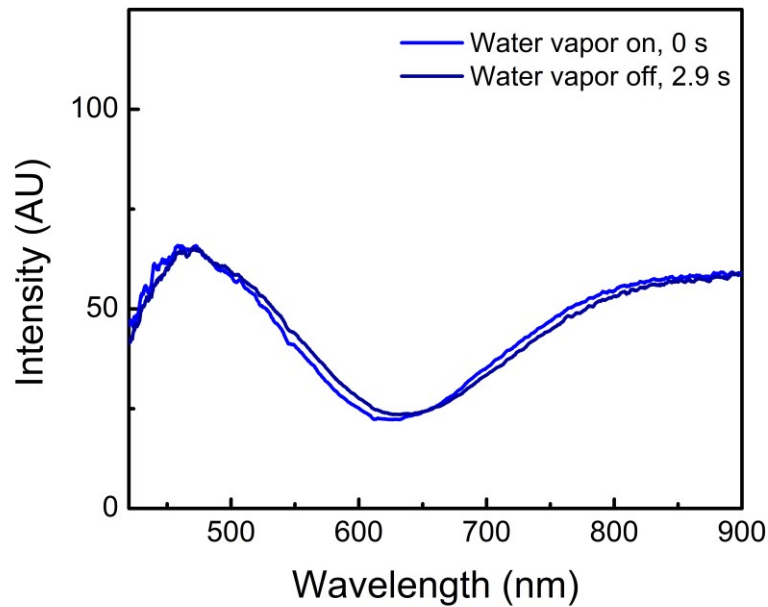


Figure 3.9. Reflection spectra ($\theta = 0^\circ$) of the PVP-Ir-glass film before and after exposure to water vapor.

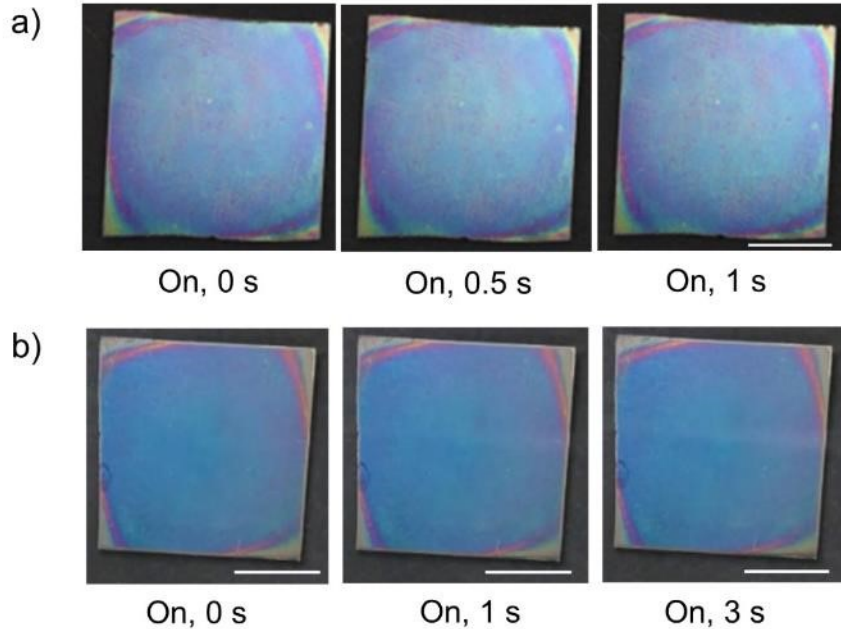


Figure 3.10. a-b) No response and color change when (a) PDMS-Ir-glass film, and (b) PC-Ir-glass are exposed to hexane vapor. d_3 : 5 nm. Scale bars: 1 cm.

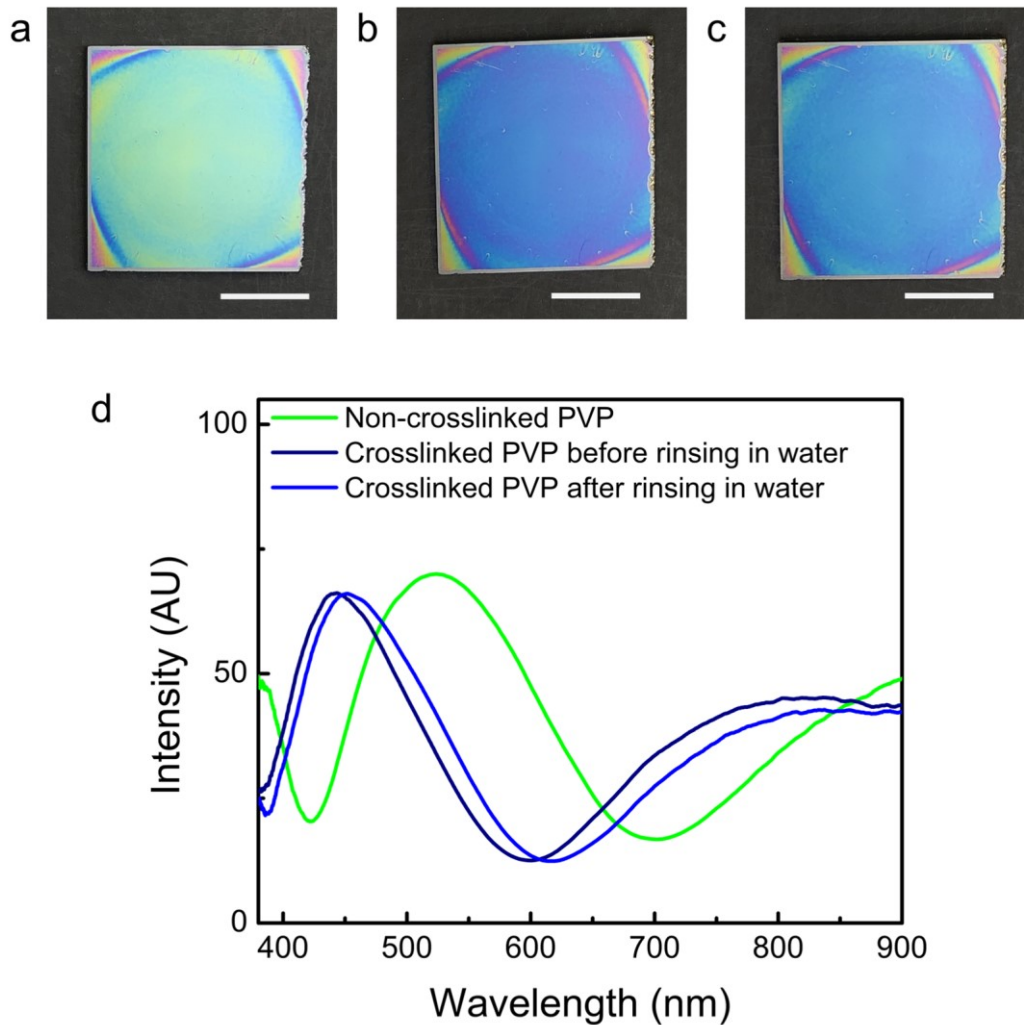


Figure 3.11. a) Photograph (top view) of the green-colored PVP-Ir-glass film before thermal crosslinking. b) Photograph of the resulting blue-colored PVPP-Ir-glass film after heating at 200 °C for 1.5 h, which leads to thermal crosslinking of PVP to form PVPP and decrease in film thickness. c) Photograph of the blue-colored PVPP-Ir-glass film after rinsing in DI water to remove any unreacted PVP residue. d) Corresponding reflection spectra ($\theta = 0^\circ$) of the films in (a-c), respectively. d_3 : 5 nm. Scale bars: 1 cm.

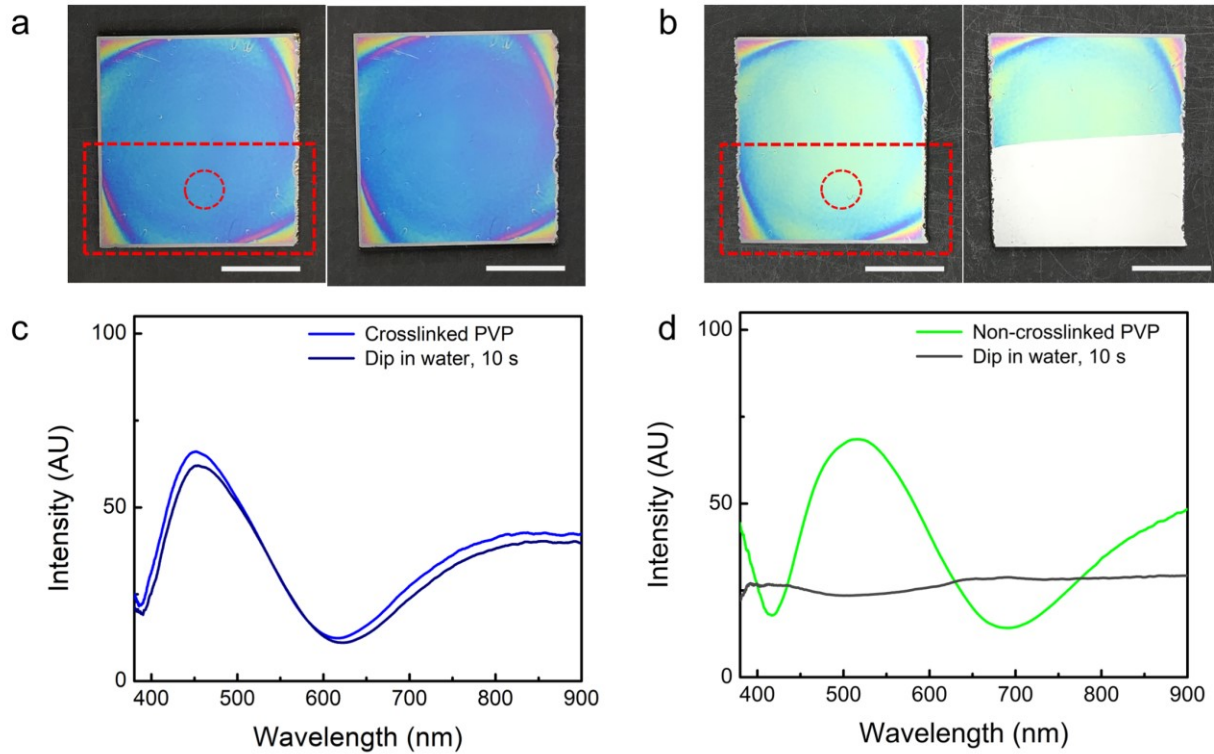


Figure 3.12. a) Photographs (top view) of the PVPP-Ir-glass film before (left) and after dipping of lower part in water for 10 s followed by blow drying with nitrogen (right). Red broken rectangle indicates the dipped region. Since PVPP is insoluble in water, the RIC film remains intact after dipping into the water. b) Photographs (top view) of the PVP-Ir-glass film before (left) and after dipping of lower part in water for 10 s followed by blow drying with nitrogen (right). Red broken rectangle indicates the dipped region. Since PVP is soluble in water, the PVP layer in the dipped region is removed after dipping into the water. c) Reflectance spectra ($\theta = 0^\circ$) of encircled region in (a) before and after dipping test. d) Reflectance spectra ($\theta = 0^\circ$) of encircled region in (b) before and after dipping test. d_3 : 5 nm. Scale bars: 1 cm.

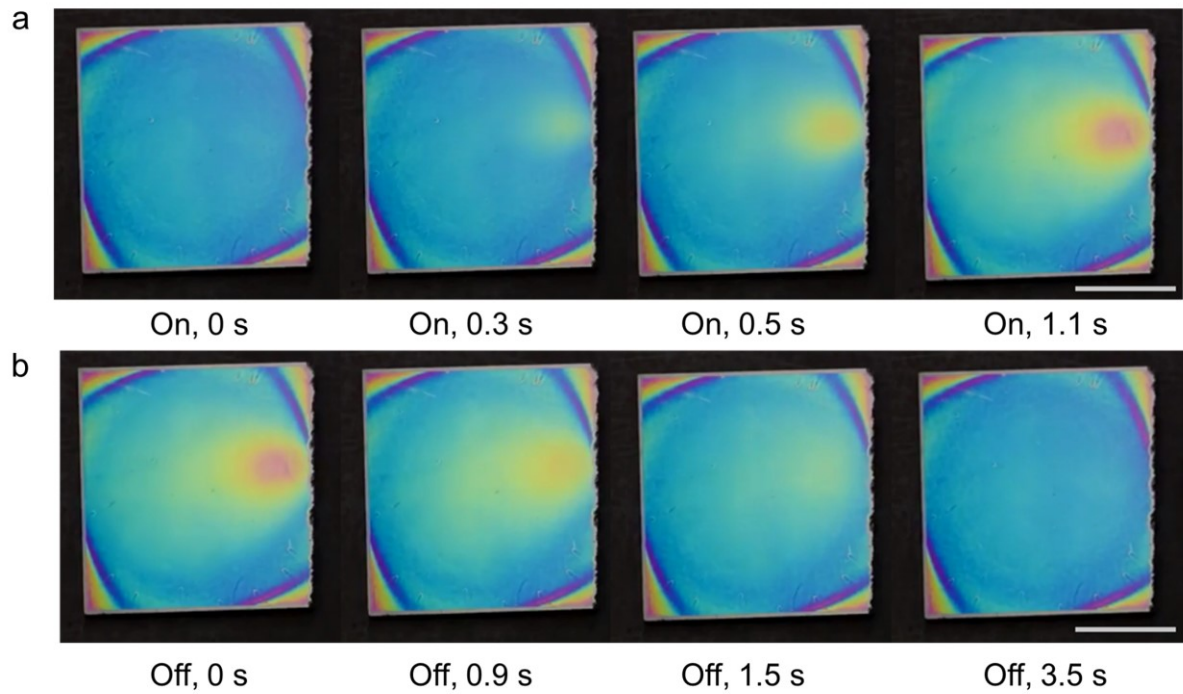


Figure 3.13. Photographs (top view) of the PVPP-Ir-glass film in (a) response to and (b) recovery from the localized exposure to water vapor, respectively. d_3 : 5 nm. Scale bars: 1 cm.

3.3.4. Estimating the Thickness of the PVP Layer Using the Coefficient of Hygroscopic Expansion of PVP.

To verify whether the humidity sensing mechanism of the PVP-Ir-glass film is due to the change in thickness of the PVP layer, we calculated the reflection peak position at each increased static RH level using the expected thickness of the PVP layer at corresponding static RH level. The expected thickness of the PVP layer was estimated using the coefficient of hygroscopic expansion of PVP, with respect to the original thickness of the PVP layer measured by SEM. The volumetric change induced by water absorption in PVP can be estimated as: ²⁵

$$\beta = \frac{\rho_w f W}{300} \quad (3.3)$$

Where β is the coefficient of hygroscopic expansion, f is the fraction of the water that contributes to an increase in the PVP volume,²⁶ ρ_w is the density of water, and W is the water uptake of PVP at 25 °C at specific RH level. As shown in the literature, the water absorption of PVP increases with relative humidity in a non-linear trend.²⁷ Hence, hygroscopic strain (ε_h) of PVP should be obtained at various RH levels according to Equation 4.4.²⁸

$$\varepsilon_h = \beta \cdot W \quad (3.4)$$

The hygroscopic strain of PVP determines expected thickness (d) of PVP at each static humidity level with respect to an initial thickness (d_0) according to Equation 4.5.

$$\varepsilon_h = \frac{d-d_0}{d_0} \quad (3.5)$$

The resulting thickness (d) can be used to predict the expected reflection peak position of PVP using the equation for the condition for constructive thin-film interference as described in equation 3.1.

Our comparison study shows that there is a good agreement between experimental and theoretical results, and the reflection peak wavelength increases with increase in relative humidity (Figures 3.14c, 3.15). This study confirms the proposed humidity sensing mechanism that is based on the thin film interference principle (Equation 3.1) and water vapor-induced swelling of the PVP layer (Figure 3.14a,b).

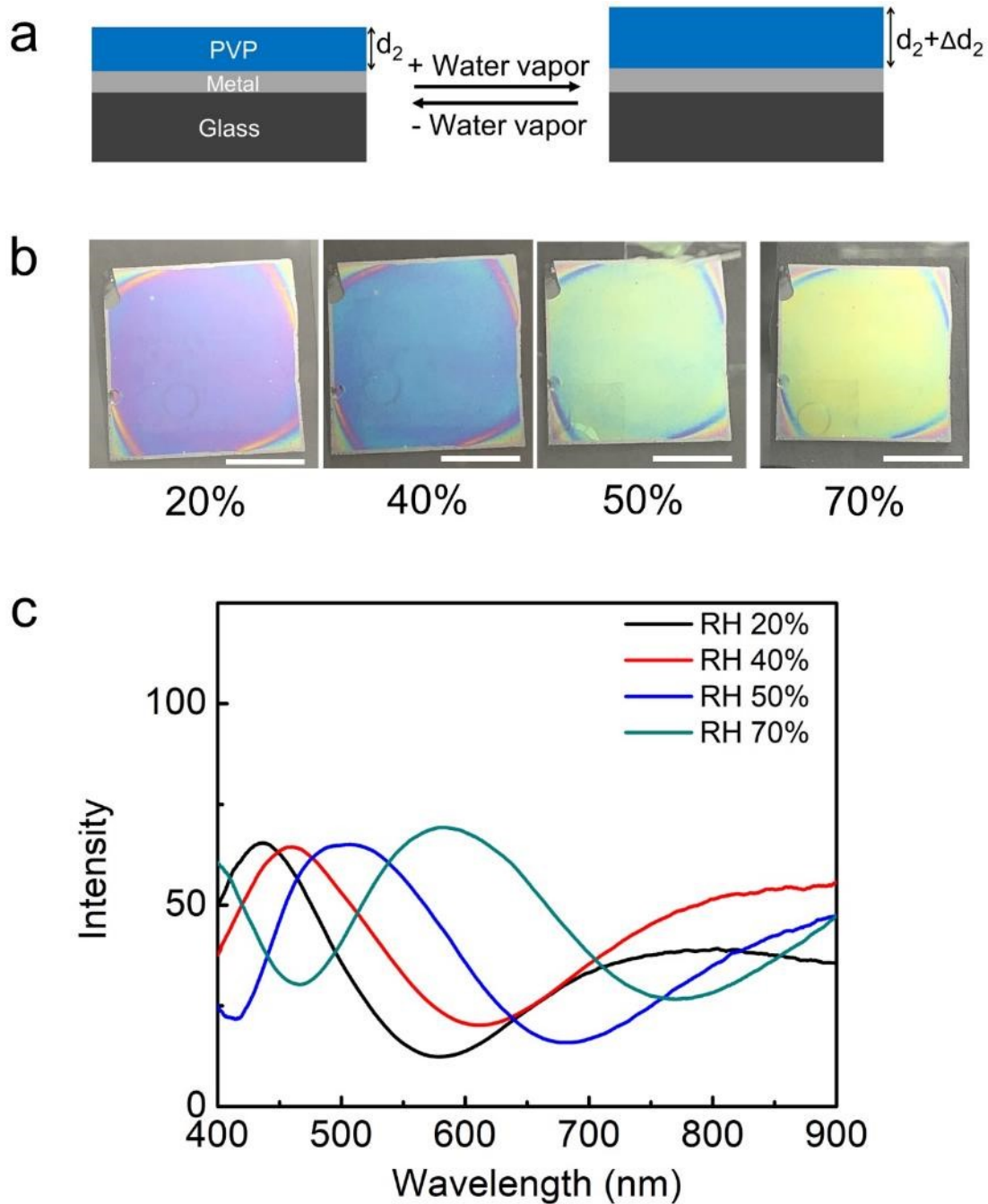


Figure 3.14 (a) Scheme of sensing mechanisms for water vapor. (b) Photographs (top view) of the PVP-Ir-glass film at different static humidity levels. (c) Reflectance spectra of PVP-Ir-glass at different static humidity levels between 20 and 70%. d_3 : 5 nm. Scale bars: 1 cm.

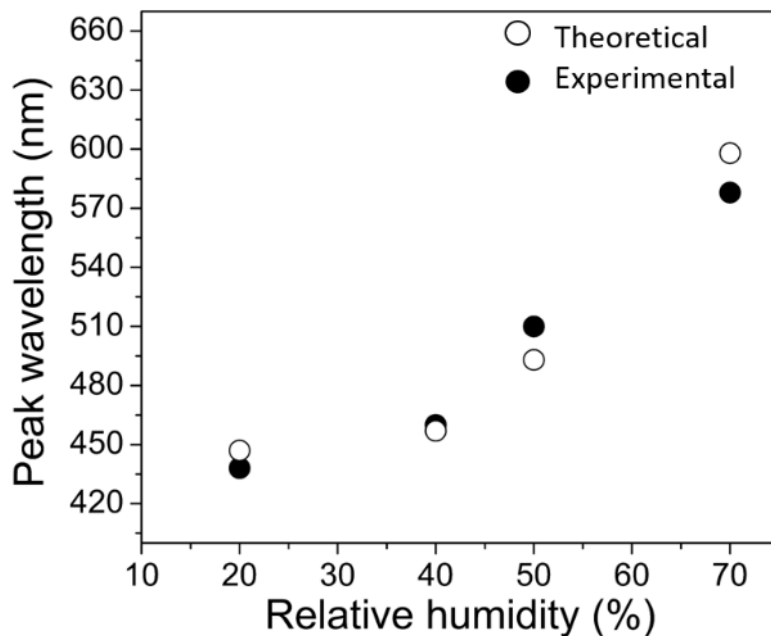


Figure 3.15. Humidity sensing mechanism. Comparison of the experimental and theoretical reflection peak positions for the PVP-Ir-glass at different static RH levels between 20 and 70%.

3.3.5. Humidity Cycle Test and Long-Term Stability of PVPP based Humidity Sensor.

To investigate the long-term stability and whether there is an oxidation effect of the metal substrate on the color of the RIC films, we have carried out the humidity cycle test for PVPP-Ir-glass and PVPP-nichrome-glass RIC films (Figures 4.16 - 4.19). Our humidity cycle test shows that there is no detectable change in both reflection spectra and color in the test region of the RIC films after 50 cycles of humidity sensing experiments (Figure 3.16, 3.18). In addition, the humidity sensing performance such as wavelength shift, and corresponding response time of the RIC films remain little changed during the humidity cycle test (Figure 3.17,3.19). However, compared with the

PVP-based RIC films , the PVPP-based RIC films exhibit smaller wavelength shift at the similar response time, most likely due to the crosslink structure of PVPP. Tuning the degree of thermal crosslinking may help increase the wavelength shift to be comparable to that of PVP-based RIC films. Future studies may investigate the effect of the degree of crosslinking on both wavelength shift and stability of the PVPP-based RIC sensors.

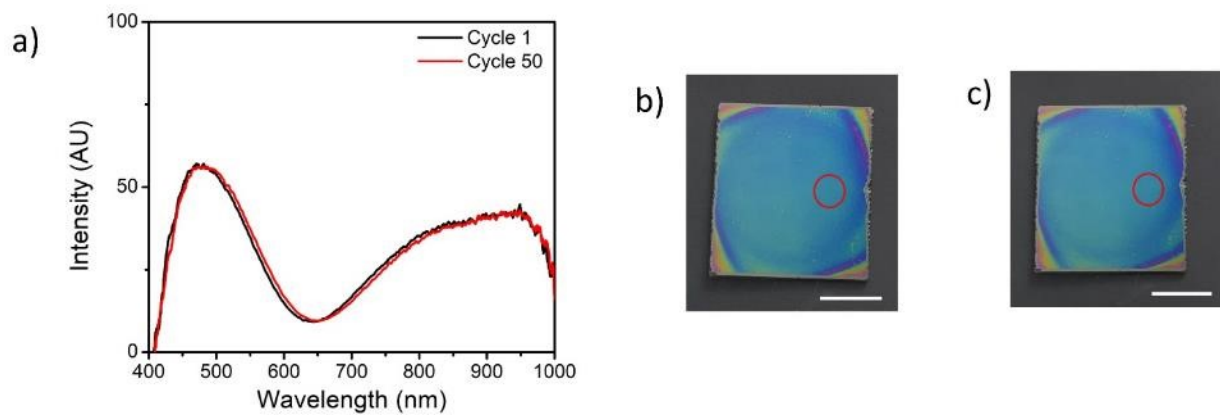


Figure 3.16. (a) Reflection spectra ($\theta = 0^\circ$) of the PVPP-Ir-glass film before cycle #1 and after cycle #50 of localized exposure to water vapor. (b,c) Corresponding photographs (top view) of the PVPP-Ir-glass film (b) before and (c) after 50 cycles of the localized exposure to water vapor at encircled region, respectively. d_3 : 5 nm. Scale bars: 1 cm.

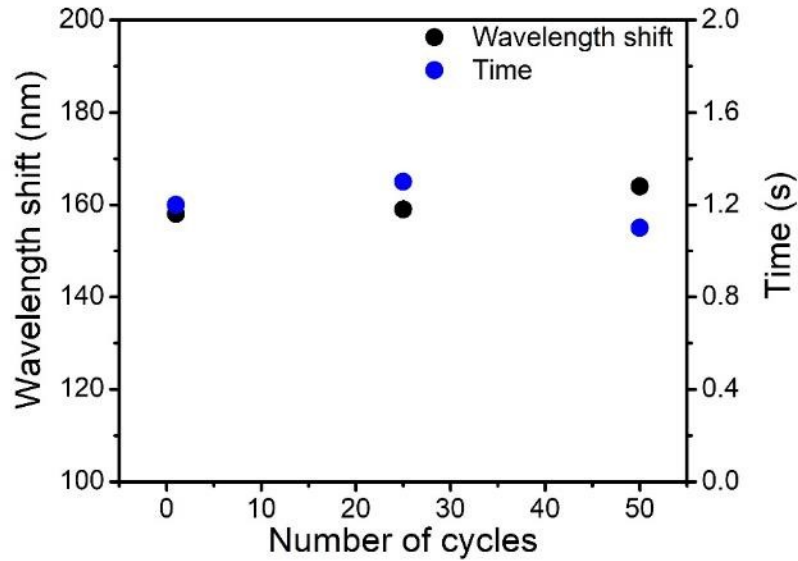


Figure 3.17. Little effects of number of humidity sensing cycles on wavelength shift from blue to red color and corresponding response time of the PVPP-Ir-glass film upon localized exposure to water vapor during cycle #1, 25 and 50.

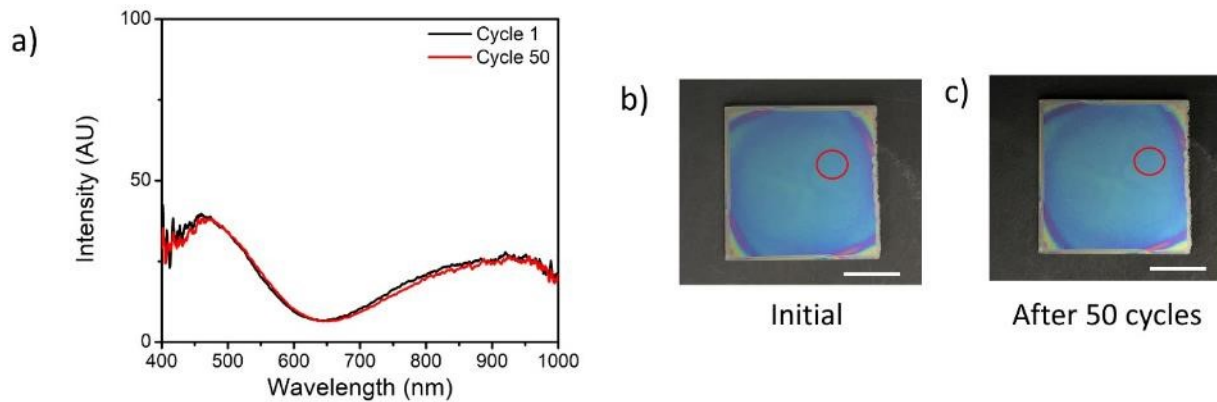


Figure 3.18. (a) Reflection spectra ($\theta = 0^\circ$) of the PVPP-nichrome-glass film before cycle #1 and after cycle #50 of localized exposure to water vapor. (b,c) Corresponding photographs (top view) of the PVPP-Ir-glass film (b) before and (c) after 50 cycles of the localized exposure to water vapor at encircled region, respectively. d_3 : 5 nm. Scale bars: 1 cm.

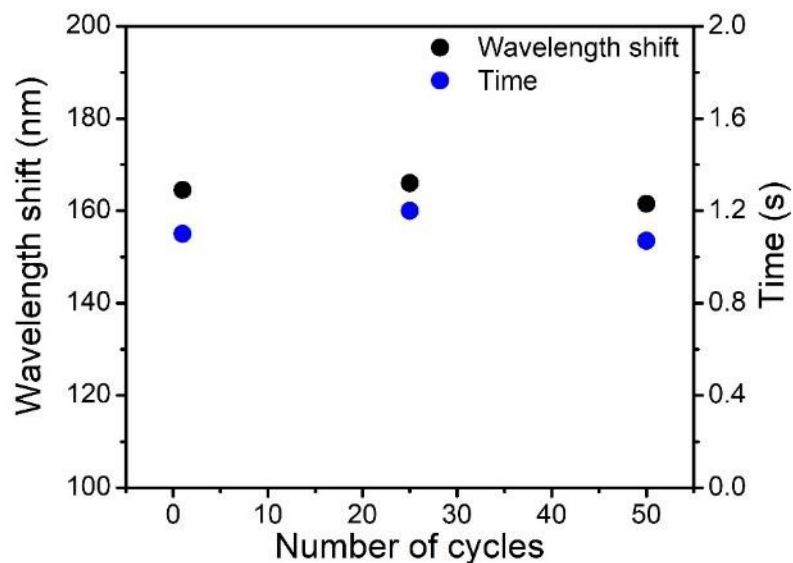


Figure 3.19. Little effects of number of humidity sensing cycles on wavelength shift from blue to red color and corresponding response time of the PVPP-nichrome-glass film upon localized exposure to water vapor during cycle #1, 25 and 50.

3.3.5. Colorimetric Responsive Interference Coloration (RIC) Organic Vapor Sensor.

Although the PDMS-Ir-glass system has no response to the humidity change, it exhibits exceptional sensitivity towards organic vapors such as hexane that can swell PDMS. It takes just ~ 0.23 s for the peak wavelength for the second-order of reflection to undergo ~ 200 nm of shift from the blue-colored to red-colored PDMS film upon exposure to the hexane vapor (Figure 3.20a, 3.21). After the removal of the hexane vapor, it takes merely ~ 0.17 s for the red-colored PDMS film to be fully recovered to the original blue-colored film (Figure 3.20b, Figure 3.22, 3.23). For comparison, both PVP-Ir-glass and PC-Ir-glass systems do not show color change upon exposure to the hexane vapor (Figure 3.24). Therefore, the selectivity of a RIC sensor towards specific

stimulus can be modulated by choosing a polymer material with desirable structure and properties.

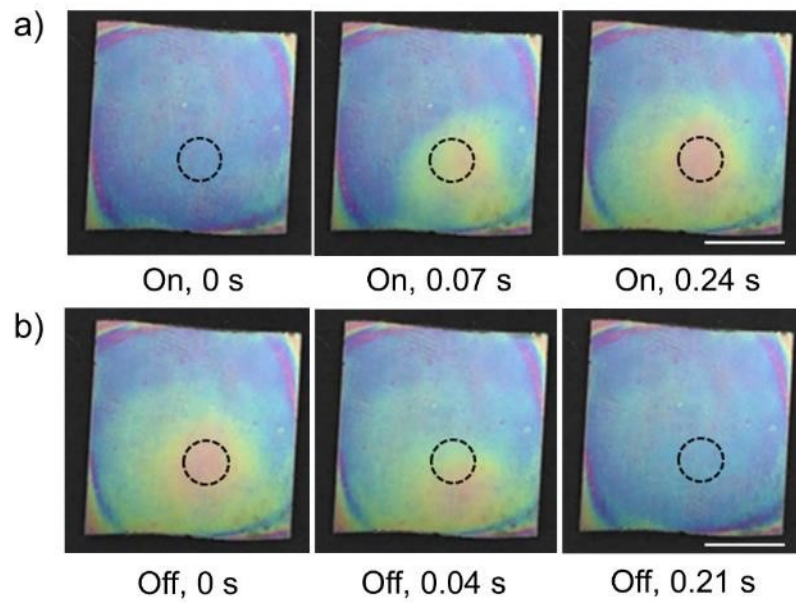


Figure 3.20. a,b) Photographs (top view) of the PDMS-Ir-glass film in (a) response to and (b) recovery from the localized exposure to hexane vapor, respectively. d_3 : 5 nm. Scale bars: 1 cm.

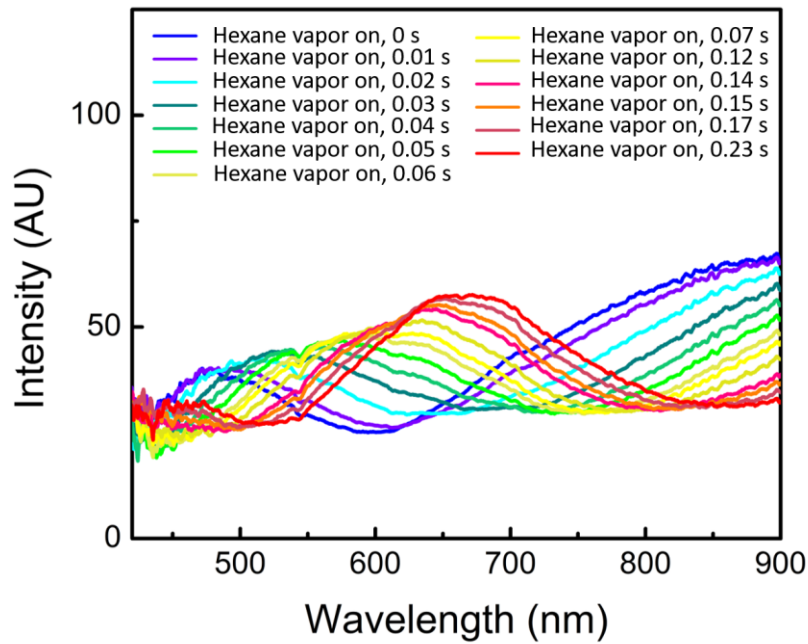


Figure 3.21. Dynamic reflectance spectra ($\theta = 0^\circ$) of the PDMS-Ir-glass film in response to hexane vapor.

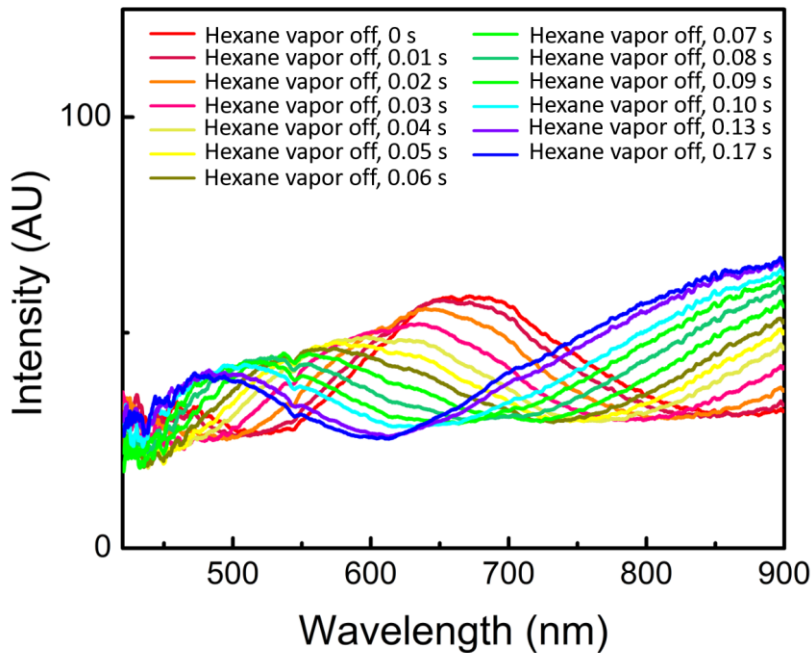


Figure 3.22. Dynamic reflectance spectra ($\theta = 0^\circ$) of the PDMS-Ir-glass film in recovery from hexane vapor.

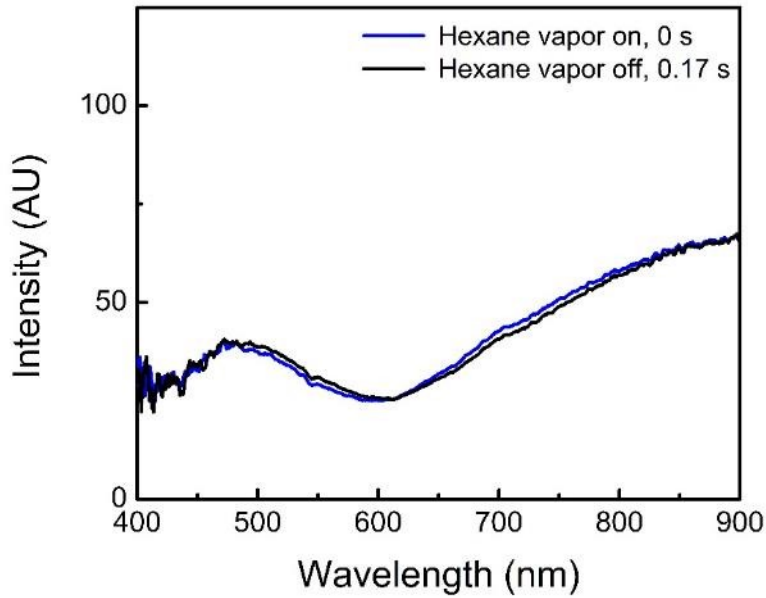


Figure 3.23. Reflection spectra ($\theta = 0^\circ$) of the PDMS-Ir-glass film before and after exposure to hexane vapor.

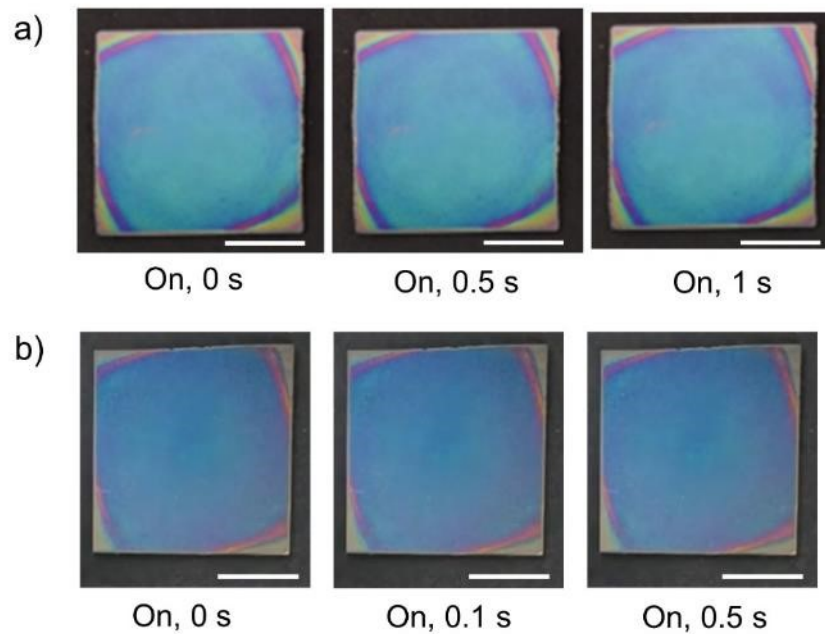


Figure 3.24. a,b) Photographs (top view) of the (a) PVP-Ir-glass, and (b) PC-Ir-glass film showing no response to hexane vapor, respectively. d_3 : 5 nm. Scale bars: 1 cm.

Nafion-based RIC demonstrates response to both humidity and VOCs such as ethanol, hexane, trifluoroacetic acid (TFA) etc. For example, exposing Nafion-Ir-glass to ethanol vapor generated by a humidifier shows a fast and reversible color change with good spacial and temporal resolution. Selectivity of sensors to various classes of VOCs is an important characteristic of a sensor. We found that exposing Nafion-Ir-glass to ammonia and triethylamine (TEA) give two different responses. For example, exposing to ammonia vapor results in a blue shift while exposing to TEA vapor results in a red shift (change from blue to greenish-yellow). Although the exposure of Nafion-Ir-glass to these bases (ammonia and TEA vapor) results in locking of the Nafion which by itself is irreversible, soaking of the base treated Nafion-Ir-glass in 1M HCl followed by rinsing results in the recovery of the initial color of the sensor. This ability of Nafion-based RIC to selectively distinguish between ammonia and amine may be important for design of sensor arrays which can selectively distinguish between closely related VOCs.

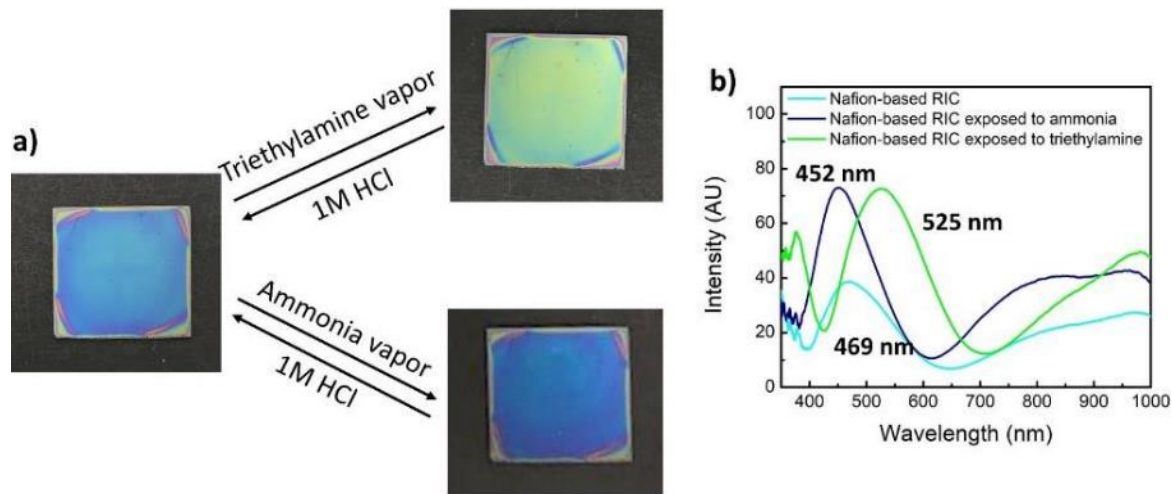


Figure 3.25. a) Photographs (top view) of the Nafion-Ir-glass (~2.5cm square) differentiating showing different response to ammonia and triethylamine vapor. (b) Corresponding reflectance spectra of ammonia and TEA vapor treated samples.

3.3.6. Viewing Angle Dependence of RIC Films

Like other conventional interference films and photonic crystals, our current RIC systems exhibit iridescent reflection colors that depend on the viewing angle (Figure 3.26). Both viewing angle-dependent photography and reflection spectroscopy reveal that the interference coloration has less viewing-angle dependence than expected from theoretical prediction (Equation 3.1). For example, the reflection color remains nearly same when the viewing angle is within 30 degree relative to the normal (Figure 3.26a). Although the origin of difference between experimental and theoretical results is unclear and requires further investigation in the future, the less-than-expected viewing-angle dependence of reflected colors can help to improve the reliability of the RIC sensors and will be beneficial for practical application.

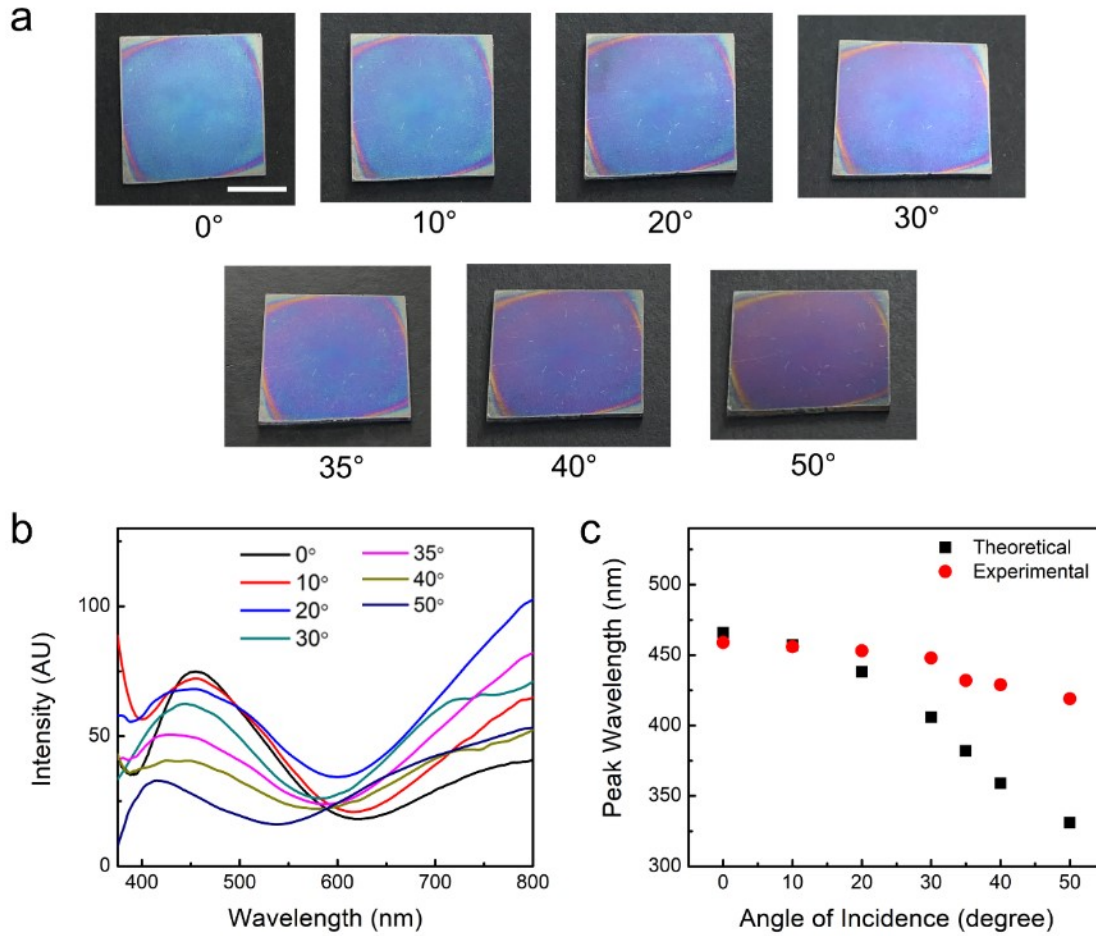


Figure 3.26. a) Viewing-angle dependent photography of the PC-Ir-glass film at different viewing angles relative to the normal. b) Reflection spectroscopy of the PC-Ir-glass film at different angles of incidence (θ). The reflection spectra were obtained using a fiber-guided light source (HL-2000, Ocean Optics) and a detector (USB2000+, Ocean Optics). Both light source and detector were varied at the same angle relative to the normal. c) Comparison of the observed reflection peak positions at various θ values with corresponding predicted reflection peak positions based on Equation 1 in the main text. d_2 : 295 nm. d_3 : 5 nm. Scale bar: 1 cm.

3.3.7. Humidity Sensing Window

Suitable indoor air humidity levels are important for human health and comfort. The EPA recommends the indoor relative humidity stays between 30% and 50%. If the indoor relative humidity is above 60%, it not only makes occupants feel less comfortable, but also allows mold and mildew to grow, which can cause health problems. On the other hand, if the indoor air is too dry with less than 30% relative humidity, it can cause static electricity problems, sensory irritation of the skin, dry eyes, and dry, sore throat. Low-cost, energy-free, real-time, continuous sensors are highly desirable for monitoring and control of temperature, humidity, occupancy, and indoor air quality in smart residential and commercial buildings.^{29,30}

By using a metal layer of 3 nm thickness and transparent substrate, both good transparency and bright interference coloration can be achieved in RIC sensors (Figure 3.27), which open door to new applications such as stimuli-sensing windows. One main advantage of such stimuli-sensing windows is their self-reporting feature that autonomously exhibits a color change upon exposure to a target stimulus without using external power sources. For instance, the PVP-Ir-glass sensor displays spatial and temporal color change in response to the localized humidity change while being transparent all the time (Figure 3.27). Since the constructive interference reflected colors and complementary destructive interference transmitted colors on opposite sides of the transparent humidity-sensing window are strongly coupled (Figure 3.27c-g), this allows monitoring of the indoor humidity level from both inside and outside the building.

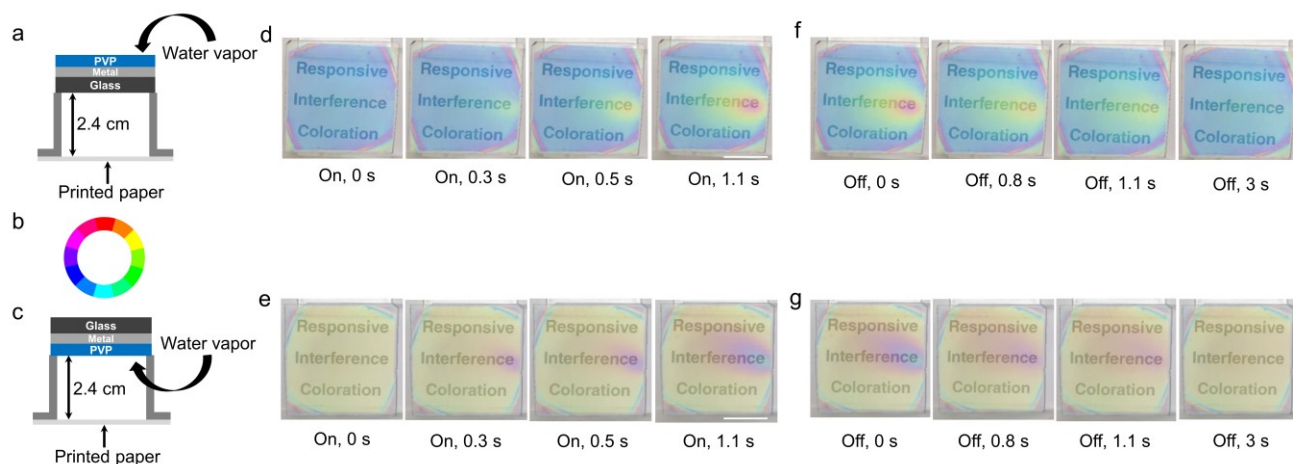


Figure 3.27. Demonstration of a humidity-sensing window made of PVP-Ir-glass. (a,d,f) Top view from the PVP side in (d) response to and (f) recovery from the localized exposure to water vapor, respectively. (b) A traditional color wheel. Each color serves as the complement of the opposite color across the wheel. (c,e,g) Top view from the glass side in (e) response to and (g) recovery from the localized exposure to water vapor, respectively. d_3 : 3 nm. Scale bars: 1 cm.

The outdoor monitoring of the indoor relative humidity enables facile control of the indoor humidity by a third party without compromise of security. Alternatively, the transparent humidity-sensing window with the sensing layer facing outside lets people to determine the outdoor relative humidity level from both indoor and outdoor. The indoor monitoring of the outdoor air humidity helps residents to easily determine when to open windows for fresh air with suitable relative humidity.

Air leaks through windows and doors represent significant amount of commercial and residential building energy consumption. Detecting the leaking locations of a leaky window is crucial for sealing the leaks and saving the energy. The transparent humidity-sensing window with the sensing layer facing inside enables energy-free, real-time

monitoring of potential window leaks with spatial resolution, because the localized air leak can cause the color change at the leaking spot of the window, due to the difference of outdoor and indoor moisture levels. Furthermore, the transparent humidity-sensing window with the sensing layer facing inside or outside can be used for monitoring of the air humidity inside or outside the car, which can help drivers to prevent the car window from fogging up by timely adjustment of humidity and temperature inside the car.

The transparent RIC films also make it possible to develop other stimuli-responsive windows by choosing appropriate sensing polymers. For instance, the volatile organic compounds (VOCs) are common indoor pollutants, which may have short- and long-term adverse health effects. The VOCs-sensing windows can be used for monitoring the indoor air quality from both inside and outside the building. In addition, the alcohol-sensing car window may help prevent drunk driving.

3.4. Conclusions

In summary, we have developed a versatile new strategy that enables scalable and affordable manufacturing of transparent RIC systems. In our polymer-metal-substrate RIC system, the thickness of the polymer layer determines the reflected color, whereas the ultrathin metal layer serves as an optical filter instead of high refractive index substrate or highly reflective substrate, which can tune the degree of transparency, the constructive interference reflection light, and complementary destructive interference transmission light via changing the metal layer thickness. We have demonstrated real-time, continuous, colorimetric RIC sensors for humidity and organic vapor, and temperature by using various stimuli-responsive polymers. The main advantages of such RIC sensors include low cost, zero power consumption, spatial and

temporal resolution, fast, dynamic, and reversible response. The selectivity of a RIC sensor towards specific stimulus can be modulated by choosing a polymer material with desirable structure and properties. Using a clear substrate (e.g. glass) allows for strong coupling of reflected colors and complementary transmitted colors on opposite sides of the transparent RIC film, which leads to new potential applications such as the self-reporting, humidity-sensing window. Although the current work is focused on rigid transparent glass, our RIC design is applicable to many other substrates such as PDMS. PDMS-based transparent RIC films with coupled complementary colors on opposite sides are desirable for applications such as wearable sensors, where the color change at the on-body side can be transduced into the color change on the opposite side of the film. In addition, such flexible RIC films can integrate sensing with actuation, which opens door to new applications. Since a vast number of stimuli-responsive polymers and composites are available,²³ it is possible to significantly expand the RIC systems with new properties and functions, which will open door to many application possibilities.

3.5. References

- (1) Kinoshita, S.; Yoshioka, S.; Miyazaki, J. Physics of Structural Colors. *Rep. Prog. Phys.* **2008**, *71*, 076401.
- (2) Sun, J.; Bhushan, B.; Tonga, J. Structural Coloration in Nature. *RSC Adv.* **2013**, *3*, 14862-14889.
- (3) Ge, J.; Yin, Y. Responsive Photonic Crystals. *Angew. Chem. Int. Ed.* **2011**, *50*, 1492-1522.

- (4) Zhao, Y.; Xie, Z.; Gu, H.; Zhu, C.; Gu, Z. Bio-Inspired Variable Structural Color Materials. *Chem. Soc. Rev.* **2012**, *41*, 3297-3317.
- (5) Chan, E. P.; Walsh, J. J.; Urbas, A. M.; Thomas, E. L. Mechanochromic Photonic Gels. *Adv. Mater.* **2013**, *25*, 3934-3947.
- (6) Fenzl, C.; Hirsch, T.; Wolfbeis, O. S. Photonic Crystals for Chemical Sensing and Biosensing. *Angew. Chem. Int. Ed.* **2014**, *53*, 3318-3335.
- (7) Cai, Z.; Smith, N. L.; Zhang, J. -T.; Asher, S. A. Two-Dimensional Photonic Crystal Chemical and Biomolecular Sensors. *Anal. Chem.* **2015**, *87*, 5013-5025.
- (8) Phillips, K. R.; England, G. T.; Sunny, S.; Shirman, E.; Shirman, T.; Vogel, N.; Aizenberg, J. A Colloidoscope of Colloid-Based Porous Materials and Their Uses. *Chem. Soc. Rev.* **2016**, *45*, 281-322.
- (9) Dumanli, A. G.; Savin, T. Recent Advances in the Biomimicry of Structural Colours. *Chem. Soc. Rev.* **2016**, *45*, 6698-6724.
- (10) Inan, H.; Poyraz, M.; Inci, F.; Lifson, M. A.; Baday, M.; Cunningham, B. T.; Demirci, U. Photonic Crystals: Emerging Biosensors and Their Promise for Point-of-Care Applications. *Chem. Soc. Rev.* **2017**, *46*, 366-388.
- (11) Goerlitzer, E. S. A.; Klupp Taylor, R. N.; Vogel, N. Bioinspired Photonic Pigments from Colloidal Self-Assembly. *Adv. Mater.* **2018**, *30*, 1706654.
- (12) Isapour, G.; Lattuada, M. Bioinspired Stimuli-Responsive Color-Changing Systems. *Adv. Mater.* **2018**, *30*, 1707069.
- (13) Kats, M. A.; Capasso, F. Optical Absorbers Based on Strong Interference in Ultra-Thin Films. *Laser Photonics Rev.* **2016**, *10*, 735-749.

- (14) Kramer, R. M.; Crookes-Goodson, W. J.; Naik, R. R. The Self-Organizing Properties of Squid Reflectin Protein. *Nat. Mater.* **2007**, *6*, 533-538.
- (15) Phan, L.; Walkup IV, W. G.; Ordinario, D. D.; Karshalev, E.; Jocson, J. -M.; Burke, A. M.; Gorodetsky, A. A. Reconfigurable Infrared Camouflage Coatings from a Cephalopod Protein. *Adv. Mater.* **2013**, *25*, 5621-5625.
- (16) Yu, L.; Xu, H.; Monro, T. M.; Lancaster, D. G.; Xie, Y.; Zeng, H.; Chen, G. Y.; Liu, X. Ultrafast Colorimetric Humidity-Sensitive Polyelectrolyte Coating for Touchless Control. *Mater. Horiz.* **2017**, *4*, 72-82.
- (17) Qin, M.; Sun, M.; Bai, R.; Mao, Y.; Qian, X.; Sikka, D.; Zhao, Y.; Qi, H. J.; Suo, Z.; He, X. Bioinspired Hydrogel Interferometer for Adaptive Coloration and Chemical Sensing. *Adv. Mater.* **2018**, *30*, 1800468.
- (18) Steele, J. J.; Taschuk, M. T.; Brett, M. J. Nanostructured Metal Oxide Thin Films for Humidity Sensors. *IEEE Sens. J.* **2008**, *8*, 1422-1428.
- (19) Hawkeye, M. M.; Brett, M. J. Optimized Colorimetric Photonic-Crystal Humidity Sensor Fabricated Using Glancing Angle Deposition. *Adv. Funct. Mater.* **2011**, *21*, 3652-3658.
- (20) Greenspan, L. Humidity Fixed Points of Binary Saturated Aqueous Solutions. *J. Res. Natl. Bur. Stand. Sec. A* **1977**, *81A*, 89-96.
- (21) Banisadr, S., Oyefusi, A., and Chen, J. A Versatile Strategy for Transparent Stimuli-Responsive Interference Coloration. *ACS applied materials & interfaces*, **2019**, *11*, 7415-7422.
- (22) Cohen Stuart, M. A.; Huck, W. T. S.; Genzer, J.; Müller, M.; Ober, C.; Stamm, M.; Sukhorukov, G. B.; Szleifer, I.; Tsukruk, V. V.; Urban, M.; Winnik, F.; Zauscher, S.;

Luzinov, I.; Minko, S. Emerging Applications of Stimuli-Responsive Polymer Materials. *Nat. Mater.* **2010**, *9*, 101-113.

(23) Chen, Z.; Lu, C. Humidity Sensors: A Review of Materials and Mechanisms. *Sensor Lett.* **2005**, *3*, 274-295.

(24) Telford, A. M.; James, M.; Meagher, L.; Neto, C. Thermally Cross-Linked PNVP Films as Antifouling Coatings for Biomedical Applications. *ACS Appl. Mater. Interfaces* **2010**, *8*, 2399-2408.

(25) Zhang, W.; Webb, D. J. Humidity responsivity of poly (methyl methacrylate)-based optical fiber Bragg grating sensors. *Opt. Lett.* **2014**, *39*, 3026.

(26) Vogt, B. D.; Soles, C. L.; Lee, H.; Lin, E. K.; Wu, W. Moisture absorption into ultrathin hydrophilic polymer films on different substrate surfaces *Polymer* **2005**, *46*, 1635.

(27) Prudic, A.; Ji, Y.; Luebbert, C.; Sadowski, G. Influence of humidity on the phase behavior of API/polymer formulations *Eur. J. Pharm. Biopharm.* **2015**, *94*, 352.

(28) Stellrecht, E.; Han, B.; Pecht, M. Measurement of the hygroscopic swelling coefficient in mold compounds using moiré interferometry. *Exp. Techniques* **2003**, *27*, 40.

(29) Wolkoff, P. Indoor Air humidity, Air Quality, and Health-An Overview. *Int. J. Hyg. Environ. Health.* **2018**, *221*, 376-390.

(30) Neal Stewart Jr., C.; Abudayyeh, R. K.; Stewart, S. G. Houseplants as Home Health Monitors. *Science* **2018**, *361*, 229-230.

Chapter 4: Self-Reporting and Self-Acting Chemical Sensing without Power

4.1. Introduction

The Internet of Things (IoT) is a network of broadly defined devices that are used to collect, exchange, and process information, which enables a wide range of transformative applications, such as environmental monitoring, smart home, wearable health-monitoring electronics, and smart farming. One of the critical challenges that significantly limits the implementation and growth of the IoT is exponentially growing power demand by the vast network of electronic devices.¹⁻⁴ For instance, state-of-the-art sensors use electronics to actively monitor the environment for the infrequent target stimulus, consuming power continuously while waiting for the specific signal.^[5] Such active electronic sensors not only have high energy footprints, but also have limited sensor lifetime because sensors are always in the working state. Therefore, developing energy efficient sensors are essential to fully realize the potential of the IoT.

One approach is to use photovoltaics to harvest solar energy to power the sensors.^[1] Such self-powered sensors can be used as wearable sensors for the precise and continuous monitoring of biological signals.^{6,7} Another approach is to use triboelectric nanogenerators to harvest mechanical energy from the environment to power the sensors.⁸ Since both solar and environmental mechanical energy sources are intermittent by nature and they are not always available for conversion into electricity, energy storage devices such as batteries are generally required to ensure the sensor performance.

Colorimetric chemical sensors convert a chemical input signal into an optical output signal.⁹⁻¹¹ One main advantage of colorimetric sensors is their self-reporting feature that autonomously exhibits a color change upon exposure to a target stimulus without using external power sources, which make them.

To significantly lower the power-consumption of environmental monitoring sensor networks, it is crucial to develop a new type of sensors that not only is capable of continuous and passive monitoring of the environment without power consumption, but also can trigger autonomous reporting and acting functions when an event of interest is detected and confirmed.⁵ Qian and coworkers have recently developed a power-free thermally activated micromechanical sensor that produces an electrical readout signal only when irradiated by a narrowband mid-infrared light.^{12,13} Herein, we report a general strategy for powerless self-reporting and self-acting chemical sensors (Figure 4.1), which can differentiate multiple different chemical stimuli by transforming one chemical stimulus into one type of self-reporting output signal (i.e. color change), whereas transducing another chemical stimulus into two different types of self-reporting output signals (i.e. color change + bending). The bending actuation could be used as the self-acting function such as waking an electric circuit of an alarm system upon the detection of a specific stimulus.

4.2. Materials and Methods

4.2.1. Materials.

Polyvinylpyrrolidone (PVP) powder was purchased from Alfa Aesar. Polydimethylsiloxane (PDMS) precursors (Sylgard 184) were purchased from Dow Corning, and mixed based on the

manufacturer's recommended base to crosslinker ratio of 10:1. PVP solutions in ethanol with PVP loadings from 6 to 9 wt% were prepared and stored at room temperature. Ethanol (200 proof) was purchased from Koptec. Pentane was acquired from Sigma-Aldrich.

4.2.2. Preparation of Metal Layer.

Ultrathin film of iridium is deposited on a desired substrate in a sputter coating system (model K150X, Quorum Emitech) using a high purity iridium target (Ted Pella, Inc.) under a vacuum pressure of 2×10^{-3} mbar.

4.2.3. Preparation of PVP-Ir-PDMS Films.

The PDMS substrates were made by mixing and curing the PDMS precursors at 70 °C overnight or 100 °C for about 3 h. The fully-cured PDMS film was then cut into small pieces ($\sim 2 \text{ cm} \times 2 \text{ cm}$), followed by ultrathin metal layer coating. Subsequently, $\sim 0.4 \text{ mL}$ of the PVP solution was placed on the metal-coated PDMS substrate, and then spin-coated at a specific spinning rate for 30 seconds. Since the reflected color is controlled by the polymer layer thickness, appropriate spinning rate and concentration of the PVP solution were used to obtain the desired color.

4.2.4. Sample Characterizations.

The reflection spectra were acquired using a fiber optic spectrometer (USB2000+, Ocean Optics). The incident light was perpendicular to the plane of the film. The transmission spectra of the samples were recorded with a Cary 5000 UV-Vis-NIR spectrophotometer. Unless otherwise stated, all sample characterization was carried out at ambient humidity ($45 \pm 5 \text{ RH}\%$) and room temperature ($22 \pm 2 \text{ }^\circ\text{C}$).

4.2.5. Stimuli Response Measurements.

The chemical vapors (i.e. water and pentane vapors) for sensing experiments were generated by a commercial ultrasonic humidifier (Essential Oil Diffuser, Radha Beauty Co.), and then applied to the samples through a rubber tubing with a small plastic tip (e.g. pipette tip) at the end. The dynamic reflection spectra for the response of PVP-Ir-PDMS films to water vapor were acquired continuously using a fiber optic spectrometer (USB2000+, Ocean Optics) with the interval time of 10 ms.

4.3. Results and Discussion

Today more than half of the energy used by a processor is to move data via interconnects, e.g., between memory and logic.⁴ Reducing the “energy cost” of data management in IoT applications has become increasingly important. The chemical sensor described in this work can distinguish two different chemical signals and act differently. Such chemical sensors with on-site “intelligence” that allows decisions and actuation to be handled locally will reduce data movement and the energy needed to manage otherwise higher volume of data in IoT applications.

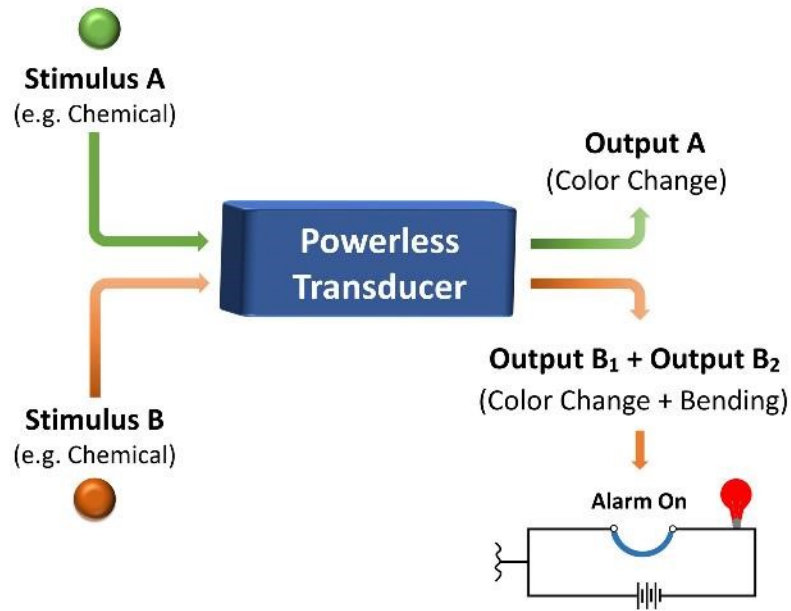


Figure 4.1. Schematic illustration of self-reporting and self-acting chemical sensor.

Our thin-film powerless transducer is composed of three layers: 1) The thin polymer layer acts as the first sensing layer, which exhibits stimuli-responsive thin film interference coloration; 2) The ultrathin metal layer serves as an optical filter; 3) The flexible substrate layer acts as the second sensing layer, which is responsive to different chemical stimuli. Our simple yet versatile trilayer thin-film transducer system allows the powerless integration of sensing with actuation, and it is applicable to a wide range of stimuli-responsive thermoplastics, thermosets, and polymer composites.¹⁵

The bioinspired stimuli-responsive structural coloration has received great interest in the past two decades due to its wide range of promising applications.¹⁵⁻²⁴ Thin-film interference is the simplest structural coloration mechanism, which is responsible for the colorful, iridescent reflections that can be seen in oil films on water, and soap bubbles.^{16,17,26-29} Thanks to its design simplicity, which does not require multilayers of

materials with alternative refractive indices or micro- and nanostructures, thin film interference represents a promising solution towards scalable and affordable manufacturing of high-quality responsive structural coloration systems. However, thin films of polymers with appropriate thickness generally do not exhibit visible structural colors if they are directly deposited on low-cost substrates such as glass³⁰ and polydimethylsiloxane (PDMS). We have found recently that, in order to see bright thin-film interference color on glass, it is crucial to use an ultrathin metal layer as an optical filter instead of high refractive index substrate or highly reflective substrate.³⁰ Such an optical filter layer can significantly enhance the observed interference color intensity by simultaneously optimizing both the constructive interference reflection light and complementary destructive interference transmission light. In this work, the ultra thin metal layer is also found to be key to observe bright thin film interference colors on flexible PDMS substrate (Figure 4.2).

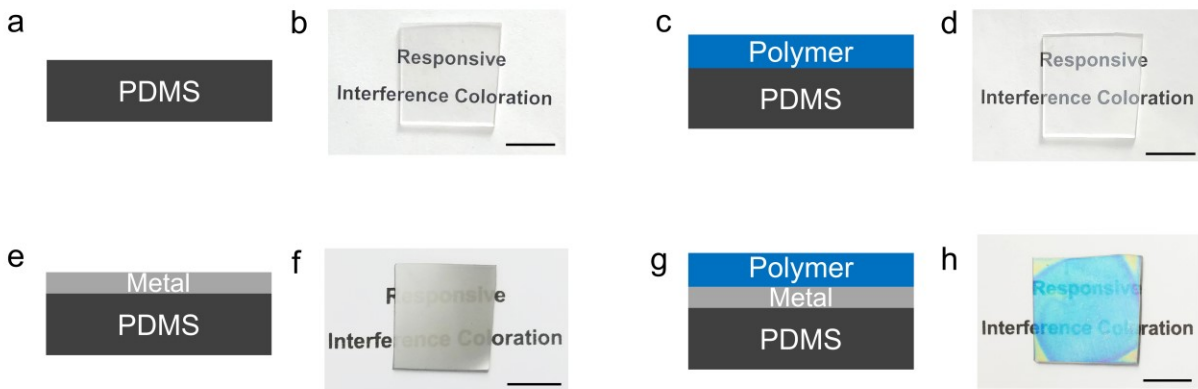


Figure 4.2. a,b) The colorless PDMS substrate. c,d) The colorless PVP-PDMS film with the PVP layer thickness comparable to that in (g,h). e,f) The Ir-PDMS film showing light grayish color. g,h) The PVP-Ir-PDMS film showing bright blue color. d_3 : (f,h) 5 nm. Scale bars: 1 cm

Our previous study was focused on the sensing properties of the glass-based thin film interference films.³⁰ Since the glass substrate is rigid and not responsive to external stimuli by itself, the actuation is impossible in these glass-based films. In current study, we have been successful for the first time in powerless integration of sensing with actuation functions in thin film interference films by using the flexible PDMS substrate, which also acts as the second sensing layer (Figure 4.3a).

The condition for constructive thin-film interference is determined by Equation 4.1:

$$m\lambda = 2n_2d_2\cos\theta \quad (4.1)$$

where λ is the wavelength giving the maximum reflectivity, m is the order of diffraction (a positive integer), d_2 and n_2 are the thickness and refractive index of the polymer layer, respectively, and θ is the angle of incidence.^{16,17} The condition for the destructive thin-film interference follows Equation 4.1:

$$(m-1/2)\lambda = 2n_2d_2\cos\theta \quad (4.2)$$

where λ represents the wavelength giving the minimum reflectivity (maximum transmissivity).^{16,17} In this work, the polyvinylpyrrolidone (PVP) is chosen as the first sensing layer, whereas the PDMS is selected as the flexible substrate as well as the second sensing layer (Figure 4.2, 4.3). By tuning the PVP polymer layer thickness via spin coating using appropriate spin speeds and concentrations of polymer solutions, various interference colors including purple, blue, green, yellow, and red can be generated on metal-coated PDMS substrates. Owing to the transparency of PDMS, both constructive interference reflected colors and complementary destructive interference transmitted colors across the spectrum can be created simultaneously on opposite sides of the substrate, respectively. Like other conventional interference films and photonic

crystals, our stimuli-responsive interference coloration films exhibit iridescent reflection colors that depend on the viewing angle.

PVP and PDMS show opposite stimuli-responsive properties because of their different chemical structures. The PVP layer is responsive to water vapor, but not volatile organic compounds (VOCs) such as pentane vapor. In contrast, the PDMS substrate is responsive to VOCs such as pentane vapor, but not water vapor. Upon exposure to the water vapor in area C, the PVP-Ir-PDMS film only exhibits a localized color change from blue to yellow and red without bending (Figure 4.3e). The reflectance peak position ($\theta = 0^\circ$) of area C undergoes significant red-shift of ~ 130 nm (Figure 4.3h), which suggests the color change in area C is due to the PVP layer thickness increase upon exposure to the water vapor. Since the PVP layer is much thinner than the PDMS substrate (Thickness: ~ 300 μm), the swelling of the PVP layer does not cause the bending of the PVP-Ir-PDMS film. After the removal of the water vapor, the area C of the PVP-Ir-PDMS film is fully recovered to the original blue color.

In contrast, when exposed to a pentane vapor, the PDMS layer swells and leads to the bending of the PVP-Ir-PDMS film towards the PVP side (Figure 4.3c,d). The pentane vapor-induced bending actuation also causes a simultaneous color change from blue to dark purple at both ends of the film. The bending is fully reversible after the removal of the pentane vapor. Since the reflectance peak position ($\theta = 0^\circ$) of both area A and area B remain essentially unchanged around 473 nm upon bending (Figure 4.3f-g), the color change observed in area B can be attributed mainly to the change of viewing angle. The bending actuation of the film could be employed as an electrically conductive mechanical switch to turn on the electric circuit for further actions (e.g. alarm).

There are different ways to tune the curvature of the PVP-Ir-PDMS film. For example, using thinner PDMS as the sensing layer for pentane vapor may help increase curvature even at low concentration of pentane vapor. On the otherhand, the curvature may be increased with increase in concentration of pentane vapor as more swelling can be achieved by the PDMS layer

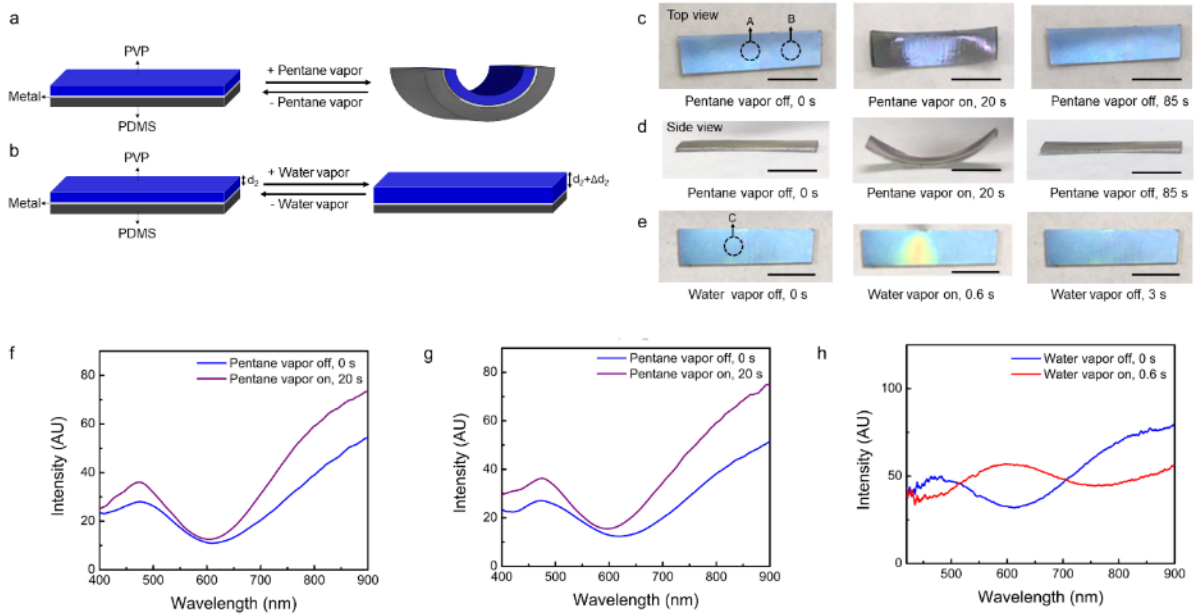


Figure 4.3. Self-reporting and self-acting sensor. a,b) Sensing mechanisms for (a) pentane vapor and (b) water vapor, respectively. c,d) Photographs of (c) top view and (d) side view of pentane vapor-induced bending deformation of the PVP-Ir-PDMS film. e) Photographs (top view) of the PVP-Ir-PDMS film in response to and recovery from the localized exposure to water vapor, respectively. f,g) Reflection spectra ($\theta = 0^\circ$) of the encircled area (f) A and (g) B of the PVP-Ir-PDMS film in Figure 4c before and upon exposure to pentane vapor, respectively. To acquire the reflection spectra ($\theta = 0^\circ$) of the encircled area B, the fiber optic probe is oriented perpendicular to the plane of the area B of the film for both unbent and bent shapes. h) Reflection spectra ($\theta = 0^\circ$) of the encircled area C of the PVP-Ir-PDMS film in Figure 4e before and upon exposure to water vapor. d_3 : 5 nm. Scale bars: 5 mm.

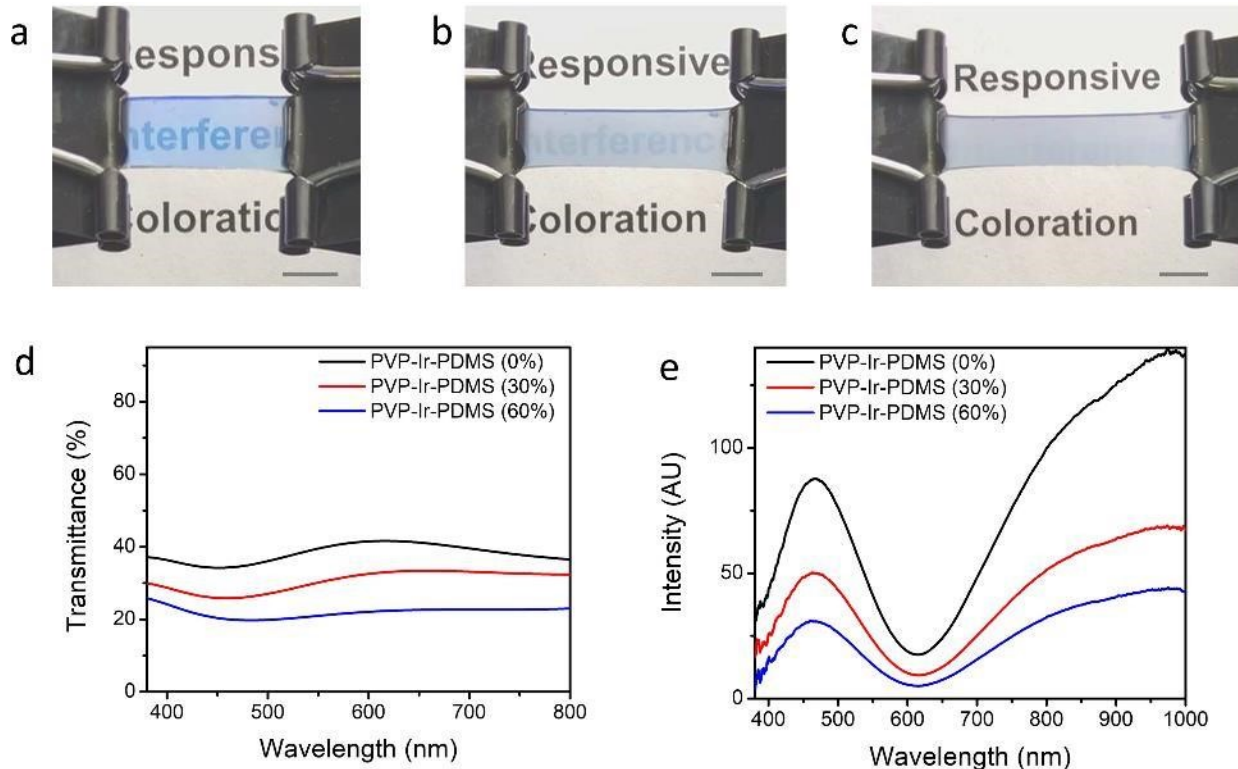


Figure 4.4. Strain induced transparency. a-b) Photograph of PVP-Ir-PDMS at different stretching ratio in a) 0, b) 30 and c) 60% elongation, respectively. d) Transmission spectra of PVP-Ir-PDMS at different elongation. e) Reflection spectra ($\theta = 0^\circ$) of the PVP-Ir-PDMS film at elongation ratio. d_3 : 5 nm. Scale bars: 5 mm.

Cephalopods, such as cuttlefish are able to instantaneously change their skin color pattern for camouflage and communication.³¹ This transformation is made possible by the motion of a chromatophore, in which the sac contains pigments with radial muscles attached peripherally. Additionally, cuttlefish has the capability of tuning it's optical properties by altering the surface structures and morphologies of their muscles through mechanical means.³¹ Inspired by this display strategy by mechanical means found in nature, we demonstrated stretching deformation-controlled surface engineering to achieve tunable transparency in a PVP-Ir-PDMS film (Figure 4.4). Upon

in-plane stretching of the film, the PVP-Ir-PDMS shows a reversible change in transparency from being transparent to completely opaque after elongation by 60% (Figure 4.4a-c). The correlation between the transmittance and elongation shows a decrease in transmittance with increasing elongation of the film (Figure 4.4d) which is in line with observed opacity observe in Figure 4.4a-c. The reflectance spectra show no significant blue shift in peak position but decrease in intensity and broader peak as the PVP-Ir-PDMS film is stretched to 60%. This tunable transparency via transmission and reflectance may find application smart window and optical switches.

The opacity of the stretched state can be attributed to strong trapping and scattering of light resulting from the strain-dependent secondary cracks and possibly folds in the iridium and PDMS, respectively. Zeng and coworkers demonstrated a deformation-controlled surface engineering to achieve various mechanochromisms, through a series of optical device design, by using a hybrid bilayer material system consisting of a rigid thin film bonded on a soft substrate. Using strain-dependent cracks and folds, they demonstrated tunable and reversible transparency change mechanochromism. To investigate the possible cause of opacity in our system, we performed the SEM image of the Ir-PDMS in the pristine, unstretched state (Figure 4.5a). We observed some cracks present on the surface of the Ir-PDMS (Figure 4.5b) probably originating during the fabrication process. Upon stretching and releasing, new cracks (secondary cracks) are formed with majority perpendicular to the stretching direction (Figure 4.5c). We propose that these secondary cracks coupled and/or folds in the Ir-PDMS system causes scattering and/or trapping of light in the stretched state of the PVP-Ir-PDMS. Hence, the observed change in transparency with increased

elongation. Further experiments are needed to further verify the mechanism. For example, it is important to know how the transmittance changes in control samples of Ir-PDMS and pure PDMS film. This will help further verify the proposed mechanism of trapping and scattering of light resulting from the strain-dependent secondary cracks and possibly folds in the iridium and PDMS.

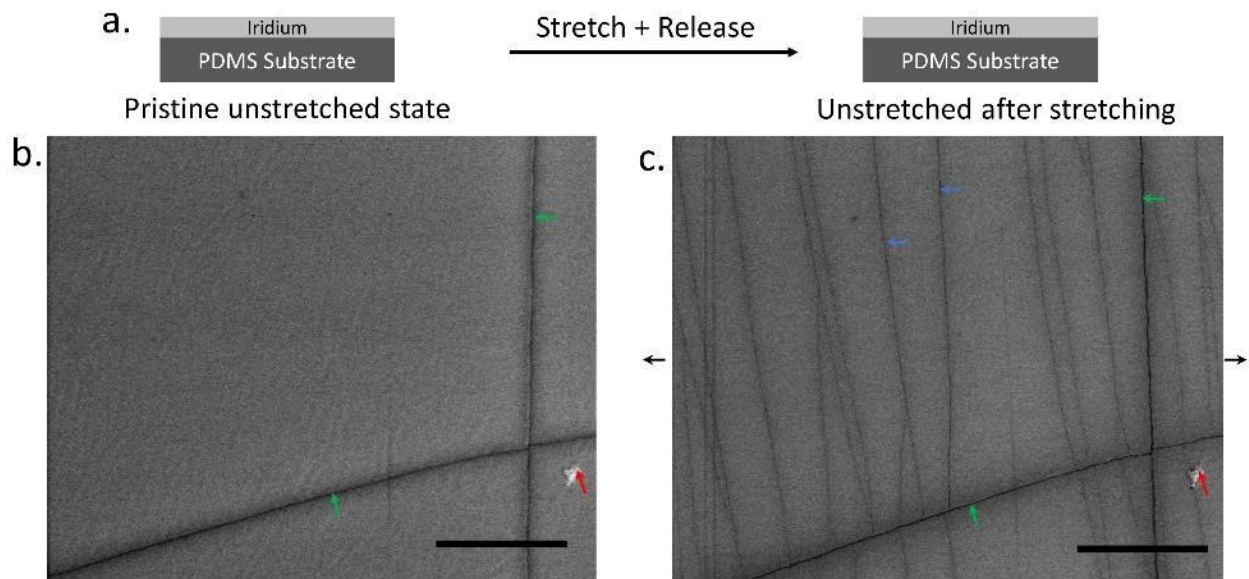


Figure 4.5. a) Scheme of process pristine unstretched and unstretched state after stretching. b) SEM image of unstretched Ir-PDMS, c) SEM image of unstretched Ir-PDMS after stretching. Red arrows show same position. Black arrows represent the stretching direction. Green and blue arrows indicate cracks present before stretching and newly formed cracks after stretching, respectively. Scale bar: 25 μm .

4.4. Conclusion

In summary, we have developed a general strategy for powerless self-reporting and self-acting chemical sensors, which is applicable to a broad range of stimuli-responsive polymer materials.¹⁵ Our simple yet versatile trilayer thin-film transducer system enables integration of sensing with actuation, and tunable transparency which allows on-site

management of intelligent response and action towards different chemical mechanical stimuli. Such new type of chemical sensors not only can remain dormant but always alert while monitoring of the environment without consuming power, but also can initiate autonomous reporting and acting functions when a chemical signal of interest is detected.

4.4. References

- [1] R. Haight, W. Haensch, D. Friedman, *Science* **2016**, 353, 124-125.
- [2] M. S. Reisch, *Chem. Eng. News* **2017**, 95, 16-17.
- [3] A. Raj, D. Steingart, *J. Electrochem. Soc.* **2018**, 165, B3130-B3136.
- [4] <https://www.semiconductors.org/wp-content/uploads/2018/06/RITR-WEB-version-FINAL.pdf>.
- [5] <https://www.darpa.mil/program/near-zero-rf-and-sensor-operations>.
- [6] S. Park, S. W. Heo, W. Lee, D. Inoue, Z. Jiang, K. Yu, H. Jinno, D. Hashizume, M. Sekino, T. Yokota, K. Fukuda, K. Tajima, T. Someya, *Nature* **2018**, 561, 516-521.
- [7] S. Zhang, F. Cicoira, *Nature* **2018**, 561, 466-467.
- [8] C. Wu, A. C. Wang, W. Ding, H. Guo, Z. L. Wang, *Adv. Energy Mater.* DOI 10.1002/aenm.201802906.
- [9] N. A. Rakow, K. S. Suslick, *Nature* **2000**, 406, 710-713.
- [10] I. Lundström, *Nature* **2000**, 406, 682-683.
- [11] J. R. Askim, M. Mahmoudi, K. S. Suslick, *Chem. Soc. Rev.* **2013**, 42, 8649-8682.
- [12] Z. Qian, S. Kang, V. Rajaram, C. Cassella, N. E. McGruer, M. Rinaldi, *Nat. Nanotech.* **2017**, 12, 969-973.
- [13] V. A. Aksyuk, *Nat. Nanotech.* **2017**, 12, 939-940.
- [14] Y. Li, J. Gong, G. He, Y. Deng, *Mater. Chem. Phys.*, **2012**, 134, 1172-1178.

- [15] M. A. Cohen Stuart, W. T. S. Huck, J. Genzer, M. Müller, C. Ober, M. Stamm, G. B. Sukhorukov, I. Szleifer, V. V. Tsukruk, M. Urban, F. Winnik, S. Zauscher, I. Luzinov, Sergiy Minko, *Nat. Mater.* **2010**, *9*, 101-113.
- [16] S. Kinoshita, S. Yoshioka, J. Miyazaki, *Rep. Prog. Phys.* **2008**, *71*, 076401.
- [17] J. Sun, B. Bhushan, J. Tonga, *RSC Adv.* **2013**, *3*, 14862-14889.
- [18] C. Fenzl, T. Hirsch, O. S. Wolfbeis, *Angew. Chem. Int. Ed.* **2014**, *53*, 3318-3335; *Angew. Chem.* **2014**, *126*, 3384-3402.
- [19] J. Ge, Y. Yin, *Angew. Chem. Int. Ed.* **2011**, *50*, 1492-1522; *Angew. Chem.* **2011**, *123*, 1530-1561.
- [20] Y. Zhao, Z. Xie, H. Gu, C. Zhu, Z. Gu, *Chem. Soc. Rev.* **2012**, *41*, 3297-3317.
- [21] E. P. Chan, J. J. Walish, A. M. Urbas, E. L. Thomas, *Adv. Mater.* **2013**, *25*, 3934-3947.
- [22] Z. Cai, N. L. Smith, J. -T. Zhang, S. A. Asher, *Anal. Chem.* **2015**, *87*, 5013-5025.
- [23] K. R. Phillips, G. T. England, S. Sunny, E. Shirman, T. Shirman, N. Vogel, J. Aizenberg, *Chem. Soc. Rev.* **2016**, *45*, 281-322.
- [24] A. G. Dumanli, T. Savin, *Chem. Soc. Rev.* **2016**, *45*, 6698-6724.
- [25] G. Isapour, M. Lattuada, *Adv. Mater.* **2018**, *30*, 1707069.
- [26] M. A. Kats, F. Capasso, *Laser Photonics Rev.* **2016**, *10*, 735-749.
- [27] R. M. Kramer, W. J. Crookes-Goodson, R. R. Naik, *Nat. Mater.* **2007**, *6*, 533-538.
- [28] L. Phan, W. G. Walkup IV, D. D. Ordinario, E. Karshalev, J. -M. Jocsón, A. M. Burke, A. A. Gorodetsky, *Adv. Mater.* **2013**, *25*, 5621-5625.
- [29] M. Qin, M. Sun, R. Bai, Y. Mao, X. Qian, D. Sikka, Y. Zhao, H. J. Qi, Z. Suo, X. He, *Adv. Mater.* **2018**, *30*, 1800468.

[30] Banisadr, S., Oyefusi, A., and Chen, J. *ACS applied materials & interfaces*, **2019**, 11, 7415-7422.

[31] Zeng, S., Zhang, D., Huang, W., Wang, Z., Freire, S.G., Yu, X., Smith, A.T., Huang, E.Y., Nguon, H. and Sun, L., *Nat. Commun.*, 2016, 7, 11802.

Adebola Olatunji Oyefusi

Education

Ph.D., Chemistry

University of Wisconsin-Milwaukee, Milwaukee, WI, USA

September 2013-May 2019

Advisor: Prof. Jian Chen

Dissertation: Smart Polymer System for 3D Shaping and Sensing

M.Sc., Chemistry

Prairie View A&M University, Prairie View, TX, USA

August 2011-December 2012

B.Sc., Industrial Chemistry

University of Lagos, Nigeria

January 2004-December 2009

Research Experience

Graduate Research Assistant, University of Wisconsin-Milwaukee, Milwaukee, WI
January 2013-May 2018

- Developed reprogrammable chemical 3D shaping strategy for origami and kirigami based on Nafion reconfigurable polymer
- Developed macro-, micro- and multilength scale 3D shaping of polymer using 2D printing technology
- Performed macro-, and microscale patterning of polymers using EFD robot/dispenser, soft lithography and photolithography
- Formulated, tested/characterized various direct writing ink solution for 2D printing and 3D shaping
- Designed and fabricated microfluidic channel
- Fabricated and characterized humidity and volatile organic chemical (VOC) sensors based on rigid and flexible substrates
- Imaging techniques: SEM, Polarized optical microscopy
- Spectroscopy techniques: FTIR, ATR, NMR, UV-Visible-NIR, Raman spectroscopy
- Analytical techniques: TGA, DSC, DMA, Tensile test, EDX, XRD, XRF, Two/four-point probe resistivity measurements
- Thin film fabrication techniques: Spin coating, Sputter coating, Spray coating, Solution casting, Thermal vacuum deposition
- Skilled in Simulations (ANSYS), Data Analysis (Origin), 3D-Modeling (SketchUp), Microsoft office (Word, Excel, PowerPoint), Graphics (Adobe Photoshop)

- Performed annual safety inspections, oversaw the chemical inventory, monitored the safety of the laboratory activities, and composed standard operating procedures as the laboratory safety coordinator

Graduate Research Assistant, Prairie View A&M University, Prairie View, TX, USA.
August 2011-December 2012

- Functionalized carbon nanotubes and graphene nanosheets
- Studied adsorption of heavy metals from aqueous solution using reduced graphite oxide- polymer composites
- Synthesized, characterized and studied the magnetic properties of graphene-transition metal ferrites

Work Experience

Research & Development Intern, ExxonMobil Research and Engineering (EMRE),
Paulsboro, NJ January 2018-May 2018

- Studied the effect of grease formulation components on the friction performance of greases
- Developed method for grease friction measurement using the Mini Traction Machine (MTM)
- Tribological testing of grease film thickness and friction using EHD and MTM rig
- Performed rheological measurement of grease properties
- Worked with technologist to synthesis polyurea based grease

Summer Research Intern, Cooperative Agriculture Research Center (CARC), Prairie
View, Texas, USA May 2011-August 2012

- Synthesized and characterized graphene nanomaterial
- Synthesized and characterized nanocomposite of poly l-lactic acid (PLLA) grafted graphene by ring opening polymerization
- Studied the bioactivity of hFOB cells on graphene-PLLA composite for application in tissue engineering

Research Associate, Nextzon Business Services Limited, Victoria Island, Lagos,
Nigeria February 2010–August 2011

- Project identification, scoping and detailed estimating of start-up cost
- Gathered, collated and analyzed research data
- Assisted in managing company's asset/investment in various sectors including real estate, technology, education, and manufacturing

Teaching Experience

Graduate Teaching Assistant, University of Wisconsin-Milwaukee
Fall 2013-Spring 2019

- Planned lessons, delivered instructions, and created comprehensive assessments for 'Introductory Organic Chemistry Laboratory', 'Organic Chemistry Laboratory' and 'General Chemistry'

Mentoring, University of Wisconsin-Milwaukee
Spring 2013-Spring 2018

- Coached undergraduate students through their research in polymer and organic chemistry
- Mentor newly admitted graduate students on teaching assignments

Publications

- S. Banisadr, A. Oyefusi and J. Chen. A versatile transparent stimuli-responsive interference coloration. *ACS Applied Materials & Interfaces*, **2018**. DOI:10.1021/acsami.8b21290
- A. Oyefusi and J. Chen. Reprogrammable chemical 3D shaping for origami, kirigami, and reconfigurable molding. *Angewandte Chemie International Edition*, **2017**, 56, 8250 – 8253
- O. Olanipekun, A. Oyefusi, G.M. Neelgund and A. Oki; Synthesis and characterization of reduced graphite oxide- polymer composites and their application in adsorption of lead. *Spectrochimica Acta Part A*; **2015**, 149, 991-996
- A. Oyefusi, O. Olanipekun, G.M. Neelgund, D. Patterson, J.M. Stone, E. Williams, L. Carson, G. Regisford, and A. Oki; Hydroxyapatite grafted carbon nanotubes and graphene nanosheets: promising bone implant materials, *Spectrochimica Acta Part A*; **2014**, 132, 410-416
- O. Olanipekun, A. Oyefusi, G.M. Neelgund and A. Oki; Adsorption of lead (Pb) by graphite oxide. *Spectrochimica Acta Part A*; **2014**, 118, 857-860

Selected Presentations

- Poster: *Reprogrammable chemical 3D shaping for origami, kirigami, and reconfigurable molding*. NOBCCChE Conference. Minneapolis, **2017**
- Oral Presentation: *Reprogrammable chemical 3D shaping for origami, kirigami, and reconfigurable molding*. NOBCCChE Conference. Minneapolis, **2017**
- Poster: *Reprogrammable chemical 3D shaping for origami, kirigami, and reconfigurable molding*. America Chemical Society (ACS) Regional Meeting, Milwaukee, **2017**

- Poster: *Hydroxyapatite grafted carbon nanotubes and graphene nanosheets: Promising bone implant materials*. 3rd Science Technology Engineering Agriculture and Mathematics (STEAM) Symposium. **2011**
- Poster: *Hydroxyapatite grafted carbon nanotubes and graphene nanosheets: Promising bone implant materials*. Intercultural Cancer Council (ICC) Biennial Symposium on Minorities, the Medically Underserved & Health equity. Houston, TX, **June 2012**
- Poster: *Poly lactide grafted graphene nanosheets: facile synthesis, characterization and proliferation studies on hFOB 1.19 cell line*. NOBCChE Conference. Indianapolis, **2013**

Media Highlights, Academic Awards and Affiliations

- Media highlight of work by over ten media/ news outlets including Angewandte Chemie New and Science Magazine
- American Chemical Society (ACS) Student Exchange Award, 2018
- Chancellor's Award, University of Wisconsin-Milwaukee, 2012-2018
- American Chemical Society Member, January 2016-Present
- National Organization for Professional Advancement of Black Chemists and Chemical Engineers (NOBCChE), November 2017-Present
- Undergraduate Scholar's Award, University of Lagos, Nigeria

Workshops / Certificates

- Engineering Simulations-ANSYS, edX, Cornell University, 2016
- Chemical Hygiene Plan and Laboratory Safety Training, University of Wisconsin-Milwaukee, 2014
- Machine Learning and Big Data Analysis, Coursera, 2016-2017